Vol. 21 No. 03
November 2024

p-ISSN 1412-2960
e-ISSN 2579-521X

Indonesian Physics Communication

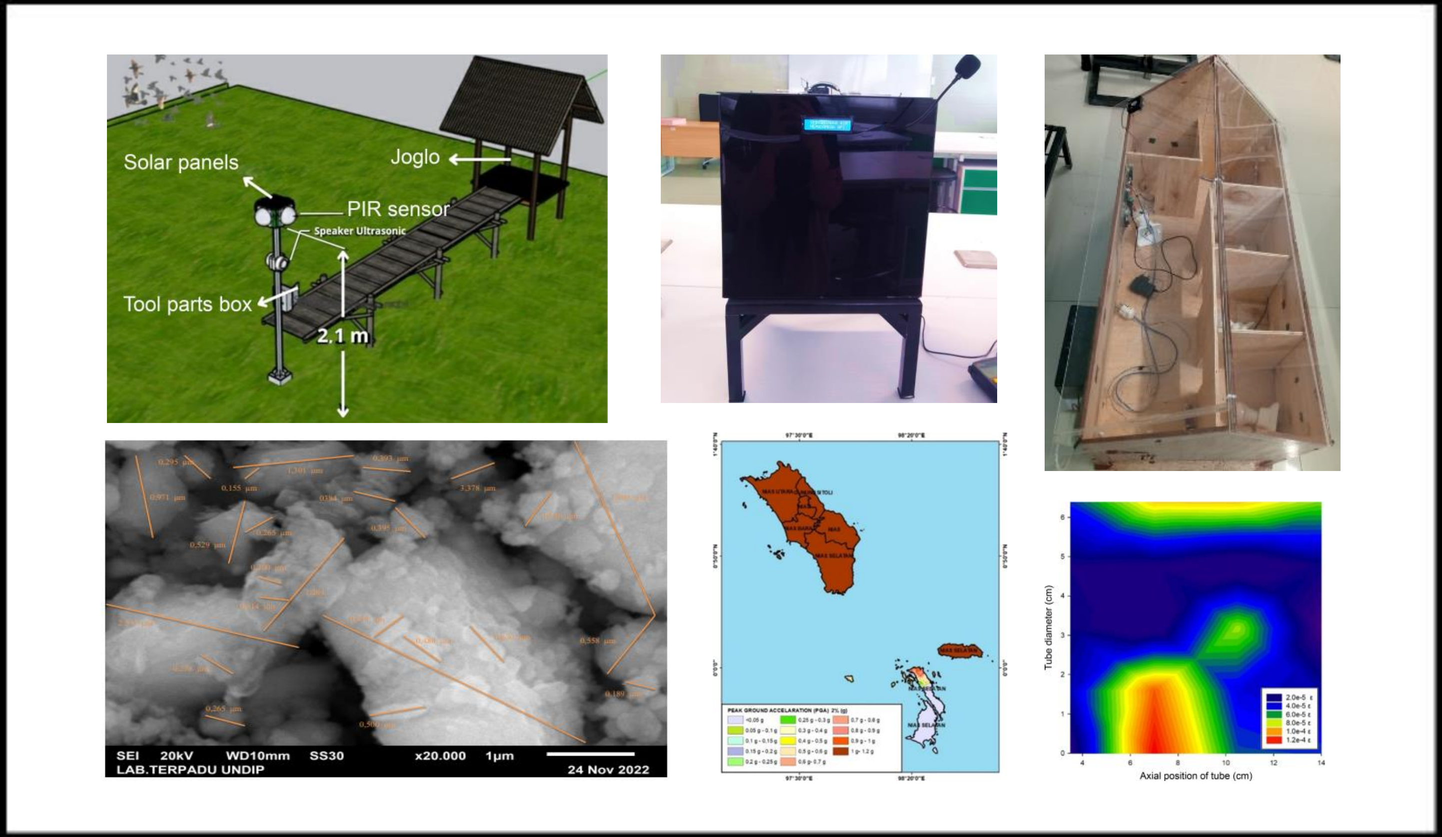

Department of Physics
Faculty of Mathematics and Natural Sciences
Universitas Riau
Kampus Bina Widya Jl. HR. Soebrantas Km. 12.5
Simpang Baru Panam, Pekanbaru 28293

ISSN 1412 2960

Indonesian Physics Communication
Vol. 21 No. 03
November 2024
Department of Physics, Universitas Riau
Pekanbaru

Vol. 21 No. 03
November 2024

p-ISSN 1412-2960
e-ISSN 2579-521X

Indonesian Physics Communication

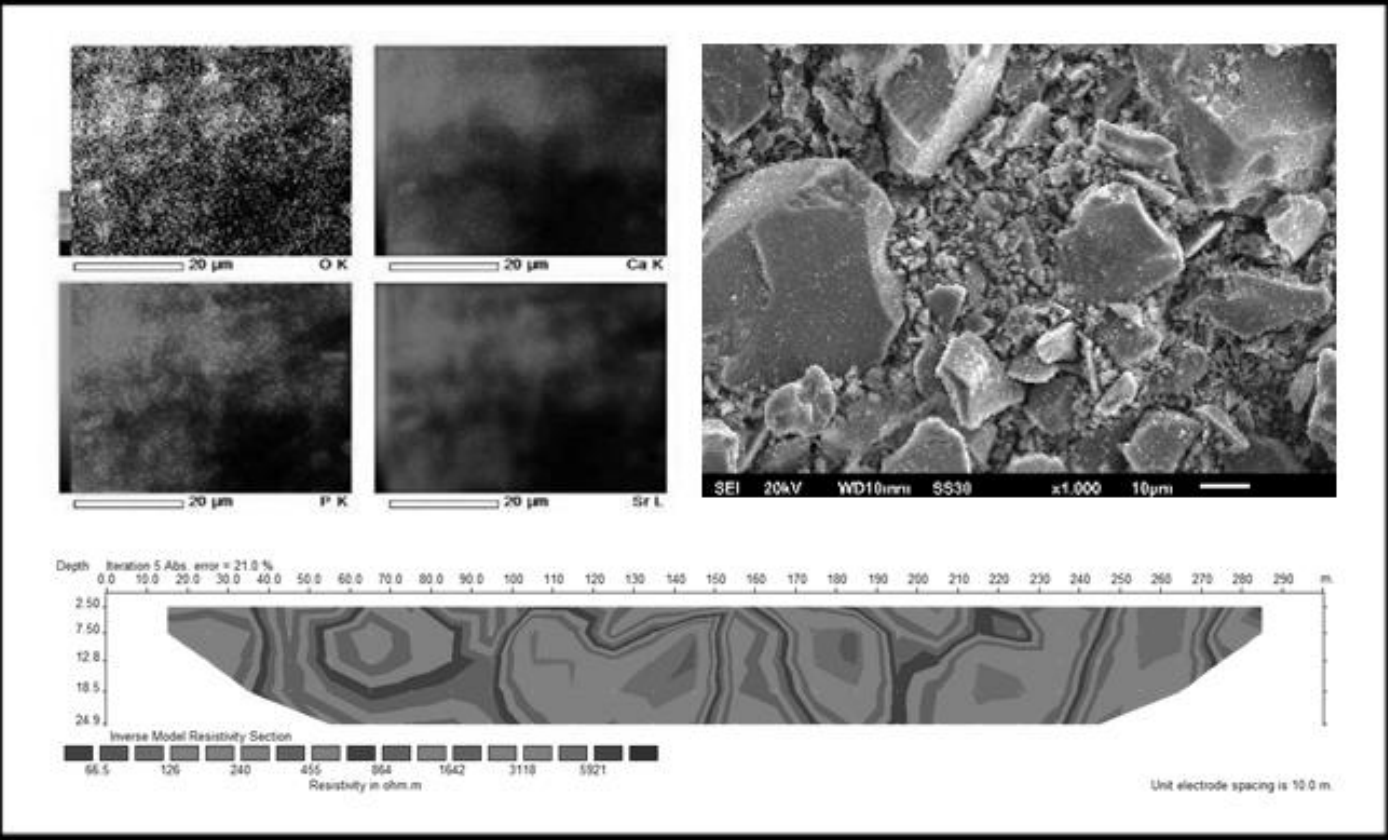

Department of Physics
Faculty of Mathematics and Natural Sciences
Universitas Riau
Kampus Bina Widya Jl. HR. Soebrantas Km. 12.5
Simpang Baru Panam, Pekanbaru 28293

Indonesian Physics Communication
Department of Physics, Universitas Riau, Pekanbaru, Indonesia
p-ISSN 1412-2960 | e-ISSN 2579-521X
Web: https://kfi.ejournal.unri.ac.id
E-mail: kfi@ejournal.unri.ac.id

Editorial Board of the Indonesian Physics Communication (IPC) Journal
Department of Physics, Faculty of Mathematics and Natural Sciences, Universitas Riau

Editorial Address:

Department of Physics, Faculty of Mathematics and Natural Sciences, Universitas Riau
Kampus Bina Widya Km 12.5 Simpang Baru Pekanbaru
Homepage: https://kfi.ejournal.unri.ac.id/index.php/JKFI
E-mail: kfi@ejournal.unri.ac.id

LIST OF CONTENTS

IPC
Indonesian Physics Communication
Department of Physics, Universitas Riau, Pekanbaru, Indonesia
p-ISSN 1412-2960 | e-ISSN 2579-521X
Vol. 21 | No. 3
November 2024
Web: https://kfi.ejournal.unri.ac.id
E-mail: kfi@ejournal.unri.ac.id

Harnessing multi-doping porous carbon from *Musa paradisiaca L.* peel waste for solid-state supercapacitors

Cenora Evelynza Purba[1], Nursyafni Nursyafni[1], Apriwandi Apriwandi[1], Pharada Kresna[2], Julnaidi[3], Muhammad Nasir[4], Rakhmawati Farma[1], Rahmi Dewi[1], Awaludin Martin[5], Lilik Tri Hardanto[6], Rika Taslim[7], Erman Taer[1,]*
[1]Department of Physics, Universitas Riau, Pekanbaru 28293, Indonesia
[2]State Junior High School 1 Tapung Hulu, Kampar 28464, Indonesia
[3]Department of Mechanical Engineering, Pekanbaru College of Technology, Pekanbaru 28125, Indonesia
[4]Department of Physics Education, Universitas Riau, Pekanbaru 28293, Indonesia
[5]Department of Mechanical Engineering, Universitas Riau, Pekanbaru 28293, Indonesia
[6]AspenTech, Jakarta 12190, Indonesia
[7]Department of Industrial Engineering, UIN Sultan Syarif Kasim, Pekanbaru 28293, Indonesia

*Corresponding author: erman.taer@lecturer.unri.ac.id

ABSTRACT

The demand for low-cost carbons with multi-doping in supercapacitors has led to a significant focus on utilizing biomass waste to produce activated carbons. The research successfully utilized *Musa paradisiaca L.* (MPL) peel as a porous carbon for solid-state supercapacitor. The process involved collecting banana peel waste, drying the peels using sunlight, pre-carbonization using a furnace, pH neutralization, drying, crushing carbon particles, and ensuring uniform particle size. Different concentrations of the catalytic $ZnCl_2$ solution (300, 500, and 700 mmol/g) were selected to optimize physical and electrochemical properties. The resulting chemically activated MPL carbon powder was evaluated using SEM-EDS, XRD, and BET. MPL activated carbon with a 500 mmol/g solution of $ZnCl_2$ was found to have optimal physical properties with a carbon percentage of 81.65%, oxygen 17.39%, phosphorus 0.42%, and boron 0.52%. Electrochemical properties were evaluated using dual-electrode system was exhibited the highest specific capacitance of 67 F/g. These findings demonstrate the potential of MPL peel waste as a high quality electrode for supercapaicor next-generation.

Keywords: Carbon; electrode materials; *Musa paradisiaca L.* peel; self-doped; supercapacitor

Received 06-09-2023 | Revised 10-10-2023 | Accepted 29-10-2024 | Published 30-11-2024

INTRODUCTION

Electrical energy has become a fundamental necessity for people worldwide and has significantly impacted almost every aspect of life. In Indonesia, the reliance on fossil fuels like oil, coal, and natural gas for electrical energy has led to air pollution, affecting the quality of life and public health [1]. The country's energy demand continues to rise due to economic activities in the industrial, transportation, commercial, and household sectors. This escalating energy requirement has prompted the exploration of various alternative energy sources to address the national energy crisis. Renewable energy sources such as solar and wind can generate electrical energy, but their effective use depends on efficient energy storage [2].

Supercapacitors are promising electrical energy storage technologies for the future. Supercapacitors are widely used in various applications such as in vehicles, trains, electronics, and in telecommunications. This technology offers energy storage with high power density and a long life cycle [3]. This is because supercapacitors store energy electrostatically through the absorption of electrolyte ions at the electrolyte electrode interface [4]. This non-faradaic process produces high power density but low energy density. Furthermore, its long life cycle occurs because supercapacitors do not experience significant degradation as occurs in

©Author(s) | DOI: 10.31258/jkfi.21.3.187-196

conventional batteries [5]. Among the components of supercapacitors, the selection of electrode materials is very important in improving their performance. Carbon materials have been widely studied as supercapacitor electrode materials because they have superior electrical conductivity, good chemical stability, and high surface area. However, carbon materials mostly come from fossil fuels whose application in the future industrial sector is limited due to their high cost, non-renewable sources, complicated synthesis, and environmental pollution. Thus, it is important to find carbon materials that are low-cost, easy to synthesize, and environmentally friendly.

Biomass-based carbon materials have attracted much attention due to their low cost, sustainability, and wide availability in nature [6]. Several biomass materials that have been utilized such as coconut shells have been successfully used as carbon sources with high carbon content and have O, N, and B doping [7]. Furthermore, hemp biomass has been successfully used as activated carbon material through high-temperature pyrolysis and chemical activation using KOH [8]. Garlic peel waste has been successfully used as porous activated carbon with the addition of melamine dopant and $KHCO_3$ activator selected as activator material [9]. In addition, other biomass materials that have also been successfully used as activated carbon are soybean straw [10], hazelnuts [11], and bamboo [12]. However, the methods used in these studies limit their large-scale application due to their complicated synthesis, longer time, and high cost [13]. Therefore, an easier, simpler, lower cost, and more time-saving method is needed.

On the other hand, bananas are one of Indonesia's plantation products that are produced in large quantities every year. Based on data from the Central Statistics Agency, another part of the banana that can also be used is the peel which contains 14.4% cellulose. In recent years, banana peels have been widely studied for use as absorbent materials (activated carbon). In more detail, *Musa paradisiaca L.* (MPL) peels contain 43.7% carbon elements consisting of cellulose, hemicellulose, chlorophyll pigments, and pectin substances so that they support the production of activated carbon as a supercapacitor electrode material. These components support the potential of MPL peels to be used as activated carbon with a high degree of crystallinity so that the activated carbon obtained can be applied to supercapacitors. MPL peels are synthesized with easy and cost-effective preparation, starting with the drying process, pre-carbonization using a furnace, chemical activation, and high-temperature pyrolysis. Chemical activation was carried out using a ZnCl2 activator with varying concentrations of 300, 500, and 700 mmol/g. The electrochemical performance of the MPL peels-activated carbon produced was tested using a two-electrode configuration, showing a specific capacitance of 67.14 F/g, with an energy density of 9.325 Wh/kg and a power density of 33.60 W/kg. The results of this study indicate that MPL peels waste can be used as an activated carbon material for supercapacitor electrodes.

MATERIALS AND METHODS

The MPL peel was cut into small pieces and then dried in the sun to reduce its water content. Furthermore, the pre-carbonization process was carried out on 5 kg of MPL peel samples in one burning using a furnace. The samples that had gone through the pre-carbonization process were then soaked in distilled water (equivalent) until pH = 7, then the samples were dried in the sun. Furthermore, the sample refinement process was carried out using a mortar and ball milling tool. The sample was first ground until smooth using a mortar, then the sample was put into a vial for the ball milling process for approximately 24 hours. The sample was sieved using a sieve measuring $\leq$ 60 µm to obtain uniform results.

Next, chemical activation was carried out using $ZnCl_2$ activator. The ratio of activator and carbon is 1 : 5, namely 30 grams of sample was inserted, then 150 ml of distilled water was used. The first stage in this chemical activation is to dissolve the $ZnCl_2$ activator into 150 ml of distilled water using a hot plate stirrer for 1 hour at 80°C. The MPL peel carbon sample was inserted into the activator mixture and stirred using a magnetic stirrer for 2 hours at 80°C, then dried using an oven. The dried sample was ground until smooth and then sieved using a 60 µm sieve. The MPL peel carbon sample was pyrolyzed at high temperature using a furnace. Furthermore, the sample was neutralized again so that the remaining combustion powder did not mix with the activated carbon sample.

The degree of crystallinity of MPL was evaluated using X-ray diffraction (XRD) in the angle range (2θ) 10° – 60° with a Shimadzu type MAXima_X XRD 7000. The surface morphology of MPL was observed using a scanning electron microscope (SEM) at magnifications of 5000× and 15000× and the elemental composition of MPL was evaluated through energy dispersive spectroscopy (EDS) using a Jeol JSM-IT200 instrument. The porosity properties of MPL were evaluated using a Quantachrome Nova 4200e instrument to determine the specific surface area and pore size distribution through the Brunauer–Emmett–Teller (BET) method. The electrochemical performance of the supercapacitor cell was evaluated using cyclic voltammetry (CV) and galvanostatic charge discharge (GCD) in a two-electrode system. Previously, the MPL-activated carbon powder sample was molded using a hydraulic press in the form of a monolithic coin and additional materials. The molded sample was then polished with a diameter and thickness of 8 mm and 0.2 mm, respectively, and immersed in 1 M H_2SO_4 electrolyte. The CV method at a maximum voltage window of up to 1 V used a CV UR Rad-ER 5841 physics instrument. The GCD method was carried out at a current density of 1 A/g using a CD UR Red-ER 2018.

RESULTS AND DISCUSSION

The samples of activated carbon from banana peel based on the influence of different concentrations of activators MPL-300, MPL-500, and MPL-700 showed XRD patterns in the form of two gentle peaks and several sharp peaks [14]. The MPL-300, MPL-500, and MPL-700 samples had peaks related to each scattering plane, where on the (002) and (100) planes in the range of 22.987°, 23.241°, 23.195° and 44.968°, 44.734°, 43.130°. The reflection angles on the hkl 002 and 100 planes indicate that the activated carbon samples based on banana peel have an amorphous structure.

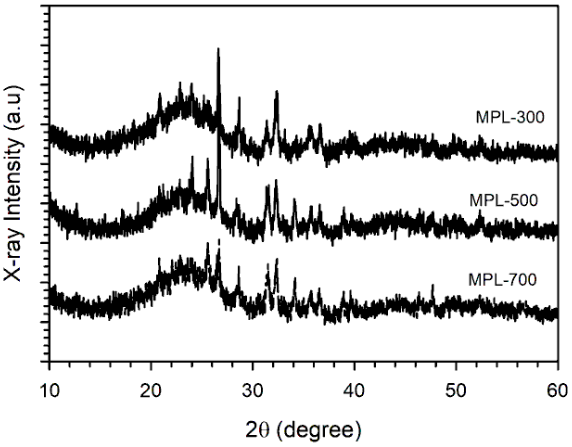

Figure 1. XRD pattern of MPL peels sample.

Table 1. Carbon lattice parameters of MPL peels.

Sample code	**$2\theta_{002}$ (°)**	**$2\theta_{100}$ (°)**	**d_{002} (Å)**	**d_{100} (Å)**	**L_c (Å)**	**L_a (Å)**
MPL-300	22.987	44.968	3.865	2.014	8.271	6.799
MPL-500	23.241	44.734	3.824	2.024	8.650	22.766
MPL-700	23.195	43.130	3.831	2.095	10.933	2.320

The data presented in Table 1 shows the lattice parameters that provide information on the shift of the 2θ angle that causes changes in the value of the microcrystalline layer in each sample. Giving the concentration of $ZnCl_2$ to the MPL peel sample from 300 to 700 mmol/g can increase the height value of the microcrystalline layer (Lc) from 8.271 to

10.933 Å. Then, a small Lc value indicates a larger specific surface area [15]. More details are discussed in the N_2 gas absorption analysis.

The pore characteristics of MPL were investigated through nitrogen adsorption/desorption measurements shown in Figures 2 (a) and (b). The isotherm curves between relative pressure (P/P_0) and STP volume (cm^3/g) where the relationship is in accordance with the IV isotherm based on the IUPAC classification. The hysteresis loops show varying shapes related to capillary condensation in the mesoporous layer depending on the concentration ratio of the activating agent and the synthesis form used [16]. The combination of macropores, mesopores, and micropores can support electrolytes to shorten the ion diffusion distance and facilitate rapid ion transfer. This type of curve forms micropores and mesopores which simultaneously contribute to the enhancement of the electrochemical double layer capacitance (EDLC) and improve the accessibility of high power density of supercapacitor devices.

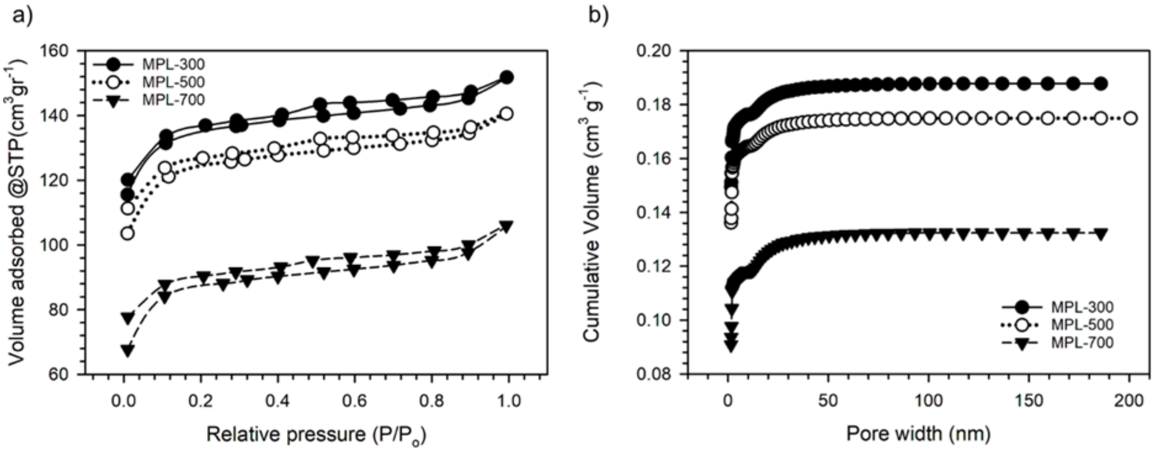

Figure 2. (a) N_2 gas absorption profile of activated carbon material, and (b) pore diameter vs cumulative volume of MPL peel samples.

The specific surface area of carbon electrodes MPL-300, MPL-500, and MPL-700 can be calculated by the BET method with values of 411.311 m^2/g, 378.786 m^2/g, and 266.822 m^2/g with total pores of MPL-300, MPL-500, and MPL-700 of 0.149 cm^2/g, 0.136 cm^2/g, and 0.090 cm^2/g respectively. These results indicate that MPL-300 has the highest specific surface area of 411.311 m^2/g. However, high surface area is not always a determining factor in increasing the specific capacitance value of carbon electrodes. This is because the higher surface area of MPL-300 can reduce the active properties of carbon which will cause brittle properties on the electrode, which can inhibit electrochemical properties [17].

The surface morphology of banana peel from all concentration variations is illustrated in Figure 3. Figures 3 (a) and 3 (b) show the morphology of MPL-300 samples at 5000x and 15000x magnifications. The MPL-300 sample displays a surface dominated by particle chunks and carbon aggregates in the size range of 291 – 612 nm at 5000x magnification and 130 – 353 nm at 15000x magnification. Figures 3 (c) and (d) show the morphology of MPL-500 samples at 5000x magnification with a size range of 361 – 1519 nm and at 15000x magnification the size range is 213 – 770 nm. The addition of a chemical activator of 500 mmol/g $ZnCl_2$ resulted in a relatively larger aggregate surface size. Figures 3 (e) and (f) with the MPL-700 sample show the morphology at 5000x magnification with a size range of 188 – 800 nm and 116 – 465 nm at 15000x magnification.

The elemental content for the three electrodes was evaluated through EDS. The results of the EDS characterization for the MPL-300, MPL-500, and MPL-700 samples were in the form of percentages of the constituent elements of the banana peel carbon electrode shown in Table 2.

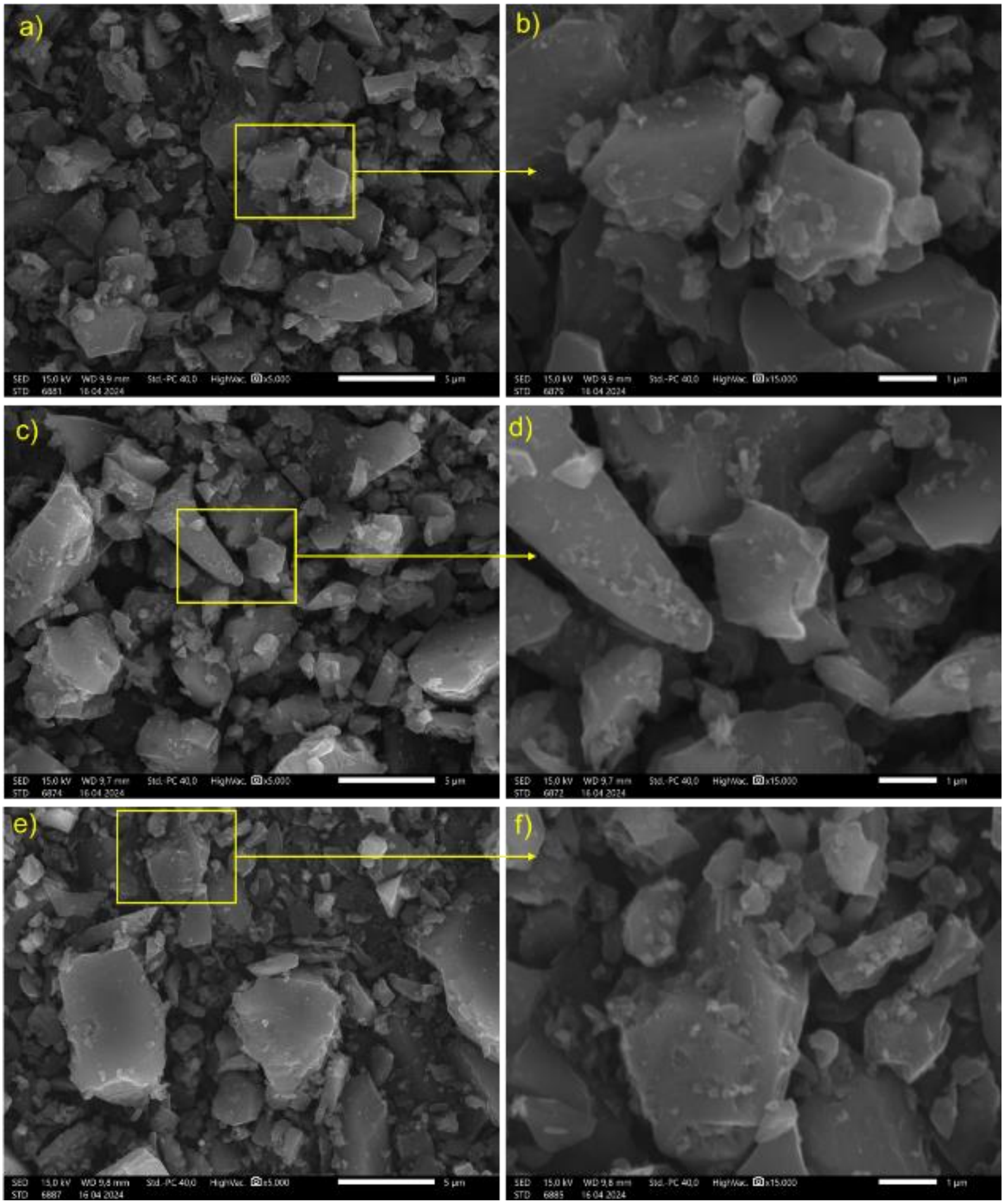

Figure 3. SEM images carbon of peels (a) MPL-300 magnification 5000x, (b) MPL-300 magnification 15,000x, (c) MPL-500 magnification 5,000x, (d) MPL-500 magnification 15,000x, (e) MPL-700 magnification 5,000x, (f) MPL-700 magnification 15,000x.

Table 2. Percentage content of elements in MPL peel samples.

Sample code	Percentage of elements (%)			
	C	O	P	B
MPL-300	90.32	9.59	0.09	-
MPL-500	88.74	10.38	0.22	0.66
MPL-700	86.79	13.06	0.15	-

Based on Table 2, it can be seen that the composition of the elements of the banana peel carbon electrode is carbon (C), oxygen (O), phosphorus (P), boron (B), and nitrogen (N). The elements of the banana peel content are dominated by carbon content with a percentage of 86.79% – 90.32%. The percentage of oxygen content in MPL-300, MPL-500, and MPL-700 are 0.59%, 10.38%, and 13.06% respectively. The percentage of phosphorus content in the MPL-300, MPL-500, and MPL-700 samples is 0.09%, 0.22%, 0.15%, followed by the boron content in MPL-500 which is 0.66%, in the MPL-300, MPL-500, and MPL-700 samples there is no nitrogen content.

In this case, oxygen is one of the heteroatoms and self-doping elements which is a contribution from the basic elements of biomass waste [18]. The high O element significantly presents an increase in the wettability and hydrophilicity features of the material which dramatically encourages electrolyte infiltration which causes faradaic redox reactions in the electrode material [19]. Phosphorus, boron, and nitrogen are natural dopings that can produce pseudocapacitor properties which means it is possible to achieve higher specific capacitance and energy density in supercapacitor electrochemical testing [20].

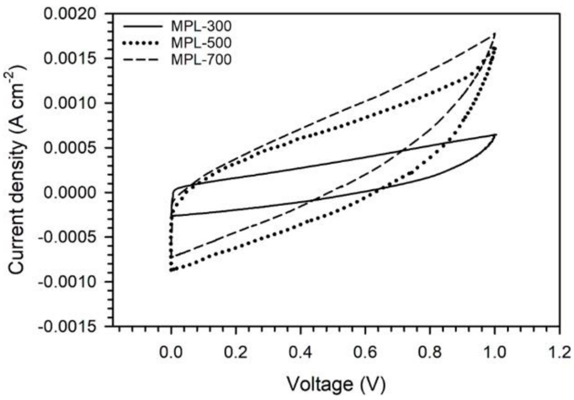

Figure 4. CV curve of MPL peel sample.

The electrochemical properties of activated carbon from supercapacitor electrodes were measured through CV shown in Figure 4. The results of the CV measurement are in the form of a curve with a distorted rectangular shape indicating that the supercapacitor has normal EDLC properties [21]. The area of the curve formed between the charge current (I_c) and the discharge current (I_d) indicates the specific capacitance value produced by the carbon electrode. The larger the area of the curve formed, the greater the specific capacitance value produced [22]. CV testing was carried out with a constant scan rate of 1 mV/s. CV testing on MPL peel carbon electrodes using H_2SO_4 electrolyte solution as a source of ion charge.

The MPL-300 and MPL-700 samples have the smallest CV curve area compared to the MPL-500 sample which has the largest curve area. These results indicate that the MPL-500 sample has the highest specific capacitance value and the largest curve so it has the ability to store the largest electrochemical energy among other samples. The concentration of MPL-300 can produce a specific capacitance value of 22.06 F/g. The addition of the concentration of $ZnCl_2$ activator to 500 mmol/g can significantly increase the specific capacitance value to 67.14 F/g with an energy density of 9.325 Wh/kg and a power density of 33.60 W/kg. The addition of the activator concentration reaching 700 mmol/g can reduce the specific capacitance value to 60.21 F/g because the addition of higher concentrations can reduce the physical properties of the electrode such as carbon content. This shows that 500 mmol/g has the optimum specific capacitance value.

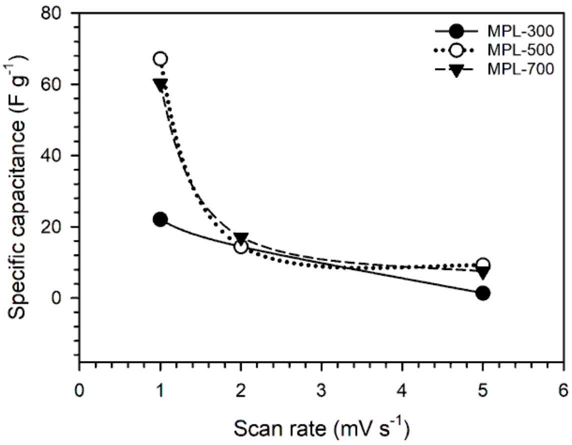

Figure 5. Specific capacitance curve versus scan rate.

Furthermore, the specific capacitance at higher scan rates is shown in Figure 5. From the figure, it can be seen that the specific capacitance decreases with the high scan rate given. This is because at high scan rates, the electrolyte ions do not have enough time to enter the pores of the electrode [23].

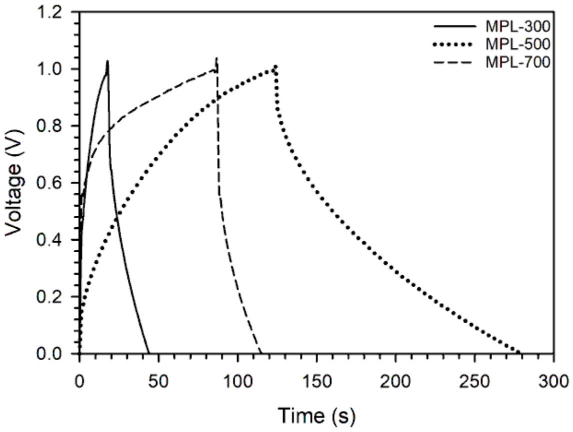

Figure 6. GCD curve of MPL peel sample.

More detailed electrochemical properties analysis evaluated through GCD can be seen in Figure 6. All samples show isosceles triangle curves indicating normal double-layer electrochemical properties [24]. The MPL-500 sample shows the longest charge-discharge measurement time which is marked by a larger isosceles triangle curve shape compared to the MPL-300 and MPL-700 samples. This proves that the MPL-500 sample has very good electrochemical properties resulting in a relatively higher specific capacitance value compared to the MPL-300 and MPL-700 samples. This is in accordance with the CV measurements which are also confirmed by the SEM results where the MPL-500 displays the sample morphology at 5000x magnification with a size range of 361 – 1519 nm and at 15000x magnification the size range is 213 – 770 nm. The administration of a chemical activator of 500 mmol/g $ZnCl_2$ produces a relatively larger aggregate surface size. In EDS, the addition of 500 mmol/g $ZnCl_2$ activator concentration can increase the percentage of carbon elements to 81.65%.

Table 3. Comparison of specific capacitance values of several biomasses

Biomass	Activator	Csp (F/g)	References
Ricinus communis shell	KOH	85	[25]
Palm waste	$CaCl_2$	137	[26]
Kapok	KOH	31.9	[27]
Sechium edule leaves	KOH	114	[28]
Orange peel	KOH	144	[29]
MPL-500	$ZnCl_2$	67.14	In this study

Table 3 shows a comparison of several specific capacitance values of several biomass with the addition of several chemical activators. Activated carbon made from MPL peels chemically activated using $ZnCl_2$ has the potential to be used as a supercapacitor cell electrode.

CONCLUSION

Multidoped carbon O, N, P, and B based on *Musa paradisiaca L.* peel waste has been successfully prepared using variations in $ZnCl_2$ activator concentrations of 300 mmol/g, 500 mmol/g and 700 mmol/g. The activated carbon obtained has a high carbon content and a good amorphous structure. MPL-500 activated carbon has optimal physical properties with a carbon content of 81.65%, oxygen 17.39%, phosphorus 0.42%, and boron 0.52%. Electrochemical performance was evaluated using 1 M H_2SO_4 electrolyte with a two-electrode system. The highest specific capacitance produced reached 67 F/g with an energy density of 9.325 Wh/kg and a power density of 33.60 W/kg. Furthermore, this study shows the use of MPL peel waste as a porous carbon-based material to be used as a supercapacitor electrode. Therefore, this research can be a reference for obtaining biomass-based porous carbon with environmentally friendly synthesis for supercapacitor energy storage devices.

ACKNOWLEDGMENTS

This research is financially supported by the first-year project of the Fostered Village Program (PDB) at the Institute for Research and Community Service, the University of Riau with the title "Solid biomass waste processing based on smoke-free and environmentally friendly technology for carbon production in Sumber Sari Village, Tapung Hulu District, Kampar Regency" with contract number of 1007/UN19.5.1.3/AL.04/2024.

REFERENCES

1. Pambudi, N. A., Firdaus, R. A., Rizkiana, R., Ulfa, D. K., Salsabila, M. S., Suharno, & Sukatiman. (2023). Renewable energy in Indonesia: Current status, potential, and future development. *Sustainability*, **15**(3), 2342.
2. Sun, J., Liu, C., Song, X., Zhang, J., Liu, Y., Liang, L., Jiang, R., & Yuan, C. (2022). Electrochemical energy storage devices under particular service environments: Achievements, challenges, and perspective. *Applied Physics Reviews*, **9**(3).
3. Zhang, J., Gu, M., & Chen, X. (2023). Supercapacitors for renewable energy applications: A review. *Micro and Nano Engineering*, 100229.
4. Samantaray, S., Mohanty, D., Hung, I. M., Moniruzzaman, M., & Satpathy, S. K. (2023). Unleashing recent electrolyte materials for next-generation supercapacitor applications: a comprehensive review. *Journal of Energy Storage*, **72**, 108352.
5. Lakshmi, K. S., & Vedhanarayanan, B. (2023). High-performance supercapacitors: A comprehensive review on paradigm shift of conventional energy storage devices. *Batteries*, **9**(4), 202.
6. Soffian, M. S., Halim, F. Z. A., Aziz, F., Rahman, M. A., Amin, M. A. M., & Chee, D. N. A. (2022). Carbon-based material derived from biomass waste for wastewater treatment. *Environmental Advances*, **9**, 100259.
7. Zhang, D., Zhan, X., Zhou, T., Du, J., Zou, K., & Luo, Y. (2024). N/B co-doped porous carbon with superior specific surface area derived from activation of biomass waste by novel deep eutectic solvents for Zn-ion hybrid supercapacitors. *Journal of Materials Science and Technology*, **193**, 22–28.
8. Tekin, B. & Topcu, Y. (2024). Novel hemp biomass-derived activated carbon as cathode material for aqueous zinc-ion hybrid supercapacitors: Synthesis, characterization, and electrochemical performance. *Journal of Energy Storage*, **77**, 109879.
9. Liu, S., Dong, K., Guo, F., Wang, J., Tang, B., Kong, L., Zhao, N., Hou, Y., Chang, J., & Li, H. (2024). Facile and green synthesis of biomass-derived N, O-doped hierarchical porous carbons for high-performance supercapacitor application. *Journal of Analytical and Applied Pyrolysis*, **177**, 106278.
10. Li, Y., Kong, C., Du, Z., Zhang, J., Qin, X., Zhang, J., Li, C., Jin, Y., & Wang, S. (2024). Oxygen-rich hierarchical porous carbon nanosheets derived from the KOH/KNO_3 co-activation treatment of soybean straw for high-performance supercapacitors. *Energy Advances*, **3**(4), 904–915.
11. Li, H., Ma, Y., Wang, Y., Li, C., Bai, Q., Shen, Y., & Uyama, H. (2024). Nitrogen enriched high specific surface area biomass porous carbon: A promising electrode material for supercapacitors. *Renewable Energy*, **224**, 120144.
12. Yue, W., Yu, Z., Zhang, X., Liu, H., He, T., & Ma, X. (2024). Green activation method and natural N/O/S co-doped strategy to prepare biomass-derived graded porous carbon for supercapacitors. *Journal of Analytical and Applied Pyrolysis*, **178**, 106409.
13. Abolore, R. S., Jaiswal, S., & Jaiswal, A. K. (2023). Green and sustainable pretreatment methods for cellulose extraction from lignocellulosic biomass and its applications: A review. *Carbohydrate Polymer Technologies and Applications*, 100396.

14. Hegde, S. S. & Bhat, B. R. (2024). Biomass waste-derived porous graphitic carbon for high-performance supercapacitors. *Journal of Energy Storage*, **76**, 109818.
15. Xiong, S., Zhao, X., Lv, F., Zhang, W., Yang, N., Zhang, Y., Wang, X., Gong, M., Wang, C., & Li, Z. (2023). Study on the influence of pre-oxidation treatment on surface wettability and supercapacitive performance of coal-based activated carbon. *Energy & Fuels*, **37**(12), 8672–8680.
16. Blachnio, M., Derylo-Marczewska, A., Winter, S., & Zienkiewicz-Strzalka, M. (2021). Mesoporous carbons of well-organized structure in the removal of dyes from aqueous solutions. *Molecules*, **26**(8), 2159.
17. Taslim, R., Apriwandi, A., & Taer, E. (2022). Novel moringa oleifera leaves 3D porous carbon-based electrode material as a high-performance EDLC supercapacitor. *ACS omega*, **7**(41), 36489–36502.
18. Gopalakrishnan, A., & Badhulika, S. (2020). Effect of self-doped heteroatoms on the performance of biomass-derived carbon for supercapacitor applications. *Journal of power sources*, **480**, 228830.
19. Zhao, L., Li, Y., Yu, M., Peng, Y., & Ran, F. (2023). Electrolyte-wettability issues and challenges of electrode materials in electrochemical energy storage, energy conversion, and beyond. *Advanced Science*, **10**(17), 2300283.
20. Lin, X., Yin, S., Zhang, W., & Li, X. (2022). N/P/O doped porous carbon materials for supercapacitor with high performance. *Diamond and Related Materials*, **125**, 109025.
21. Nayak, M. K., Sahoo, B. B., Thatoi, D. N., Nazari, S., Ali, R., & Chamkha, A. J. (2024). Recent advances on supercapacitor electrode materials from Biowastes-A review. *Journal of Science: Advanced Materials and Devices*, 100734.
22. Taer, E., Deraman, M., Taslim, R., & Iwantono. (2013). Preparation of binderless activated carbon monolith from pre-carbonization rubber wood sawdust by controlling of carbonization and activation condition. *AIP Conference Proceedings*, **1554**(1), 33–37.
23. Taer, E., Syamsunar, N., Apriwandi, A., & Taslim, R. (2023). Novel Solanum torvum fruit biomass-derived hierarchical porous carbon nanosphere as excellent electrode material for enhanced symmetric supercapacitor performance. *JOM*, **75**(11), 4494–4506.
24. Rajivgandhi, P., Mariappan, A., Manivannan, M., Dharman, R. K., Oh, T. H., & Sekar, A. (2024). Biomass waste derived from cassia fistula into value-added porous carbon electrode for aqueous symmetric supercapacitors. *Inorganic Chemistry Communications*, **165**, 112552.
25. Rajasekaran, S. J., Grace, A. N., Jacob, G., Alodhayb, A., Pandiaraj, S., & Raghavan, V. (2023). Investigation of different aqueous electrolytes for biomass-derived activated carbon-based supercapacitors. *Catalysts*, **13**(2), 286.
26. Rustamaji, H., Prakoso, T., Devianto, H., Widiatmoko, P., Febriyanto, P., & Eviani, M. (2024). Modification of hydrochar derived from palm waste with thiourea to produce N, S co-doped activated carbon for supercapacitor. *Sustainable Chemistry for the Environment*, **7**, 100132.
27. Thazin, N. M., Chaiammart, N., Thu, M. M., & Panomsuwan, G. (2022). Effect of pre-carbonization temperature on the porous structure and electrochemical properties of activated carbon fibers derived from kapok for supercapacitor applications. *Journal of Metals, Materials and Minerals*, **32**(1), 55–64.
28. Jalalah, M., Rudra, S., Aljafari, B., Irfan, M., Almasabi, S. S., Alsuwian, T., Patil, A.A., Nayak, A.K., & Harraz, F. A. (2022). Novel porous heteroatom-doped biomass activated carbon nanoflakes for efficient solid-state symmetric supercapacitor devices. *Journal of the*

Taiwan Institute of Chemical Engineers, **132**, 104148.

29. Ajay, K. M., Dinesh, M. N., Byatarayappa, G., Radhika, M. G., Kathyayini, N., & Vijeth, H. (2021). Electrochemical investigations on low cost KOH activated carbon derived from orange-peel and polyaniline for hybrid supercapacitors. *Inorganic Chemistry Communications*, **127**, 108523.

Indonesian Physics Communication
Department of Physics, Universitas Riau, Pekanbaru, Indonesia
p-ISSN 1412-2960 | e-ISSN 2579-521X
Vol. 21 | No. 3
November 2024
Web: https://kfi.ejournal.unri.ac.id
E-mail: kfi@ejournal.unri.ac.id

Areca-nut waste-derived carbon porous for sustainable electrode materials: A brief study for green-supercapacitor

Nursyafni Nursyafni[1], **Julnaidi**[2], **Erman Taer**[1,*]
[1]Department of Physics, Universitas Riau, Pekanbaru 28293, Indonesia
[2]Department of Mechanical Engineering, Pekanbaru College of Technology, Pekanbaru 28125, Indonesia

*Corresponding author: erman.taer@lecturer.unri.ac.id

ABSTRACT

Biomass-based porous carbon is an exceptional material with unique nano-morphological properties and a high surface area, making it an ideal candidate for improving the performance of supercapacitor electrodes. Herein, activated carbon derived novel areca-nut waste (ANW) as electrodes materials were successfully produced using a simple method. The process involved drying the ANW using pre-carbonization, chemical activation, and high-temperature pyrolysis. The zinc chloride was selected as chemical catalytic in 1 m/l solution. Subsequently, porous carbon was produced at different physical activation temperatures of 800°C, 850°C, and 900°C. The activated carbon was converted into coin-like design with an additional adhesive of PVA. The electrochemical properties were assessed using a two-electrode system in a 1 M H_2SO_4 electrolyte. The ANW-based supercapacitor demonstrated good electrochemical performance, with an optimal specific capacitance of 94.6 F/g at 850°C. Additionally, it exhibited an optimal energy density of 12.8 Wh/kg and a power density of 245.516 W/kg. These results suggest that porous carbon derived from ANW biomass holds promise as a sustainable working electrode for green-supercapacitor.

Keywords: Activated carbon; areca-nut waste; biomass; electrode; supercapacitor

Received 06-09-2023 | Revised 13-10-2023 | Accepted 31-10-2024 | Published 30-11-2024

INTRODUCTION

The growth of the human population and the development of the global economy have led to an increasing demand for energy worldwide. It is estimated that by 2026, the demand for energy will double. Therefore, it is important to study the development of new and sustainable energy sources. Supercapacitors have attracted attention because they are a new type of energy storage device that has high power density, long service life, good cycle stability, and large capacity [1]. In addition, supercapacitors are efficient, green, and environmentally friendly energy storage devices [2]. However, the low energy density of supercapacitors is a weakness that limits their widespread application. To overcome these problems, the development of electrode materials is necessary because they are a key factor in improving the performance of high-performance supercapacitors [3].

Activated carbon is commonly used as an electrode material due to its affordability, stability, and good conductivity [4]. It's typically derived from coal, petroleum, and biomass. Biomass-derived activated carbon offers advantages such as abundant availability, unique porosity, sustainability, and environmental friendliness [5]. Previous studies have highlighted the exceptional properties of natural waste-based carbon materials, including their nano morphology, hierarchical pores, and hydrophilicity supporting heteroatom elements [6, 7]. For example, hierarchically porous carbon from biomass plane tree fruit fluffs achieved an energy density of 46.3 Wh/kg [8]. Porous carbon obtained from biomass garlic peels exhibited an energy density of 9.07 Wh/kg and a specific capacitance reaching 396.25 F/g [4]. Additionally, porous carbon from the jujube shell demonstrated a high

©Author(s) | DOI: 10.31258/jkfi.21.3.197-204

specific capacitance of 535 F/g with an energy density of 13.97 Wh/kg [9]. However, not all biomass can exhibit these characteristics through simple and environmentally friendly methods, requiring further intensive studies to identify potential biomass and environmentally friendly approaches. On the other hand, the areca-nut (AN) is a major horticultural crop in Indonesia, occupying 147,890 hectares and supplying 80% of the global AN demand [10]. The substantial area of AN plantations generates significant waste, including areca-nut waste (ANW), which contains 66.08% cellulose, 7.40% hemicellulose, 19.59% lignin, and other minor components [10, 11]. Given these contents, ANW holds promise as a raw material for activated carbon production.

Furthermore, one of the main ways to convert biomass into activated carbon is by using the thermochemical transformation method [12]. This method consists of two steps, namely carbonization and activation. Carbonization is the process of converting organic matter into carbon through low-temperature pyrolysis [13]. This process focuses on removing volatile compounds, and hydrocarbons and breaking down precursors until charred residue remains. Furthermore, the activation process involves the addition of appropriate activating agents to obtain a high surface area with its unique porosity. The activation process is divided into two, namely chemical activation and physical activation. The chemical activation process is a common method used to produce carbon-based activated carbon derived from biomass [14]. In this process, biomass carbon material is mixed with chemicals and carbonized using inert gas. While the physical activation process uses oxygen-containing gases such as CO_2 and water vapor. This process takes place at high temperatures (800°C – 1000°C) by decomposing carbon materials so that they form many pores and cracks [15].

In this study, a simple and cost-effective synthesis is reported to obtain biomass-based activated carbon. Conversion of ANW into carbon through drying, pre-carbonization, chemical activation, carbonization, and physical activation processes. Chemical activation was carried out using 1 M $ZnCl_2$ as an activating agent. Carbon samples were prepared in powder form which were then carbonized and physically activated. Carbonization was carried out up to a temperature of 600°C with an inert gas environment (N_2). Physical activation was applied using different temperatures, namely at 800°C, 850°C, and 900°C with a CO_2 gas environment. Furthermore, the electrochemical performance of the activated carbon obtained was evaluated in a 2-electrode configuration with a specific capacitance of 94.6 F/g with an energy density of 12.8 Wh/kg and a power density of 245.516 W/kg. Therefore, this study proves that ANW biomass can be utilized as activated carbon to be used as an electrode supercapacitor.

MATERIALS AND METHODS

Material

Samples of ANW were collected from plantations in Solok Regency, Indonesia. We used $ZnCl_2$ from Merck KgA as the chemical activator. The gases N_2 and CO_2 were obtained from PT. Aneka Gas Industri Tbk, Indonesia. The electrolyte material H_2SO_4 was supplied by Panreac Química Sau. Duck eggshell membranes were used as separators, and DI water was produced on the laboratory scale.

Preparation of Sample Powder

The ANW was initially cleaned and cut into small pieces measuring 3 × 2 cm. Afterward, it was dried using sunlight for 2 days and then in an oven at 110°C for 48 hours. The drying process was then continued using a vacuum oven at a temperature range of 50°C – 250°C. Subsequently, the sample was ground using a mortar and ball milling. After grinding, the sample was sieved to obtain a uniform powder size of < 60 µm.

Preparation of Porous Carbon from ANW

The ANW sample powder was chemically impregnated using 1 M $ZnCl_2$ with distilled water and carbon. This process involved using a hotplate set to a rotation of 300 rpm and a temperature of 80°C. After impregnation, the sample was dried in an oven and then ground into powder again. The obtained carbon powder was subjected to pyrolysis through carbonization and physical activation. Carbonization was carried out at temperatures ranging from 30°C to 289°C and from 289°C to 600°C, with a N_2 gas flow rate of 1°C/min and 3°C/min, respectively. Physical activation was performed using CO_2 gas at temperatures of 800°C, 850°C, and 900°C, with a gas flow rate of 10°C/min. The resulting porous carbons were labeled as ANW-800, ANW-850, and ANW-900. The pyrolysis products were neutralized using DI water until the pH reached 7 and then dried in an oven at 110°C.

Material Characterization

Phase and degree of crystallinity of ANW were evaluated using X-ray diffraction (XRD) with a Shimadzu type MAXima_X, within the angle range (2θ) 10° – 60°, with plate number 1 No. BMN: 3.08.02.01.027.1. The electrochemical properties of the supercapacitor cell were evaluated in a two-electrode system using additional adhesive. The electrodes, with a diameter of 8 mm and a thickness of 0.2 mm, were prepared in a 1 M H_2SO_4 electrolyte solution and separated using a duck eggshell membrane. The electrochemical performance was measured using cyclic voltammetry (CV) and galvanostatic charge discharge (GCD) techniques. The CV method was carried out using a CV UR Rad-ER 5841 physics instrument, testing at a maximum voltage window of up to 1 V at scan rates of 1, 2, 5, and 10 mV/s. The GCD method was carried out using a CD UR Red-ER 2018 with a current density of 1 A/g. Specific capacitance, resistance, energy density, and power density were obtained from the CV and GCD methods, and calculated using standard equations.

RESULTS AND DISCUSSION

The XRD pattern of ANW at different physical activation temperatures is characterized in Figure 1. This pattern shows two diffraction peaks at 2θ values of 22.424° – 23.496° and 42.013° – 44.714° which are related to the crystal planes (002) and (100). This characteristic indicates low graphitization so that the activated carbon electrode has an amorphous nature [16]. Therefore, this structure can form more developed pores which results in high electrical conductivity values. High conductivity values can support better electrochemical properties. This study is in line with previous studies using different biomass, namely *Mangifera indica* leaf [17], *Phyllostachys edulis* [18], and paddy straw [19]. Furthermore, the XRD pattern also shows several sharp peaks which confirm the presence of crystalline compounds in each sample.

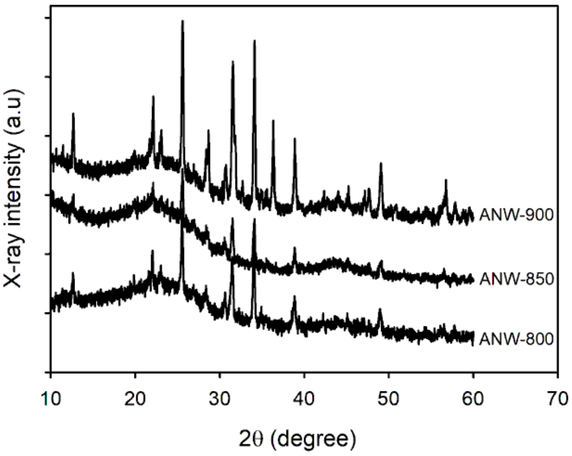

Figure 1. XRD pattern of ANW samples.

Table 1 shows the interlayer d-spacing and microcrystalline dimensions for the three ANW samples. The d_{002} and d_{100} values of ANW based on the Bragg equation $2d\sin\theta = n\lambda$ have values ranging from 3.783 – 3.962 Å and 2.025 – 2.148 Å, respectively. The d_{002} value obtained is higher than the d_{002} value of graphite confirming that the ANW-activated carbon sample has high porosity due to weak graphitization so that the sample has better amorphous properties. Furthermore, the layer height value (L_c) is related to the specific surface area according to the empirical formula ($SSA_{xrd} = 2/\rho_{xrd}L_c$), where $\rho_{xrd} = (d_{002(graphite)}/d_{002}) \times \rho_{graphite}$ [20]. Based on the empirical formula, it can be concluded that the L_c value is inversely proportional to the specific surface area value. If the L_c value is small, the surface area is large. From Table 1, it can be seen that ANW-850 has the smallest Lc layer height value, which is 8.606 Å, so ANW-850 has the highest specific surface area which can improve the performance of supercapacitor electrodes.

Table 1. Lattice parameters and interlayer spacing for ANW activated carbon samples.

Samples code	$2\theta_{002}$ (°)	$2\theta_{001}$ (°)	d_{002} (Å)	d_{100} (Å)	L_c (Å)	L_a (Å)
ANW-800	22.424	44.714	3.962	2.025	8.982	15.619
ANW-850	23.496	44.128	3.783	2.050	8.606	36.752
ANW-900	22.913	42.013	3.878	2.148	9.177	10.505

The electrochemical properties of ANW were evaluated through a two-electrode system in 1 M H_2SO_4 electrolyte using CV and GCD. Figure 2 depicts the CV curves for the three electrodes at a scan rate of 1 mV/s with a voltage range of 0 – 1 V. The curves have a distorted rectangular shape, indicating the characteristics of the electrical double-layer capacitance derived from the porous carbon material [21]. The sample ANW-800 shows a fairly large hysteresis curve, which indicates a specific capacitance value of 60 F/g. Increasing the physical activation temperature significantly increases the current density of ANW-850, with its specific capacitance reaching 76 F/g. However, further increasing the physical activation temperature to 900°C reduces the current density in the hysteresis loop, confirming that the specific capacitive property of the third electrode decreases to 14 F/g.

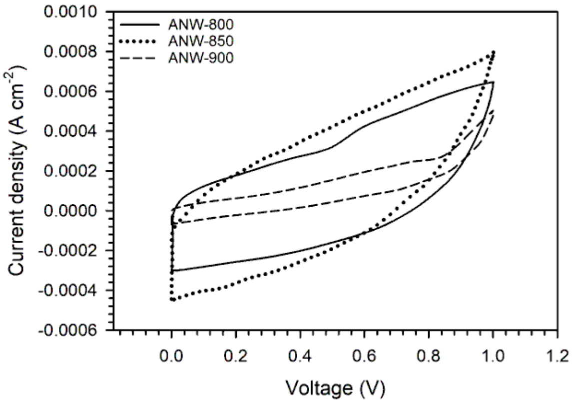

Figure 2. CV profile of ANW sample at a scan rate of 1 mV/s.

Furthermore, the electrode potential of ANW-850 was evaluated at different scan rates ranging from 1 to 10 mV/s, as shown in Figure 3. The figure illustrates that at high scan rates, the ANW-850 sample displays a good rectangular curve, which indicates ideal capacitive behavior characteristics [22]. However, at higher scan rates, the ions have enough time to diffuse into the electrode pores, the electrolyte ions are unable to access the interior of the active material, leading to a decrease in capacitance [23, 24].

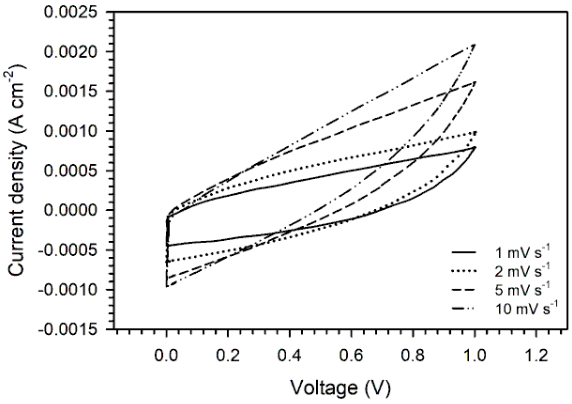

Figure 3. The CV profiles of ANW-850 at scan rates of 1, 2, and 5 mV/s.

The electrochemical performance of ANW-850 was thoroughly analyzed through GCD measurements. The GCD curve of ANW-850 was assessed at a current density of 1 A/g, as depicted in Figure 4. The results showed an isosceles triangle shape, confirming the normal double-layer electrochemistry [25]. In addition, the straight line on the discharge curve indicated the ohmic resistance of the electrode [26]. The resistance value for ANW-850 was determined to be 0.27 Ω, with a specific capacitance of 94.6 F/g. Furthermore, the charge and discharge times on the GCD curve validated the coulombic efficiency value of the ANW-850 sample, which was found to be 87% [27]. These findings confirmed the superior electrochemical performance of the ANW-850 sample. In particular, the electrochemical performance of ANW-850 showed a specific capacitance of 94.6 F/g, accompanied by an energy density of 12.8 Wh/kg and a power density of 245.516 W/kg. The electrochemical performance of ANW was compared with that of other biomass-based activated carbon supercapacitor electrodes, as shown in Table 2.

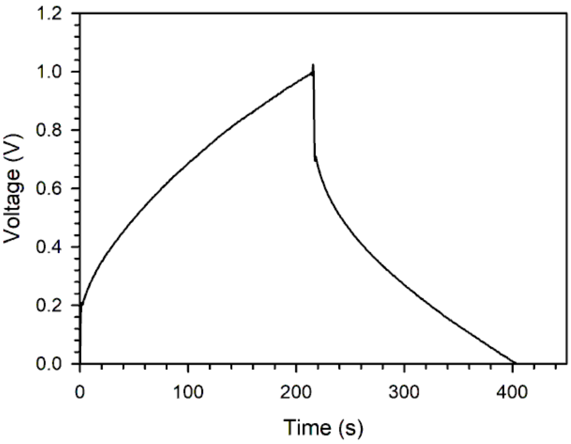

Figure 4. The GCD profiles of ANW samples.

Tabel 2. Comparison of the electrochemical performance of activated carbon-based supercapacitor electrodes derived from biomass.

sources	Csp (F/g)	Esp (Wh/kg)	Psp (W/kg)	References
Jack wood tree	147	8.02	68.5	[28]
Asparagus waste	160	31	560	[29]
Cashew nut shells	106	2.43	1002	[30]
Palm waste	135.1	3.4	202.6	[31]
Areca-nut waste	94.6	12.8	245.51	In this study

CONCLUSION

Porous carbon based on areca nut waste biomass has been successfully obtained through a simple method. The method begins with drying, pre-carbonization, chemical activation using 1 M $ZnCl_2$, and high-temperature pyrolysis (carbonization and physical activation). Physical activation was carried out with different temperature treatments, namely 800°C, 850°C, and 900°C. The activated carbon obtained has an amorphous structure with a 2θ angle of 22.424° – 23.496° and 42.013° – 44.714°. ANW-850 has the smallest L_c value of 8.606 Å, indicating a larger surface area than the other two samples. The electrochemical performance of ANW was also evaluated through a CV with specific capacitances of 60, 76, and 14 F/g for ANW-800, ANW-850, and ANW-900, respectively. Further electrochemical performance of ANW-850 was also evaluated using GCD which obtained a specific capacitance of 94.6 F/g with an energy density of 12.8 Wh/kg and a power density of 245.516 W/kg at a current density of 1 A/g. Thus, it can be concluded that the areca nut waste is suitable to be used as a carbon source for application in high-performance supercapacitor electrodes.

ACKNOWLEDGMENTS

The research was funded by Direktorat Jenderal Pendidikan Tinggi, Riset dan Teknologi, Republic of Indonesia in master thesis research-postgraduate program scheme with contract number of 20728/UN19.5.1.3/AL.04/2024.

REFERENCES

1. Wang, W., Shen, Y., Ma, Z., Wei, X., Fan, H., & Bai, Q. (2024). High-performance supercapacitors based on self-supporting thick carbon electrodes from renewable

biomass wood. *Sustainable Materials and Technologies*, **40**, e00824.

2. Hu, H., Yan, M., Jiang, J., Huang, A., Cai, S., Lan, L., Ye, K., Chen, D., Tang, K., Zuo, Q., Zeng, Y., & Zhao, Y. (2023). A state-of-the-art review on biomass-derived carbon materials for supercapacitor applications: From precursor selection to design optimization. *Science of The Total Environment*, 169141.
3. Liu, L., Zhang, W., Lu, B., Cheng, Z., Cao, H., Li, J., Fan, Z., & An, X. (2024). Controllable heteroatoms doped electrodes engineered by biomass based carbon for advanced supercapacitors: A review. *Biomass and Bioenergy*, **186**, 107265.
4. Liu, S., Dong, K., Guo, F., Wang, J., Tang, B., Kong, L., Zhao, N., Hou, Y., Chang, J., & Li, H. (2024). Facile and green synthesis of biomass-derived N, O-doped hierarchical porous carbons for high-performance supercapacitor application. *Journal of Analytical and Applied Pyrolysis*, **177**, 106278.
5. Yuksel, R. & Karakehya, N. (2024). High energy density biomass-derived activated carbon materials for sustainable energy storage. *Carbon*, **221**, 118934.
6. Taer, E., Yanti, N., Apriwandi, A., Ismardi, A., & Taslim, R. (2023). Novel O, P, S self-doped with 3D hierarchy porous carbon from aromatic agricultural waste via H_3PO_4 activation for supercapacitor electrodes. *Diamond and Related Materials*, **140**, 110415.
7. Taer, E., Apriwandi, A., Farma, R., & Taslim, R. (2024). Synthesis of highly self-NO-dual doped unique carbon blooming flower-like nanofiber derived novel snake-plant waste for ultrahigh energy of solid-state-supercapacitor. *Chemical Engineering Science*, **285**, 119566.
8. Wang, M. X., He, D., Zhu, M., Wu, L., Wang, Z., Huang, Z. H., & Yang, H. (2023). Green fabrication of hierarchically porous carbon microtubes from biomass waste via self-activation for high-energy-density supercapacitor. *Journal of Power Sources*, **560**, 232703.
9. Li, Y. & Qi, B. (2023). Secondary utilization of jujube shell bio-waste into biomass carbon for supercapacitor electrode materials study. *Electrochemistry Communications*, **152**, 107512.
10. Ridho, M. R., Nawawi, D. S., Juliana, I., & Fatriasari, W. (2023). The kraft lignin characteristics of areca leaf sheath isolated by phosphoric acid. *Bioresource Technology Reports*, **23**, 101569.
11. Madyaratri, E. W., Ridho, M. R., Iswanto, A. H., Osvaldová, L. M., Lee, S. H., Antov, P., & Fatriasari, W. (2023). Effect of lignin or lignosulfonate addition on the fire resistance of areca (*Areca catechu*) particleboards bonded with ultra-low-emitting urea-formaldehyde resin. *Fire*, **6**(8), 299.
12. Tekin, B. & Topcu, Y. (2024). Novel hemp biomass-derived activated carbon as cathode material for aqueous zinc-ion hybrid supercapacitors: Synthesis, characterization, and electrochemical performance. *Journal of Energy Storage*, **77**, 109879.
13. Muttil, N., Jagadeesan, S., Chanda, A., Duke, M., & Singh, S. K. (2022). Production, types, and applications of activated carbon derived from waste tyres: an overview. *Applied Sciences*, **13**(1), 257.
14. Taer, E., & Taslim, R. (2020). A high potential of biomass leaves waste for porous activated carbon nanofiber/nanosheet as electrode material of supercapacitor. *Journal of Physics: Conference Series*, **1655**(1), 012007.
15. Qiu, C., Jiang, L., Gao, Y., & Sheng, L. (2023). Effects of oxygen-containing functional groups on carbon materials in supercapacitors: A review. *Materials and Design*, **230**, 111952.
16. Ma, Y., Tian, J., Li, L., Kong, L., Liu, S., Guo, K., & Chen, X. (2021). Interconnected hierarchical porous carbon synthesized from freeze-dried celery for supercapacitor with high performance.

International Journal of Energy Research, **45**(6), 9058–9068.

17. Hegde, S. S. & Bhat, B. R. (2024). Sustainable energy storage: Mangifera indica leaf waste-derived activated carbon for long-life, high-performance supercapacitors. *RSC advances*, **14**(12), 8028–8038.
18. Egun, I. L., Akinwolemiwa, B., Yin, B., Tian, H., He, H., Fow, K. L., Zhang, H., Chen, G. Z., & Hu, D. (2024). Conversion of high moisture biomass to hierarchical porous carbon via molten base carbonisation and activation for electrochemical double layer capacitor. *Bioresource Technology*, **409**, 131251.
19. Devi, R., Kumar, V., Kumar, S., Bulla, M., & Mishra, A. K. (2024). Performance optimization of the symmetric supercapacitors based on paddy straw-derived porous activated carbon. *Journal of Energy Storage*, **79**, 110167.
20. Kumar, K., Saxena, R. K., Kothari, R., Suri, D. K., Kaushik, N. K., & Bohra, J. N. (1997). Correlation between adsorption and X-ray diffraction studies on viscose rayon based activated carbon cloth. *Carbon*, **35**(12), 1842–1844.
21. Tadesse, M. G., Kasaw, E., & Lübben, J. F. (2023). Valorization of banana peel using carbonization: Potential use in the sustainable manufacturing of flexible supercapacitors. *Micromachines*, **14**(2), 330.
22. Li, W., Chen, C., Wang, H., Li, P., Jiang, X., Yang, J., & Liu, J. (2022). Hierarchical porous carbon induced by inherent structure of eggplant as sustainable electrode material for high performance supercapacitor. *Journal of Materials Research and Technology*, **17**, 1540–1552.
23. Ozpinar, P., Dogan, C., Demiral, H., Morali, U., Erol, S., Samdan, C., Yildiz, D., & Demiral, I. (2022). Activated carbons prepared from hazelnut shell waste by phosphoric acid activation for supercapacitor electrode applications and comprehensive electrochemical analysis. *Renewable Energy*, **189**, 535–548.
24. Taer, E., Deraman, M., Taslim, R., & Iwantono. (2013). Preparation of binderless activated carbon monolith from pre-carbonization rubber wood sawdust by controlling of carbonization and activation condition. *AIP Conference Proceedings*, **1554**(1), 33–37.
25. Yue, W., Yu, Z., Zhang, X., Liu, H., Zhang, Y., & Ma, X. (2024). Preparation of natural N/O/S co-doped biomass-derived carbon materials for supercapacitors using multistage gas self-exfoliation effect. *Journal of Analytical and Applied Pyrolysis*, **179**, 106525.
26. Rahim, A. H. A., Ramli, N., Nordin, A. N., & Wahab, M. F. A. (2021). Supercapacitor performance with activated carbon and graphene nanoplatelets composite electrodes, and insights from the equivalent circuit model. *Carbon Trends*, **5**, 100101.
27. Joseph, S., Singh, G., Lee, J. M., Yu, X., Breese, M. B., Ruban, S. M., Bhargava, S. K., Yi, J., & Vinu, A. (2023). Hierarchical carbon structures from soft drink for multi-functional energy applications of Li-ion battery, Na-ion battery and CO_2 capture. *Carbon*, **210**, 118085.
28. Bandara, T. M. W. J., Alahakoon, A. M. B. S., Mellander, B. E., & Albinsson, I. (2024). Activated carbon synthesized from Jack wood biochar for high performing biomass derived composite double layer supercapacitors. *Carbon Trends*, **15**, 100359.
29. Ahmad, N., Rinaldi, A., Sidoli, M., Magnani, G., Morenghi, A., Scaravonati, S., Vezzoni, V., Pasetti, L., Fornasini, L., Ridi, F., Milanese, C., & Pontiroli, D. (2024). High performance quasi-solid-state supercapacitor based on activated carbon derived from asparagus waste. *Journal of Energy Storage*, **99**, 113267.

30. Chaiammart, N., Vignesh, V., Thu, M. M., Eiad-ua, A., Maiyalagan, T., & Panomsuwan, G. (2024). Chemically activated carbons derived from cashew nut shells as potential electrode materials for electrochemical supercapacitors. *Carbon Resources Conversion*, 100267.

31. Rustamaji, H., Prakoso, T., Devianto, H., Widiatmoko, P., Febriyanto, P., & Eviani, M. (2024). Modification of hydrochar derived from palm waste with thiourea to produce N, S co-doped activated carbon for supercapacitor. *Sustainable Chemistry for the Environment*, **7**, 100132.

Indonesian Physics Communication
Department of Physics, Universitas Riau, Pekanbaru, Indonesia
p-ISSN 1412-2960 | e-ISSN 2579-521X
Vol. 21 | No. 3
November 2024
Web: https://kfi.ejournal.unri.ac.id
E-mail: kfi@ejournal.unri.ac.id

Preparation and characterization of Cr-TiO_2/α-Fe_2O_3 nanocomposite for methylene blue degradation

Teguh P. Hadilala[1,*], **Erwin Amiruddin**[1,*], **Amir Awaluddin**[2], **Rahmondia Nanda Setiadi**[1]
[1]Department of Physics, Universitas Riau, Pekanbaru 28293, Indonesia
[2]Department of Chemistry, Universitas Riau, Pekanbaru 28293, Indonesia

*Corresponding author: erwin.amiruddin@lecturer.unri.ac.id; teguh.p7850@grad.unri.ac.id

ABSTRACT

In this study, Cr-TiO_2/α-Fe_2O_3 nanocomposite was prepared by the ball milling method, incorporating chromium, titanium dioxide (TiO_2), and iron oxide (α-Fe_2O_3) nanoparticles extracted from Logas-Kuansing natural sand. The structural, magnetic, morphological, and optical properties of these nanocomposites were investigated using X-ray diffraction (XRD), vibrating sample magnetometer (VSM), scanning electron microscopy (SEM), and UV-Vis spectroscopy. XRD revealed that both the pure and chromium-added nanocomposites have a hexagonal structure, with a crystalline size reduction from 17.5 nm to 19.7, 19.5, and 19.4 nm for the pure and chromium-added samples with chromium concentrations of 0, 5, 10, and 15 wt.%, respectively. Magnetic properties were analyzed through hysteresis loops using VSM, revealing coercivity, saturation magnetization, and remanence magnetization in the ranges of 131 – 247 Oe, 0.80 – 0.54 emu/g, and 0.097 – 0.116 emu/g, respectively. SEM analysis confirmed that the particle shape and size are within the nanometer scale. The optical band gap, estimated using the Tauc relation, decreased from 1.93 eV for the pure nanocomposite to 1.74, 1.68, and 1.72 eV for 5, 10, and 15 wt.% chromium-added nanocomposites, respectively. This study suggests that the prepared Cr-TiO_2/α-Fe_2O_3 nanocomposite exhibits promising physical properties as a catalyst for the degradation of methylene blue.

Keywords: Ball milling; Cr-TiO_2/α-Fe_2O_3; Logas natural sand; nanocomposite

Received 06-09-2023 | Revised 15-10-2023 | Accepted 02-11-2024 | Published 30-11-2024

INTRODUCTION

The rapid growth of industries in recent decades has been remarkable. The discharge of several hazardous dyes from various textile industries into wastewater is a major cause of serious environmental problems that affect human health and aquatic ecosystems, due to the toxicity and carcinogenic effects of these substances. The pollutants released by these industries include oils, pharmaceuticals, cosmetics, photochemicals, and textile effluents [1, 2]. The most commonly used dye in the textile industry is methylene blue (MB). MB is a cationic dye widely used in various industries, including textiles, paper, and plastics. MB is known to be toxic, carcinogenic, and mutagenic [3]. Nanocomposites have garnered significant attention for their potential in environmental remediation, particularly for degrading organic pollutants. Recycling nanocomposites enhances water purification, making it more eco-friendly, efficient, and cost-effective [4]. Natural iron sand contains iron oxide compositions, including magnetite (Fe_3O_4), maghemite (γ-Fe_2O_3), and hematite (α-Fe_2O_3) [5].

Among the various types of metal oxides, iron oxides such as α-Fe_2O_3 are considered one of the most important oxides due to their numerous technological applications ranging from catalysts to biomedical applications and environmental remediation [6]. Hematite (α-Fe_2O_3), as the most stable iron oxide with n-type semiconductor properties (for example = 2.1 eV) [7]. Hematite has a low cost and high corrosion resistance, making it an attractive material for various applications, such as catalysts, pigments, and gas sensors [8]. For a compound to show the photocatalytic property, it should be a semiconductor with a sufficient band gap to degrade dyes. Metal oxides such as TiO_2, are widely used due to their photocatalytic, catalytic activity, water splitting properties, nontoxicity, low-cost, and stability [9]. Coupling hematite with other semiconductor with higher band gap energy can increase the photocatalytic activity. TiO_2 with high band energy gap (3.0 – 3.2 eV) is suitable for coupling with hematite [10]. Previous researchers used nanocomposites and metal oxides for the photocatalytic degradation of dyes, enhancing activity with transition metals Ag and Au [11, 12]. There are several methods for preparing α- Iron oxide derived from natural sand can be prepared using methods such as high energy milling (HEM), top down, and ball milling. Ball milling is the best choice for nanoparticle preparation because it is simple, efficient, and cost-effective [13].

In this study, iron oxide nanoparticles (α-Fe_2O_3) were prepared from natural sand in Logas Village, Logas Tanah Darat District, Kuantan Singingi Regency, Riau Province, with the addition of titanium dioxide (TiO_2) nanoparticles in a weight percentage (wt.%) ratio of 65:35 using a simple, efficient, and cost-effective ball milling method to obtain the magnetic nanocomposite TiO_2/α-Fe_2O_3. Subsequently, chromium (Cr) nanoparticles were added in wt.% to form the Cr-TiO_2/α-Fe_2O_3 nanocomposite. We investigated the structural, magnetic, morphological, and optical properties of the magnetic Cr-TiO_2/α-Fe_2O_3 nanocomposite, which serves as an effective photocatalyst for the degradation of MB.

EXPERIMENTAL PROCEDURE

Raw Material and Chemical

The raw material used for preparing α-Fe_2O_3 nanoparticles is natural sands collected from Logas Village, Kuansing District, Riau Province. The chemical used for the mixture of α-Fe_2O_3 nanoparticles to form a nanocomposite is titanium dioxide with the addition of chromium with a purity of 99.99%.

Preparation of Cr-TiO_2/α-Fe_2O_3

The separation of iron oxide and non-iron oxide particles was carried out using an iron sand separator (ISS) and NdFeB magnet. The ball milling process was conducted in three stages, each lasting 50 hours, with the separation of iron oxide and non-iron oxide particles at each stage. The product from the fourth stage of ball milling (BM 4) was combined with TiO_2 nanoparticles in a 65 : 35 wt.% ratio and divided into five equal parts by mass. The TiO_2/α-Fe_2O_3 nanocomposite was then further divided into five equal parts and doped with Cr nanoparticles at concentrations of 0, 5, 10, and 15 wt.%. Next, ball milling was performed for 20 hours on each sample, resulting in Cr-TiO_2/α-Fe_2O_3 nanocomposites. The structural, magnetic, morphological, and optical properties of the nanocomposites without Cr and with added Cr were analyzed using X-ray diffraction (XRD), vibrating sample magnetometer (VSM), scanning electron microscope (SEM), and UV-Vis spectrometer.

RESULTS AND DISCUSSION

Structural Analysis

The XRD patterns of the nanocomposites (TiO_2/α-Fe_2O_3) without and with chromium added at various compositions are shown in Figure 1.

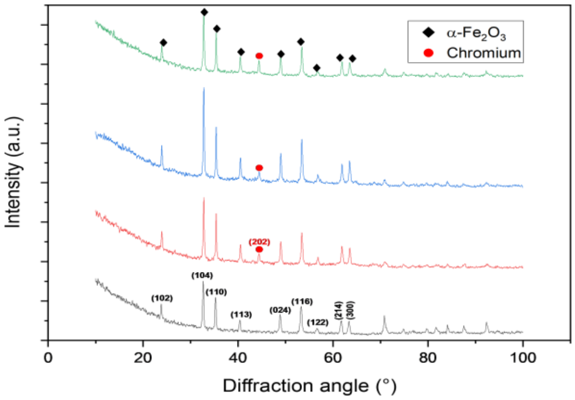

Figure 1. XRD patterns of TiO_2/α-Fe_2O_3 nanocomposites: (a) without chromium and with chromium added at compositions of; (b) 5 wt.%; (c) 10 wt.%; and (d) 15 wt.%.

The patterns were obtained using a Philips X-Ray Diffractometer equipped with Cu Kα radiation with a wavelength of 1.5406 Å. The diffraction patterns of the $TiO_2/\alpha\text{-}Fe_2O_3$ nanocomposites show diffraction peak angles at 23.81°, 32.64°, 35.25°, 40.36°, 48.82°, 53.25°, 56.68°, 61.82°, and 63.36°, which can be indexed to the crystal planes (102), (104), (110), (113), (024), (116), (122), (214), and (300). These peak positions correspond to the standard Bragg positions of hexagonal $\alpha\text{-}Fe_2O_3$, in agreement with JCPDS No. 89-8103.

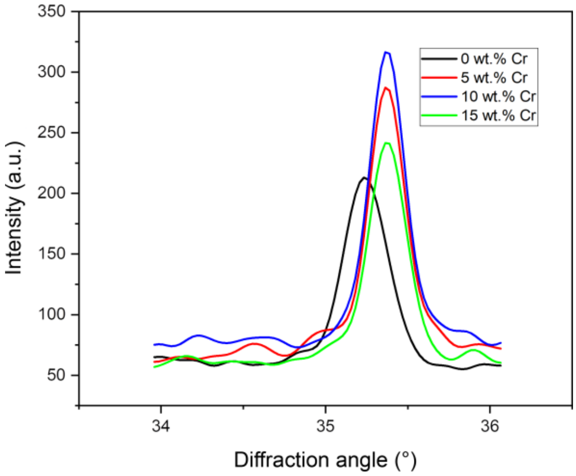

Figure 2. Enlarged diffraction angle from 35.0° to 35.6°, showing a shift of the peak position to a slightly higher angle.

The average crystallite size estimated using the Scherrer formula for the nanocomposites without chromium is 17.5, 19.7, 19.5, and 19.4 nm for chromium compositions of 0, 5, 10, and 15 wt.%, respectively. Additionally, the peak intensity was found to increase, indicating a reduction in crystallite size with the addition of chromium. The XRD pattern also confirmed the presence of an additional diffraction peak at 2θ = 44.37° in the chromium-doped samples. This low-intensity diffraction peak, shown in Figure 1 (b), (c), and (d), indicates the presence of metallic chromium nanoparticles in the samples. Therefore, the presence of diffraction peaks associated with chromium nanoparticles, titanium dioxide, and hematite indicates the success of the ball milling method in forming $Cr\text{-}TiO_2/\alpha\text{-}Fe_2O_3$ nanocomposites. As the chromium composition increased, the intensity of the (110) peak was found to increase, as clearly seen in Figure 1. The XRD patterns of the nanocomposites ($TiO_2/\alpha\text{-}Fe_2O_3$) without and with added chromium at different concentrations are shown in Figure 1 and 2.

Magnetic Properties

Figure 3 shows the magnetization (M) curves as a function of the applied magnetic field (H) for the nanocomposites without chromium and with chromium additions (0, 5, 10, and 15 wt.%). The measurements were performed using a VSM in an applied magnetic field ranging from -20 kOe to +20 kOe. The saturation magnetization of the samples was calculated from the magnetization plot against the applied magnetic field. As shown in Figure 3, the magnetization behavior as a function of the applied magnetic field exhibits hysteresis, with the magnetization of the nanocomposites increasing as the applied magnetic field increases and reaching saturation at a high field of 20 kOe. From the Figure 3, it is clear that the samples exhibit ferromagnetic behavior. The saturation magnetization (Ms) and remanent magnetization (Mr) of the sample without chromium (Ms = 0.80 emu/g and Mr = 0.097 emu/g), respectively, decrease with increasing chromium content.

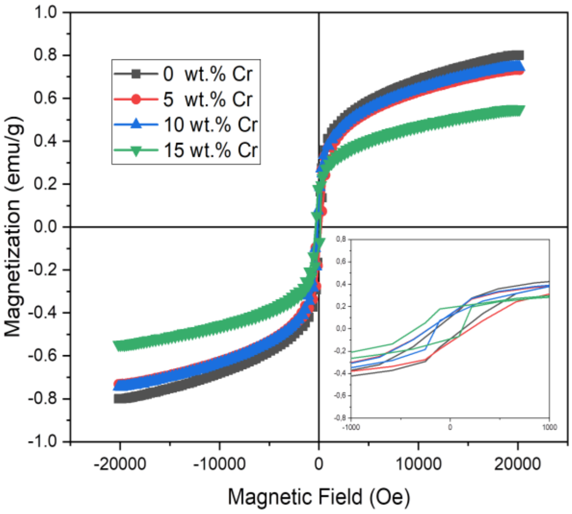

Figure 3. Hysteresis curves of the nanocomposites without and with chromium addition, with an inset showing the enlarged loop of these samples.

The coercivity increases with the addition of chromium, which is attributed to the crystallite size and morphology of the samples, as shown in Figure 4. The increase in the nonmagnetic phase content leads to greater segregation among the nanocomposites, ultimately reducing the magnetization values.

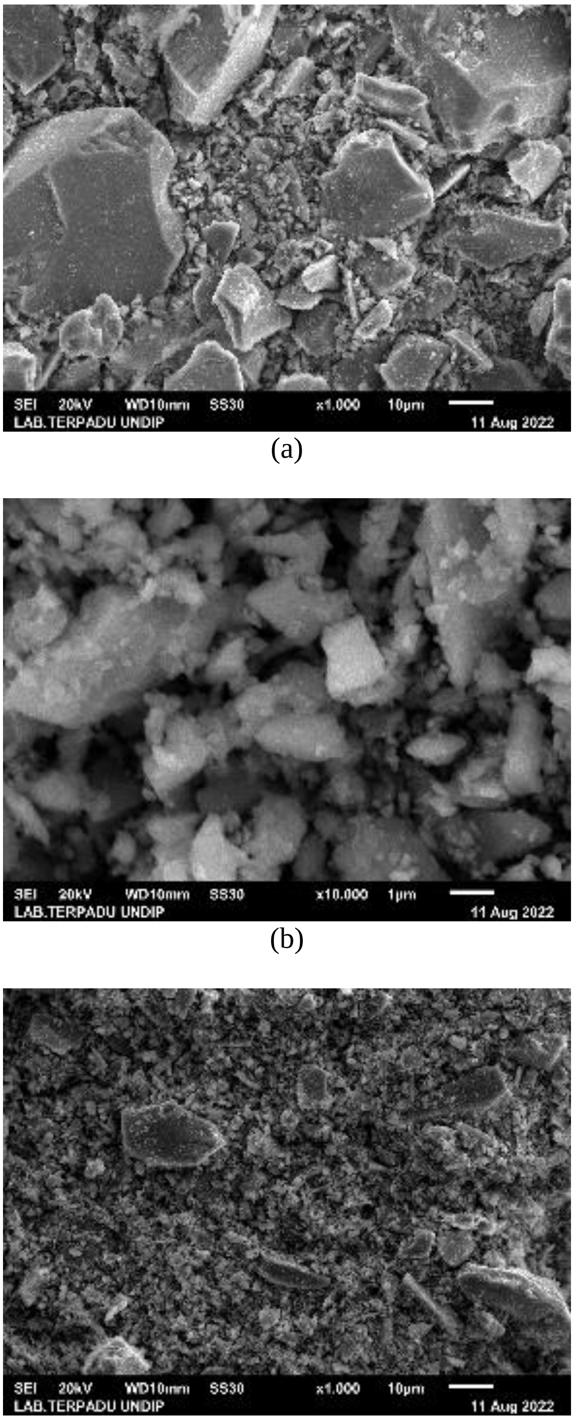

(a)

(b)

(c)

Figure 4. SEM images of: (a) nanocomposites without Cr; (b) nanocomposites with 10 wt.% Cr; and (c) nanocomposites with 15 wt.% Cr.

Optical Properties

The effect of chromium addition (10 and 15 wt.%) on the optical properties of the nanocomposites was studied based on optical absorption measurements using a UV-Vis spectrometer. The optical absorption spectra of the nanocomposites without chromium and with chromium additions at 5, 10, and 15 wt.% as a function of wavelength, as well as the optical band gap with the average crystallite size and absorption peak as a function of chromium composition, are shown in Figures 5 (a) and 5 (b), respectively.

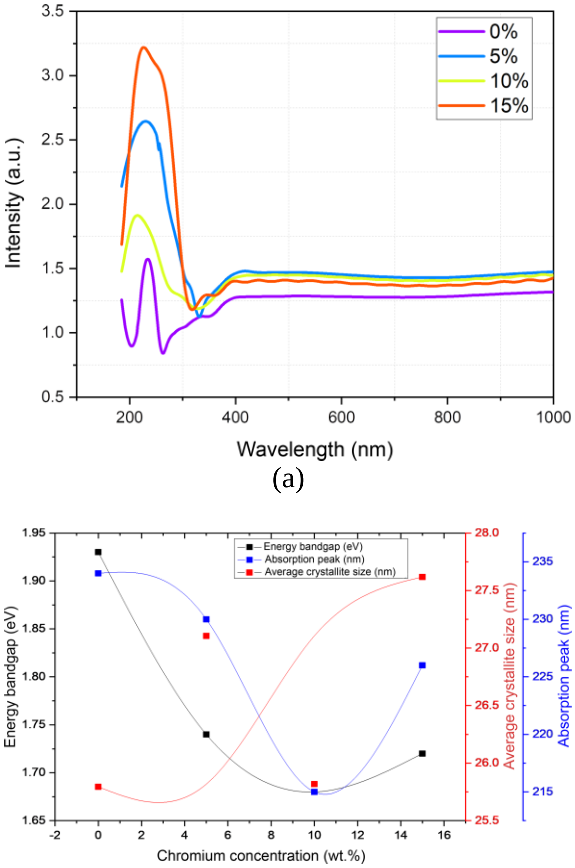

(a)

(b)

Figure 5. (a) Absorption spectra of the nanocomposites without chromium and with chromium addition at various compositions; and (b) variation of crystallite size with the optical band gap and absorption peak as a function of chromium composition.

A strong absorption at wavelengths of 234, 230, 215, and 226 nm was observed in the nanocomposites for chromium additions of 0, 5, 10, and 15 wt.%, respectively. This strong absorption was found to shift towards higher wavelengths, corresponding to lower energy, with increasing chromium concentration, resulting in greater methylene blue degradation.

The optical band gap was obtained by plotting $(\alpha h\nu)^2$ against photon energy (hν) and extrapolating the linear region ($\alpha = 0$). The optical band gap was estimated using the Tauc equation:

$$\alpha h v = A\sqrt{E_g - hv} \qquad (1)$$

where *h* is Planck's constant, *v* is the frequency, *α* is the absorption coefficient, and *n* is either 1/2 for direct transitions or 2 for indirect transitions.

The direct band gap of the nanocomposites is shown in Figure 6. The results indicate that the optical band gap calculated through UV-Vis spectroscopy decreased from 1.93 to 1.72 eV as the chromium composition increased from 0 to 15 wt.%. The addition of chromium can narrow the optical band gap of iron oxide nanoparticles. Figure 5 (b) shows the variation of average crystallite size with the optical band gap of the nanocomposites with chromium addition. The band gap of the nanocomposites without chromium and with chromium addition decreased. Therefore, the crystallite size reduced the band gap of the nanoparticles. This is due to the reduction in particle size and average crystallite size, causing the material's band gap to decrease, where the valence band shifts to lower energy and the conduction band shifts to higher energy, resulting in greater methylene blue degradation.

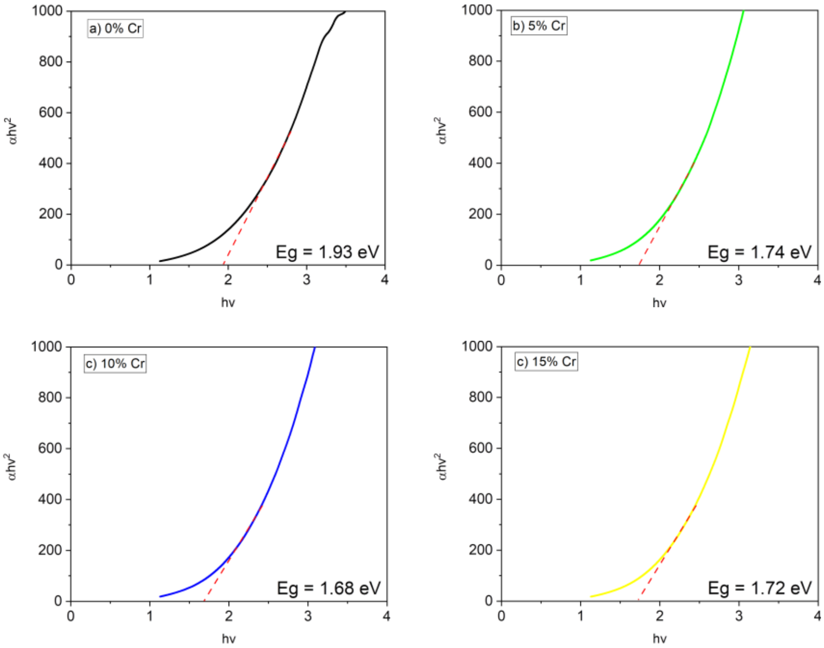

Figure 6. Band gap energy of the nanocomposites without and with chromium addition at various weight percentages.

CONCLUSION

$TiO_2/\alpha\text{-}Fe_2O_3$ nanocomposites with various chromium weight percentages ranging from 0 wt.% to 15 wt.% were successfully synthesized using the ball milling method for methylene blue degradation. Structural characterization studies using XRD revealed that all samples exhibited high crystallinity with a rhombohedral structure. The average crystallite size tended to decrease with increasing chromium content. The success of the ball milling method in forming chromium-added nanocomposites was indicated by the presence of diffraction peaks associated with chromium nanoparticles and $TiO_2/\alpha\text{-}Fe_2O_3$. Magnetic property studies confirmed the ferromagnetic nature of the samples. The morphological properties showed that nanocomposite agglomeration was more dominant in samples without chromium addition. The optical band gap obtained from Tauc plots showed a decrease with increasing chromium concentration. The results demonstrate that the Cr-TiO_2/α-Fe_2O_3 nanocomposites obtained via this simple ball milling method have the potential as catalysts for methylene blue degradation.

REFERENCES

1. Alwera, S., Talismanov, V. S., Alwera, V., & Domyati, D. (2023). Synthesis and characterization of Sn-doped CeO_2-Fe_2O_3 nanocomposite and application in photocatalytic degradation of Sudan I. *Biointerface Res. Appl. Chem.*, **13**, 179.
2. Ahmed, M. A., El-Katori, E. E., & Gharni, Z. H. (2013). Photocatalytic degradation of methylene blue dye using Fe_2O_3/TiO_2 nanoparticles prepared by sol–gel method. *J. Alloys Compd.*, **553**.
3. Fito, J., Abrham, S., & Angassa, K. (2020). Adsorption of methylene blue from textile industrial wastewater onto activated carbon of *Parthenium hysterophorus*. *Int. J. Environ. Res.*, **14**, 501–511.
4. Tajareh, A. V., Ganjidoust, H., & Ayati, B. (2019). Synthesis of TiO_2/Fe_3O_4/MWCNT magnetic and reusable nanocomposite with high photocatalytic performance in the removal of colored combinations from water. *J. Water Environ. Nanotechnol.*, **4**(3), 198–212.
5. Widodo, R. D., Anis, S., Ichwani, A. A., Setiawan, B., Fitriyana, D. F., & Rochman, L. (2020). Synthesis and characterization of iron (III) oxide from natural iron sand of the south coastal area, Purworejo Central Java. *J. Phys. Conf. Ser.*, **1444**(1), 012043.
6. Erwin, A., Sinuraya, S., Awaluddin, A., Rianna, M., Hadianto, H., Rizki, M., Purba, N. M., & Sitorus, I. T. (2023). Chromium doped iron oxide nanoparticles and physical properties prepared from Logas natural sand and their application in photo-Fenton degradation of methylene blue dye. *ARPN J. Eng. Appl. Sci.*, **18**(10).
7. Ahmad, W. R. W., Mamat, M. H., Zoolfakar, A. S., Khusaimi, Z., & Rusop, M. (2016). A review on hematite α-Fe_2O_3 focusing on nanostructures, synthesis methods and applications. *2016 IEEE Student Conference on Research and Development*, 1–6.
8. Kumar, S., Kumar, M., & Singh, A. (2021). Synthesis and characterization of iron oxide nanoparticles (Fe_2O_3, Fe_3O_4): A brief review. *Contemp. Phys.*, **62**(3).
9. Uzunbayir, B., Kartal, U., Doluel, E. C., Yurddaskal, M., & Erol, M. (2020). Development of α-Fe_2O_3/TiO_2 3D hierarchical nanostructured photocatalysts through electrochemical anodization and sol–gel methods. *J. Sol-Gel Sci. Technol.*, **96**, 441–451.
10. Lubis, S., & Maulana, I. (2018). Synthesis and characterization of TiO_2/α-Fe_2O_3 composite using hematite from iron sand for photodegradation removal of dye. *Jurnal Natural*, **18**(1), 38–43.
11. Mirzaei, A., Janghorban, K., Hashemi, B., Bonavita, A., Bonyani, M., Leonardi, S. G., & Neri, G. (2015). Synthesis, characterization and gas sensing properties of Ag@α-Fe_2O_3 core–shell nanocomposites. *Nanomaterials*, **5**(2).
12. Saber, B. & Mezni, A. (2021). Preparation and characterization of Ag@TiO_2/α-Fe_2O_3 Ternary nanocomposite for enhanced visible light photocatalytic performance. *J. Nanomater.*, **2021**, 12345.
13. Royka, A. & Amiruddin, E. (2021). Penentuan nilai suseptibilitas dan ukuran partikel magnetik pasir alam Logas Kabupaten Kuantan Singingi menggunakan variasi ukuran ball milling. *Komunikasi Fisika Indonesia*, **18**(1).

IPC
Indonesian Physics Communication
Department of Physics, Universitas Riau, Pekanbaru, Indonesia
p-ISSN 1412-2960 | e-ISSN 2579-521X
Vol. 21 | No. 3
November 2024
Web: https://kfi.ejournal.unri.ac.id
E-mail: kfi@ejournal.unri.ac.id

N-doped porous activated carbon from rubber seed shells (*Hevea brasiliensis*) as high-energy supercapacitor material

Siti Rahma Daulay, Rakhmawati Farma, Awitdrus*
Department of Physics, Universitas Riau, Pekanbaru 28293, Indonesia

*Corresponding author: awitdrus@lecturer.unri.ac.id

ABSTRACT

Biomass is an environmentally safe and cost-effective source of activated carbon (AC) for supercapacitors (SC). In this study, AC was generated using precarbonisation and activation with KOH using rubber seed shell (RSS) as a precursor. The electrochemical performance was investigated by cyclic voltammetry and galvanostatic charge-discharge determination and the ACs were characterised using FTIR analysis technique. RSS materials were prepared by varying calcination temperatures of 700°C, 800°C, and 900°C without doping. RSS_{800} shows a maximum specific capacitance of 190 F/g and has an energy density of 26.2 Wh/kg and a power density of 695.4 kW/kg at 1 A/g. Furthermore, melamine was used as an external dopant source for the N-doping process. The doped AC sample ($RSS_{800\text{-}90}$) had a specific capacitance of 288 F/g and has an energy density of 40.9 Wh/kg and a power density of 515.4 kW/kg at 1 A/g in H_2SO_4 electrolyte. N-doped with melamine as nitrogen source was successfully incorporated into AC to produce high-performance electrodes for SC.

Keywords: Activated carbon; KOH; N-doped; rubber seed shell; supercapacitors

Received 06-09-2023 | Revised 17-10-2023 | Accepted 04-11-2024 | Published 30-11-2024

INTRODUCTION

The knowledge and demand for energy storage systems that are efficient, sustainable and environmentally friendly is increasing due to technological advancements in various industrial sectors, so the exploration of renewable energy sources that are environmentally friendly is essential for the long-term economic growth of society [1, 2]. Supercapacitors (SC) are one that has attracted great attention as an environmentally friendly, efficient and effective option because they have excellent power density and a long lifetime [3].

In general, electrode materials for SC include activated carbon (AC), metal oxides, polymers, graphene, etc. AC has proven to be an excellent electrode material when compared to other types of carbon materials. Environmental pollution and the depletion of fossil fuel reserves are the reasons why researchers are exploring biomass waste as a potential alternative for producing AC. Various biomass wastes such as wood [4], empty oil palm sign [5], coconut shells [6], eggshells [7], has been converted to AC to serve as the electrode material for SC.

AC can be produced using physico-chemical activation techniques. In the chemical activation technique, biomass as a precursor will be combined with chemical activators, such as H_2SO_4, H_3PO_4, KOH, NaOH, and $ZnCl_2$ [8, 9]. Compared to other activating agents, KOH is one of the most effective and environmentally friendly, making it more ideal for use in the chemical activation process for AC manufacturing [9, 10]. Physical activation techniques can be performed using oxidising agents, such as carbon dioxide (CO_2), water vapour, air, or a combination of these gases. CO_2 is often chosen as an activation agent due to its safe and contains no toxins nature [11]. Activation temperature, the amount of activating agent, as well as heat pretreatment, all affect porosity formation during the activation process using KOH and CO_2 [12]. Heteroatom doping is one way to increase the energy storage capacity of carbon-based

©Author(s) | DOI: 10.31258/jkfi.21.3.211-218

electrodes and improve the electron transport rate. The increase in apparent capacitance is obtained under Faraday reaction conditions while maintaining the EDLC features [13, 14].

Heteroatoms can be introduced into the AC framework by changing the electron distribution and bonding properties of the surrounding carbon lattice. Elements such as N, P, S, and B are added into the carbon structure to modify its Fermi level shift and electronic structure [15, 16]. In addition, heteroatom functional groups not only reduce the resistance to charge transfer at the electrode, but also increase the wettability of the carbon network to improve the performance of the material. Nitrogen-doped carbon can be synthesised via thermal methods using nitrogen-containing compounds, such as ammonia gas (NH_3), melamine, urea, and acetonitrile [17].

Melamine-based nitrogen doping has been investigated to improve the performance of SC electrodes. For instance, Tran et al., successfully used the melamine as a nitrogen source synthesis of activated carbon from oil palm empty fruit bunches and its modification with nitrogen doping for supercapacitor applications a specific capacitance 182 to 217 F/g [18]. Kong et al. (2024), N doped porous carbon synthesised via Lewis acid salt activation for supercapacitors with high rate performance of 234 F/g [19].

Rubber seed shell (*Hevea brasiliensis*) is one of the flowering plants of the Moraceae family endemic to the eastern part of Southeast Asia and South Asia. Rubber seed shell (RSS) consists of 48.64% cellulose, 33.54% lignin, and 18.0% hemicellulose. However, RSS is often dumped on the ground and decomposes without optimal utilisation, resulting in a large amount of waste. Therefore, RSS was chosen as a carbon precursor for the manufacture of AC as a SC electrode in this study. This study aims to produce activated carbon from Hevea brasiliensis biomass through a combination of one-stage activation techniques using KOH and CO_2, and implement it as an electrode material for supercapacitors.

MATERIALS AND METHODS

RSS waste was collected from Sidokan Panompuan Village, Padang Lawas Regency, North Sumatra Province. The RSS was cleaned using deionised water to remove impurities, then dried in the sun for 5 days, followed by oven drying for 2 days. Next, the RSS was carbonised at 250°C for 3 hours, pulverised using ball milling to obtain fine powder, and sieved to a size of 53 µm. A total of 30 g of activated carbon powder was then activated with 150 ml of 0.5 M KOH solution and heated for 2 hours. The activated samples were cooled to room temperature, then dried in an electric oven overnight. After drying, the samples were shaped into coins and put into a horizontal furnace for activation at 700°C under CO_2 gas flow. The product is washed to a neutral pH (pH~7) and labelled as RSS_{700}. By repeating the same steps, activation was carried out at 800°C and 900°C, which were labelled as RSS_{800} and RSS_{900}, respectively. By repeating the steps, 0.3 g of melamine was dissolved in 100 ml of deionised water and heated for 10 minutes. In the doping process, 20 coin samples were immersed in the solution for 24 hours and dried overnight. Next, the dried coin samples were heated at 300°C in an N_2 atmosphere for different times (60, 90, and 120 minutes). The resulting products were labelled as RSS_{800-60}, RSS_{800-90}, and $RSS_{800-120}$.

RESULTS AND DISCUSSION

Fourier Transform Infrared Spectroscopy

Infrared spectroscopy is the most commonly used spectroscopic technique to measure the IR frequencies of AC chemical functional groups. In Figures 1 (a) and (b) shows, the vibrations detected on activated carbon are: C=C=C stretching vibrations at 2109 – 2114 cm^{-1}, C=C bond stretching vibrations (in alkynes) at 1992 – 1994 cm^{-1} [20]. The Fourier transform infrared spectroscopy (FTIR) spectrum shows a relatively weak signal with several bands in the 1500 – 2000 cm^{-1} range, which are usually associated with C–C and C=O stretching, as is often found in almost pure amorphous carbon [21] before and after N-doped using melamine that changes only the wavelength.

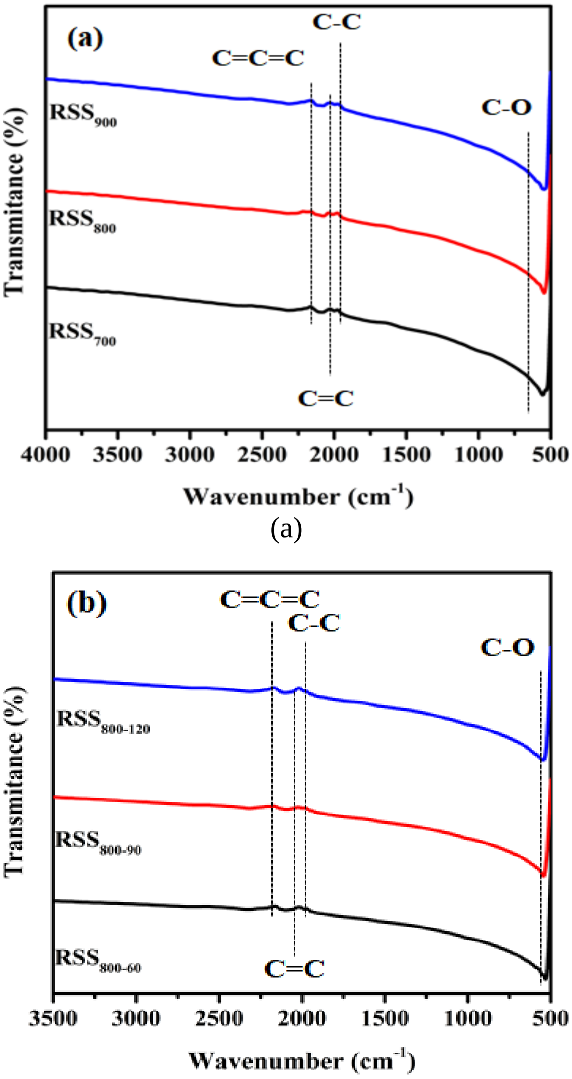

(a)

(b)

Figure 1. FTIR: (a) before N-doped; (b) and after N-doped.

Cyclic Voltammetry

Cyclic voltammetry (CV) is a method used to determine the electrochemical properties and capacitance value of an electrode by providing a voltage variation at each unit time. The electrochemical characteristics of the RSS electrode without doping are shown in Figure 2(a), the highest capacitance value is found in RSS_{800} which is a normal rectangular shape showing typical electric double layer capacitance (EDLC) behaviour. The CV curve shows the quasi-rectangular shape of the current response on reversal. Voltage without obvious redox peaks which confirm the good EDLC character of the electrode [22]. The CV curves of RSS_{800} at various scanning speeds (1, 2, 5 and 10 mV/s) are shown in Figure 2 (b). Furthermore, the CV curves of the RSS samples after doping RSS_{800-60}, RSS_{800-90}, and $RSS_{800-120}$ Figure 2 (c) show a rectangular shape with a fairly clear redox peak, showing the merging of EDLC and pseudo-capacitance behaviour. This redox peak could be due to the doping effect of melamine as the dopant source [23]. Compared with other samples, the RSS_{800-90} curve has a larger integral area, thus indicating better electrochemical performance. The CV curves at various scanning speeds (1, 2, 5 and 10 mV/s) are shown in Figure 2 (d).

Galvanostatic Charge-Discharge

Galvanostatic charge-discharge (GCD) is one of the most useful techniques to calculate electochemical capacitance under controlled current conditions [24]. Figure 3 (a) RSS_{800} shows the GCD curve is symmetrically triangular even at high current densities, which demonstrates excellent rate capability compared to the other two electrodes [25]. The GCD curves of RSS_{800} at various curent densities (1, 2, 5, and 10 A/g) are shown in Figure 3 (b). In Figure 3 (c) all electrodes show a triangular shape with a smaller IR drop, indicating high colombic efficiency [26]. The presence of heteroatoms and surface functional groups activate various Faraday processes, which favour the functioning of the EDLC system. The longer charge and discharge duration of RSS_{800-90} indicates superior capacitive performance and is in agreement with the results of CV curve analysis. Moreover, the addition of nitrogen into the carbon structure is able to increase the moisture retention capacity and conductivity of the carbon material, which ultimately improves the electrochemical performance [27]. The GCD curves of RSS_{800-90} at at various curent densities (1, 2, 5, and 10 A/g are shown in Figure 3 (d).

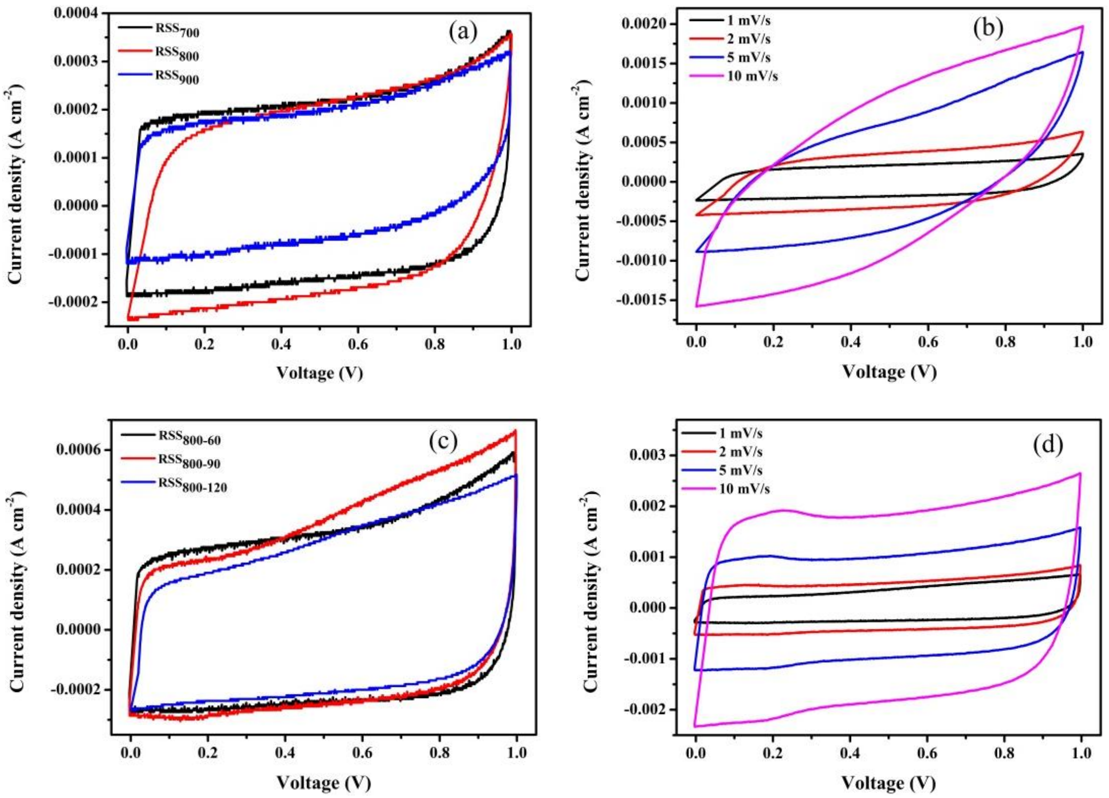

Figure 2. CV curve of: (a) RSS electrodes; (b) RSS_{800} at various scan rates; (c) RSS after N-doped electrodes; and (d) $HB_{800\text{-}90}$ at various scan rates.

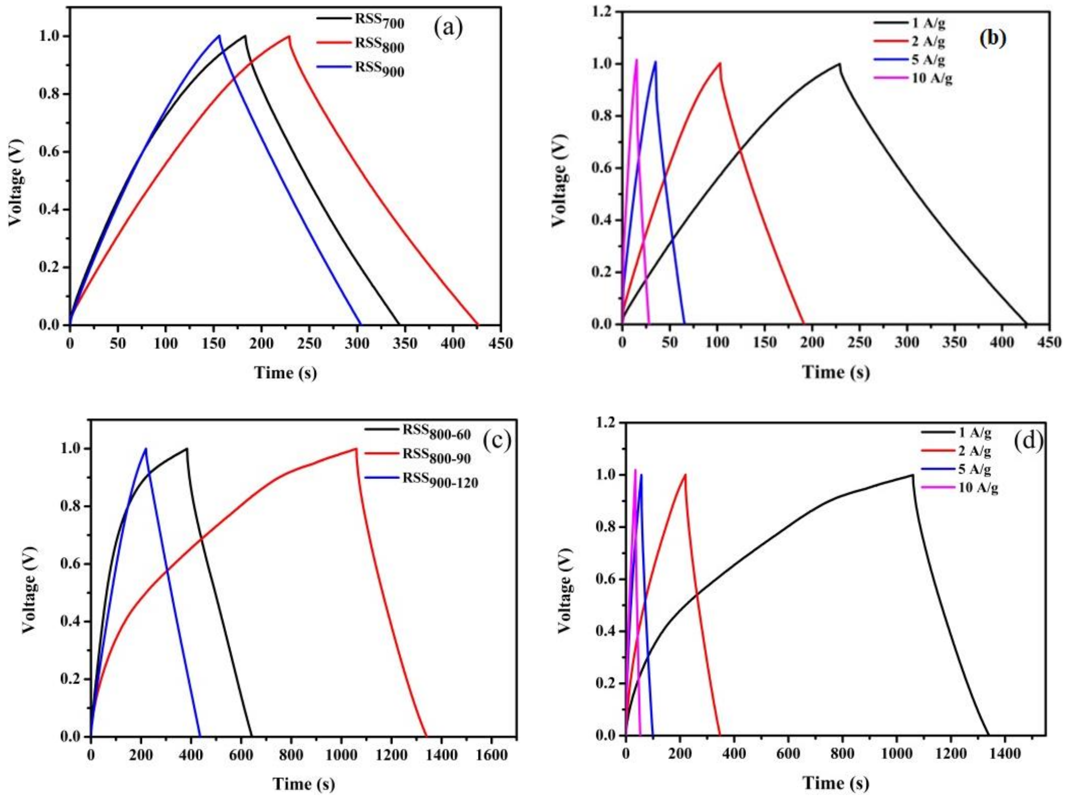

Figure 3. GCD curve of: (a) RSS electrodes; (b) RSS_{800} at various curent densities; (c) RSS after N-doped electrodes; and (d) $HB_{800\text{-}90}$ at various curent densities.

The longer charge-discharge duration of RSS_{800-90} indicates superior capacitive performance and agrees with the CV curve analysis results. The specific capacitance (C_{sp}), energy density (E_d), and power density (P_d) are obtained from the GCD curve and calculated using specific formulae [28, 29].

$$C_s = 2I\Delta t / m\Delta V \quad (1)$$

$$E_d = CV^2 / 7.2 \quad (2)$$

$$P_d = 3600 \frac{E}{\Delta t} \quad (3)$$

where, I (A) is the discharge current, Δt (s) is the discharge duration, ΔV (V) is the potential range during discharge, and m (g) is the electrode mass. The C_{sp}, E_d, and P_d values of all RSS electrodes can be seen in Table 1.

Tabel 1. Values of specific capacitance (C_{sp}), energy density (E_d), and power density (P_d).

Sample	C_{sp} (F/g)	P_{sp} (W/kg)	E_{sp} (Wh/kg)
RSS_{700}	165	513.3	22.9
RSS_{800}	190	695.4	26.2
RSS_{900}	151	511.7	20.9
RSS_{800-60}	266	513.8	36.8
RSS_{800-90}	288	515.4	40.9
$RSS_{800-120}$	220	510.2	30.6

CONCLUSION

Biomass activated carbon derived from rubber seed shells through the combination of heteroatom doping has been successfully fabricated and analysed. In addition, melamine used as an external dopant source for N doping process can improve the capacitive behaviour of SC. AC without doping treatment (RSS_{800}) has a specific capacitance of 190 F/g and AC with doping treatment ($RSS_{800-900)}$ has a specific capacitance of 288 F/g at 1 A/g, respectively. In summary, N-doped with melamine as nitrogen source was successfully incorporated into AC to improve the capacitive properties of the electrode. This research may provide a new approach for the fabrication of N-doped ACs using external dopant sources and implemented as SC electrode materials.

ACKNOWLEDGMENTS

The authors would like to thank DRTPM-Kemdikbudristek of the Republic of Indonesia for financial support through the 2024 master's thesis research grant (Contract No: 083/E5/PG.02.00.PL/2024 and 20721/UN.19.5.1.3/AL.04/2024).

REFERENCES

1. Han, G., Jia, J., Liu, Q., Huang, G., Xing, B., Zhang, C., & Cao, Y. (2022). Template-activated bifunctional soluble salt $ZnCl_2$ assisted synthesis of coal-based hierarchical porous carbon for high-performance supercapacitors. *Carbon*, **186**, 380–390.
2. Yi, E., Shen, X., Chen, X., Jiang, M., Yan, W., Liu, Y., Jiang, W., & Abdullah, M. (2023). Preparation of biomass composite activated carbon based supercapacitor materials and their application in energy storage devices. *Chemical Engineering Science*, **282**, 119193.
3. Du, X., Lin, Z., Zhang, Y., & Li, P. (2023). Microstructural tailoring of porous few-layer graphene-like biochar from kitchen waste hydrolysis residue in molten carbonate medium: Structural evolution and conductive additive-free supercapacitor application. *Science of The Total Environment*, **871**, 162045.
4. Ouyang, J., Wang, X., Wang, L., Xiong, W., Li, M., Hua, Z., Zhao, L., Zhou, C., Liu, X., Chen, H., & Luo, Y. (2022). Construction of a porous carbon skeleton in wood tracheids to enhance charge

storage for high-performance supercapacitors. *Carbon*, **196**, 532–539.

5. Rustamaji, H., Prakoso, T., Devianto, H., & Widiatmoko, P. (2023). Parameter study in preparation of nitrogen-rich-activated carbon for supercapacitors' application using multilevel factorial design. *Materials Today: Proceedings*, **3**(4),163.
6. Keppetipola, N. M., Dissanayake, M., Dissanayake, P., Karunarathne, B., Dourges, M. A., Talaga, D., Servant, L., Olivier, C., Toupance, T., Uchida, S., Tennakone, K., & Cojocaru, L. (2021). Graphite-type activated carbon from coconut shell: a natural source for eco-friendly non-volatile storage devices. *RSC advances*, **11**(5), 2854–2865.
7. Pant, B., Ojha, G. P., Acharya, J., & Park, M. (2023). Preparation, characterization, and electrochemical performances of activated carbon derived from the flower of *Bauhinia variegata L.* for supercapacitor applications. *Diamond and Related Materials*, **136**, 110040.
8. Aruchamy, K., Dharmalingam, K., Lee, C. W., Mondal, D., & Kotrappanavar, N. S. (2022). Creating ultrahigh surface area functional carbon from biomass for high performance supercapacitor and facile removal of emerging pollutants. *Chemical Engineering Journal*, **427**, 131477.
9. Wu, W., Zheng, H., Zhang, Y., Wang, Q., Huang, W., Xiang, J., Yang, X., Lu, W., Zhang, Z., & Wang, S. (2023). Preparation of high performance supercapacitors with nitrogen and oxygen self-doped porous carbon derived from wintersweet-fruit-shell. *Journal of Physics and Chemistry of Solids*, **177**, 111274.
10. Gao, Y., Yue, Q., Gao, B., & Li, A. (2020). Insight into activated carbon from different kinds of chemical activating agents: A review. *Science of the Total Environment*, **746**, 141094.
11. Xu, H., Zhang, Y., Wang, L., Chen, Y., & Gao, S. (2021). Hierarchical porous biomass-derived carbon framework with ultrahigh surface area for outstanding capacitance supercapacitor. *Renewable Energy*, **179**, 1826–1835.
12. Karakehya, N. (2023). Effects of one-step and two-step KOH activation method on the properties and supercapacitor performance of highly porous activated carbons prepared from Lycopodium clavatum spores. *Diamond and Related Materials*, **135**, 109873.
13. Gao, Y., Wang, J., Huang, Y., Zhang, S., Zhang, S., & Zou, J. (2023). Rational design of N-doped porous biomass carbon nanofiber electrodes for flexible asymmetric supercapacitors with high-performance. *Applied Surface Science*, **638**, 158137.
14. Kim, M. J., Park, J. E., Kim, S., Lim, M. S., Jin, A., Kim, O. H., Kim, M.J., Lee, K.S., Kim, J., Kim, S.S. Cho, Y.H., & Sung, Y. E. (2019). Biomass-derived air cathode materials: pore-controlled S, N-Co-doped carbon for fuel cells and metal–air batteries. *ACS catalysis*, **9**(4), 3389–3398.
15. Jerez, F., Ramos, P. B., Córdoba, V. E., Ponce, M. F., Acosta, G. G., & Bavio, M. A. (2023). Yerba mate: From waste to activated carbon for supercapacitors. *Journal of Environmental Management*, **330**, 117158.

16. Feng, T., Wang, S., Hua, Y., Zhou, P., Liu, G., Ji, K., Lin, Z., Shi, S., Jiang, X., & Zhang, R. (2021). Synthesis of biomass-derived N, O-codoped hierarchical porous carbon with large surface area for high-performance supercapacitor. *Journal of Energy Storage*, **44**, 103286.
17. Ding, Y., Li, Y., Dai, Y., Han, X., Xing, B., Zhu, L., Qiu, K., & Wang, S. (2021). A novel approach for preparing in-situ nitrogen doped carbon via pyrolysis of bean pulp for supercapacitors. *Energy*, **216**, 119227.
18. Tran Thi Dieu, H., Charoensook, K., Tai, H. C., Lin, Y. T., & Li, Y. Y. (2021). Preparation of activated carbon derived from oil palm empty fruit bunches and its modification by nitrogen doping for supercapacitors. *Journal of Porous Materials*, **28**, 9–18.
19. Kong, Q., Zhang, Q., Yan, B., Chen, J., Chen, D., Jiang, L., Lan, T., Zhang, C., Yang, W., & He, S. (2024). N/O co-doped porous carbon synthesized by lewis acid salt activation for high rate performance supercapacitor. *Journal of Energy Storage*, **80**, 110322.
20. Al, K., & Kabakcı, S. B. (2024). Oxygen-rich precursors via glycerol organosolv treatment: Preparation of activated carbon from hazelnut shell and its structural components for possible use in electrodes for supercapacitors. *International Journal of Thermofluids*, **21**, 100588.
21. Boulanger, N., Talyzin, A. V., Xiong, S., Hultberg, M., & Grimm, A. (2024). High surface area activated carbon prepared from wood-based spent mushroom substrate for supercapacitors and water treatment. *Colloids and Surfaces A: Physicochemical and Engineering Aspects*, **680**, 132684.
22. Seman, R. N. A. R., & Azam, M. A. (2020). Hybrid heterostructures of graphene and molybdenum disulfide: The structural characterization and its supercapacitive performance in 6M KOH electrolyte. *Journal of Science: Advanced Materials and Devices*, **5**(4), 554–559.
23. Zhou, Y., Ren, X., Du, Y., Jiang, Y., Wan, J., & Ma, F. (2020). In-situ template cooperated with urea to construct pectin-derived hierarchical porous carbon with optimized pore structure for supercapacitor. *Electrochimica Acta*, **355**, 136801.
24. Bhushan M. (2023). Various characterization techniques for nanomaterials. *Energy Applications*, **11**(2), 103–114.
25. Xue, B., Xu, J., & Xiao, R. (2023). Ice template-assisting activation strategy to prepare biomass-derived porous carbon cages for high-performance Zn-ion hybrid supercapacitors. *Chemical Engineering Journal*, **454**, 140192.
26. Yang, X., Wang, Q., Lai, J., Cai, Z., Lv, J., Chen, X., Chen, Y., Zheng, X., Huang, B., & Lin, G. (2020). Nitrogen-doped activated carbons via melamine-assisted NaOH/KOH/urea aqueous system for high performance supercapacitors. *Materials Chemistry and Physics*, **250**, 123201.
27. Ma, M., Zhang, J., Huan, Y., Ren, M., Wei, T., & Yan, S. (2023). 3D stack tubular mesoporous carbon derived from discarded sesame capsule shells for high-

performance supercapacitors. *Diamond and Related Materials*, *131*, 109562.

28. Xie, M., Meng, H., Chen, J., Zhang, Y., Du, C., Wan, L., & Chen, Y. (2021). High-volumetric supercapacitor performance of ordered mesoporous carbon electrodes enabled by the faradaic-active nitrogen doping and decrease of microporosity. *ACS Applied Energy Materials*, **4**(2), 1840–1850.
29. Zhang, G., Zhu, R., Zhang, R., Sun, C., & Long, Z. (2023). A novel strategy for large-scale preparation of flexible high-conductivity carbon fiber paper for supercapacitors. *Diamond and Related Materials*, **138**, 110229.

IPC
Indonesian Physics Communication
Department of Physics, Universitas Riau, Pekanbaru, Indonesia
p-ISSN 1412-2960 | e-ISSN 2579-521X
Vol. 21 | No. 3
November 2024
Web: https://kfi.ejournal.unri.ac.id
E-mail: kfi@ejournal.unri.ac.id

Prediction of Pekanbaru City rainfall using dynamic models

Esy Yunita*, Sri Fitria Retnawaty, Neneng Fitrya
Department of Physics, Universitas Muhammadiyah Riau, Pekanbaru 28294, Indonesia

*Corresponding author: esy1706@gmail.com

ABSTRACT

The need for predictions is very necessary in various sectors of life, one of which is rainfall predictions. The threshold value for PM_{10} particles that is allowed to be in ambient air is, 150 µgram/m^3/day). The aim of this research is to create a dynamic model predicting Pekanbaru City's rainfall for the next 3 years. Rainfall prediction in this research was carried out using the dynamic system modeling method with Powersim software. The data used is BMKG data for the Pekanbaru City for 5 years (2015 – 2019) using 4 parameters, namely rainfall, air humidity, wind speed and temperature. Prediction results show that air humidity in Pekanbaru City has the same pattern as BMKG, namely the highest month is December and the lowest is August. Wind speed prediction results are highest in July and lowest in May. The highest temperature in Pekanbaru City is in April and the lowest is in January. Rainfall for 2020 – 2021 is predicted to experience light rain on average, because it has the same data pattern on the variables that influence it. So it can be interpreted that the validation results for air humidity, wind speed and temperature in Pekanbaru City show that they are valid because they do not exceed the limit value of $\leq 5\%$.

Keywords: Dynamic model; Pekanbaru City; prediction; rainfall

Received 26-09-2023 | Revised 19-10-2023 | Accepted 06-11-2024 | Published 30-11-2024

INTRODUCTION

Particulates (PM_{10}) are airborne particles that are smaller than 10 microns (micrometers). The threshold value of PM_{10} particles allowed in ambient air is 150 µgram/m^3/day [1]. Specifically in Pekanbaru City in 2019 in July the PM_{10} value was still below the NAB, which was around 48.89 µgram/m^3/day. In August the PM_{10} value was 80.44 µgram/m^3 and the September PM_{10} value exceeded the quality standard threshold value with a very unhealthy category, namely with a value of 245.94 µgram/m^3 [2].

The increase in PM_{10} values is caused by forest and land fires in the area around Pekanbaru City, as well as the dry season which also worsens air quality due to the absence of rain to reduce the deposition of air pollutants [2-4]. Rainfall can remove pollutants in the atmosphere, pollutants will be directly washed by rainwater and then deposited on the surface [5-9]. Rainfall data for the last 5 years obtained from BMKG shows that September was a dry month. The amount of rainfall in September amounted to 28 mm, while the previous 2 months, July and August experienced moderate rainfall months with rainfall amounts of 119.2 and 148.7. There has been a lot of research on rainfall, one of the studies that predict rainfall was conducted by Oktaviani and Afdal (2013) in Padang City [10]. This research is to recognize rainfall patterns using traingdx. The results obtained are in the form of rainfall prediction results for the next 3 years but this research uses complex equations that require a lot of time and computers with high specifications. In 2015, Handayani and Adri, predicted rainfall in Pekanbaru City using the trainlm training function with two variations, namely binary activation function and bipolar activation function [11]. The results obtained from this research are in the form of rainfall prediction results for the next 3 years, but this research uses complex equations that require a lot of time and high specifications computers.

Based on the description above, the prediction of rainfall in Pekanbaru City will be carried out with a dynamic model using powersim. The data that will be used for rainfall prediction are temperature data, air humidity and wind speed. This research is expected to predict the monthly rainfall of Pekanbaru City for the next 3 years with simpler equations and methods.

MATERIALS AND METHODS

Collecting Data

The data used in this research is data for the last 5 years, from 2015 to 2019, totaling 240 data from 4 parametres (temperature, humidity, wind speed, and rainfall). The data was obtained from the BMKG Pekanbaru City online data website (http://dataonline.bmkg.go.id/). The data were processed and entered into monthly data in the last 5 years and the data were obtained [12-14].

Identification of System Variables

The variables used are temperature, humidity, wind speed and rainfall. The relationship between variables in the causal loop diagram of rainfall prediction in this study can be seen in Table 1 and rainfall prediction variables can be seen in Table 2.

Table 1. Relationship between variables with causal loop of rainfall prediction in Pekanbaru City.

Diagram	Variable	Connection
Rainfall	Temperature	+
	Wind velocity	–
	Air humidity	+

Table 2. Rainfall prediction variables of Pekanbaru City in 2015 – 2019.

Variable	Influencing variables	Infornation	Data source
Rainfall	Tenperature	Constant comes from BMKG	Secondary data was obtained from BMKG Pekanbaru City
	Wind velocity		
	Air humidity		

Dynamic Model Building

Dynamic modeling is the creation of a causal loop diagram (CLD) and the creation of a stock flow diagram (SFD). Making causal loop diagrams is done by determining the factors that affect system performance. Making stock and flow diagrams is done by determining the variables affected by rainfall in Pekanbaru City against the variables that influence (temperature, humidity, and wind speed).

Dynamic Model Simulation

Simulation of dynamic model of rainfall, temperature, humidity, and wind speed of Pekanbaru City for 2015 – 2019 using powersim software tool.

Verification and Validation

Verification and validation in this research uses data in 2020 by comparing the results of rainfall simulations for the Pekanbaru City. Pekanbaru. The comparison result must be ≤ 5%, if it exceeds ≤ 5% then the causal loop diagram will be made again.

Data

Data analysis by analyzing graphs generated from Powersim Software modeling simulations. Predict rainfall for the next 3 years using Powersim by analyzing the graph result.

RESULTS AND DISCUSSION

Collecting Data

Rainfall Rate

The pattern of rainfall data that has been taken shows a seasonal cycle where in 5 years (2015 – 2019) has the same pattern. The average graph of the 5-year rainfall data of Pekanbaru City can be seen in Figure 1.

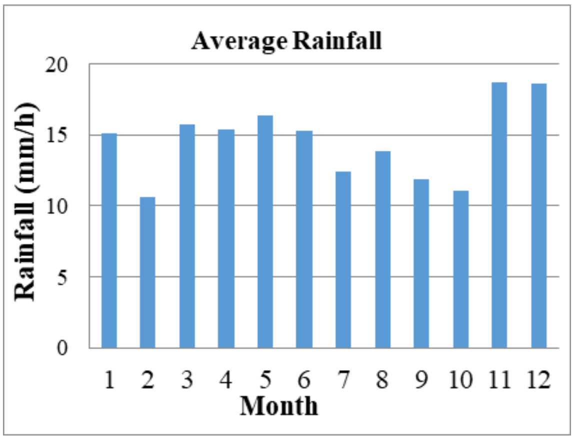

Figure 1. Graph of average rainfall monthly rainfall of Pekanbaru City in 5 years (2015 – 2019).

Air Humidity

The air humidity of Pekanbaru City shows a seasonal cycle with the highest humidity in November, and the lowest in October. The average graph of the 5-year data of air humidity of Pekanbaru City can be seen in Figure 2.

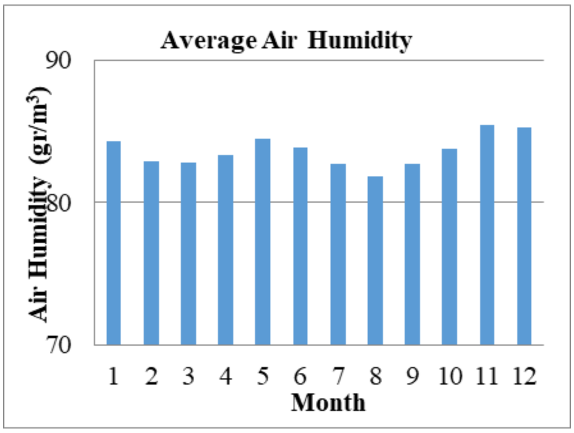

Figure 2. Graph of average monthly air humidity of Pekanbaru City in 5 years (2015 – 2019).

Temperature

The temperature of Pekanbaru City shows a seasonal cycle with the highest temperature in September, and the lowest in January. The temperature number is one of the positive variables which means, the more the temperature number increases, the more the amount of rainfall increases. The average graph of 5 years of Pekanbaru City temperature data can be seen in Figure 3.

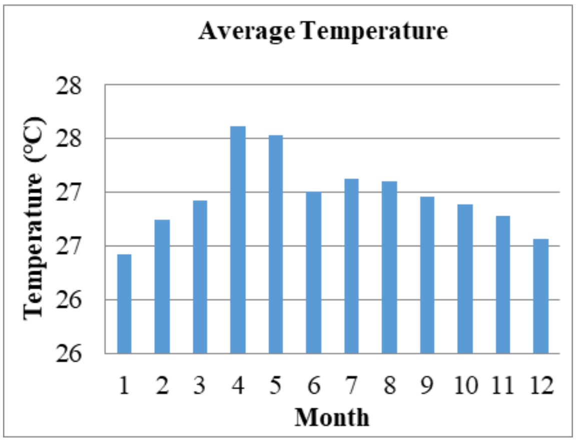

Figure 3. Graph of average monthly temperature Pekanbaru City in 5 years (2015 – 2019).

Wind Velocity

Wind speed is one of the factors that affect rainfall in Pekanbaru City. The temperature of Pekanbaru City shows a seasonal cycle with the highest humidity in September, and the lowest in January. The average graph of 5 years wind speed data of Pekanbaru City can be seen in Figure 4.

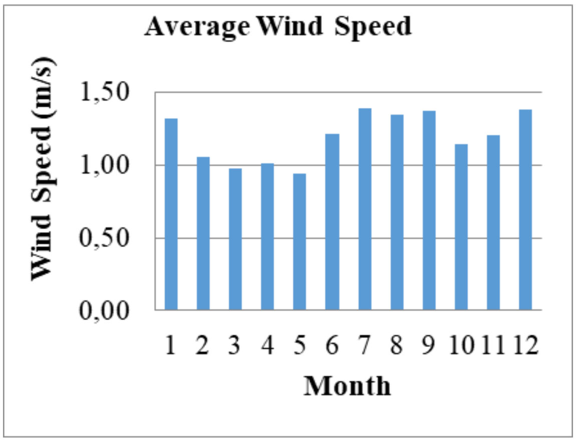

Figure 4. Graph of average monthly wind speed of Pekanbaru City in 5 years (2015 – 2019).

The temperature in November was 26.75ºC with a wind speed of 1.20 m/s which is low compared to other months. The highest temperature occurred in May which was 27.53ºC with the lowest wind speed of 0.94 m/s, rainfall at the time of the highest temperature was 16.36 mm with air humidity of 84.75 gram/m^3. The highest wind speed occurred in July which was 1.39 m/s with rainfall of 12.42 mm, air humidity at the time of the highest temperature was 83.25 gram/m^3 and the temperature in July was 27.12ºC.

The lowest rainfall and temperature occurred in January, with rainfall of 10.13 mm and temperature of 26.42ºC. The air humidity at the time of the lowest temperature and rainfall was 84.34 gram/m^3 and the wind speed was 1.31 m/s. The lowest air humidity occurred in August which was 80.05 gram/m^3, with a wind speed of 1.35 m/s. The temperature in August was 27.10ºC and the rainfall was 13.82 mm. The average data air humidity, wind speed and temperature with rainfall for 5 years (2015 – 2019), from January to December shows the state of light rainfall, which is between 5 – 20 mm.

Results of Causal Loop Diagram of Rainfall Prediction

Causal loop diagram is made to connect variables that affect the addition and subtraction of the system model that will be used to predict the amount of rainfall in Pekanbaru City as shown in Figure 5.

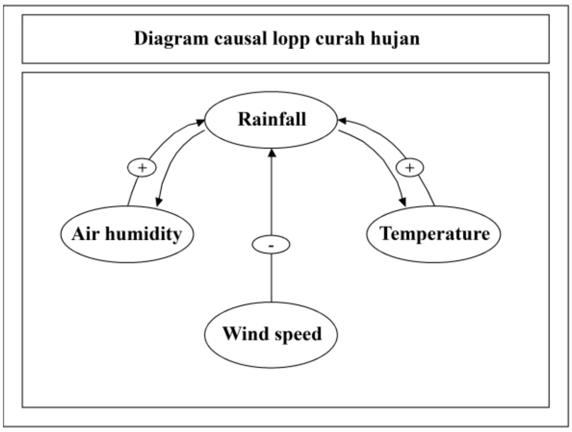

Figure 5. Causal loop diagram for rainfall prediction ini Pekanbaru City.

Factors affecting rainfall in Pekanbaru City are temperature and humidity, which are connected by a positive line, meaning that the more the temperature and humidity numbers increase, the rainfall in Pekanbaru City will also increase. Another variable that affects rainfall is wind speed which is connected with a negative line, meaning that the more the wind speed number increases, the less rainfall. The discussion above shows that the causal loop diagram is feedback information [15].

The change in air humidity in January 0.0037 is obtained from the average of the results of the change in air humidity data in 2016, 85.55 gram/m^3. 2016 85.55 gram/m^3 minus 2015 data 83.94 gram/m^3, 2017 84.50 gram/m^3 minus 2016 85.55 gram/m^3, 2018 82.60 gram/m^3 minus 2017 84.50 gram/m^3, and 2019 85.11 gram/m^3 minus 2018 82.60 gram/m^3. Changes in wind speed data and temperature data are obtained in the same way as the change data humidity.

Result of Stock Diagram Creation

Stock flow diagram is made to simulate air humidity, wind speed and temperature. Stock flow diagrams produce predictions of air humidity, wind speed and temperature which will be used to predict rainfall in Pekanbaru City for the next 2 years.

Results of Making Air Humidity Stock Flow Diagram

The stock flow diagram on the constant symbol will include the percentage of the 5-year air humidity (2015 – 2019) and on the level symbol will include the average results of the air humidity of the last 5 years (2015 – 2019). Stock flow diagram of air humidity of Pekanbaru City can be seen in Figure 6.

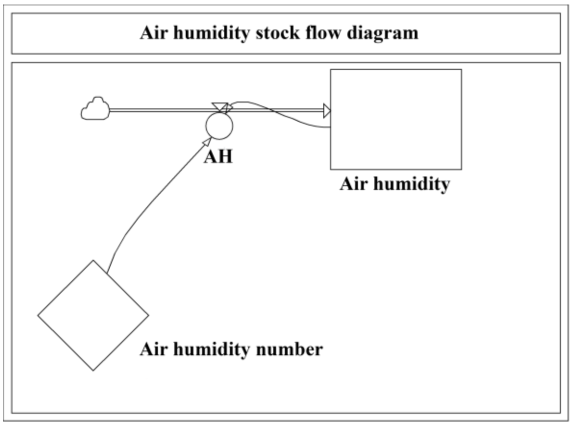

Figure 6. Stock flow diagram for air humidity prediction.

Results of Stock Flow Diagram Creation Temperature

The stock flow diagram on the constant symbol will include the percentage of the 5-year temperature (2015 – 2019) and on the level symbol will include the average results of the last 5 years of air humidity (2015 – 2019). Stock flow diagram of air humidity of Pekanbaru City can be seen in Figure 7.

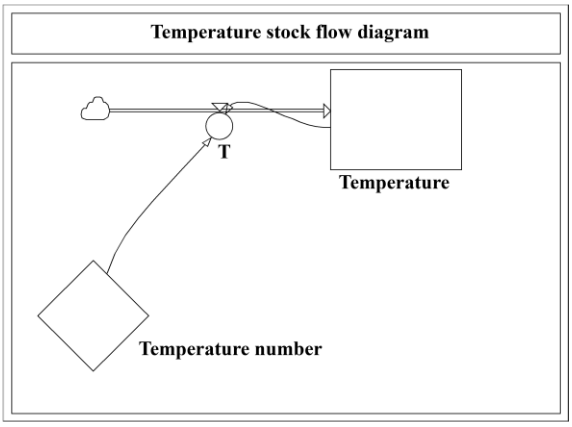

Figure 7. Stock flow diagram of temperature prediction for Pekanbaru City.

Results of Stock Flow Diagram Creation Wind Speed

The stock flow diagram on the constant symbol will include the percentage of wind speed for 5 years (2015 – 2019) and on the level symbol will include the average results of air humidity for the last 5 years (2015 – 2019). Stock flow diagram of wind speed of Pekanbaru City can be seen in Figure 8.

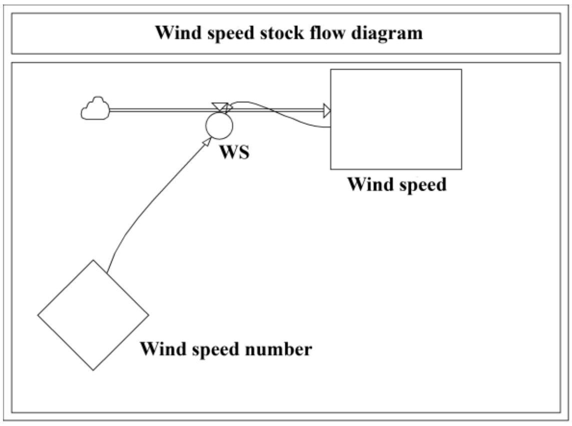

Figure 8. Stock flow diagram for predicting wind speed for Pekanbaru City.

Validation Results

Data validation results that show the percentage error does not exceed the limit ≤ 5% of the average value allowed then the prediction model made can be used. Validation of air humidity, wind Speed, and temperature of Pekanbaru City is done by comparing real data of air humidity, wind speed and temperature sourced from BMKG Pekanbaru City with simulated data [16].

Air Humidity Validation Results

Air humidity validation results when the highest simulation results are highest, namely, in July 86.69 gram/m^3 and real BMKG data from the average of the last 5 years (2015 – 2019) 82.72 gram/m^3 with an error rate of 0.0480. Air Humidity validation results when the lowest simulation results are in August 81.1 gram/m^3 and real data from BMKG from the average of the last 5 years is 81.85 gram/m^3 with an error rate of -0.0092.

Validation is made by calculating the difference between BMKG real data and simulated data, and calculating the percentage of BMKG real data. The percentage difference between the highest and lowest simulation results shows an error rate of less than ≤ 5%.

Temperature Validation Results

Temperature validation results when the highest simulation results are in July 27.07ºC, and real BMKG data from the average of the last 5 years is -0.0018. Temperature validation results at the time of the lowest simulation results in January 26.41ºC, and BMKG real data from the average of the last 5 years (2015 – 2019) is 26.42ºC with an error rate of -0.0004. Validation is made by calculating the difference between BMKG real data and simulated data, and calculating the percentage of BMKG real data. The highest and lowest simulation results show an error rate of less than ≤ 5%.

Wind Speed Validation Results

Wind speed validation results when the highest simulation results are in July 1.38 m/s and real BMKG data from the average of the last 5 years (2015 – 2019) 1.39 m/s, with an error rate of -0.01. Wind speed validation results when the lowest simulation results are in March 0.9 m/s and real BMKG data from the average of the last 5 years is 0.97 m/s with an error rate of -0.7. Validation is made by calculating the difference between BMKG real data and simulated data, and calculating the percentage of BMKG real data. The percentage difference between the highest and lowest simulation results shows an error rate of less than ≤ 5%.

The results of validation of air humidity, temperature and wind speed are in line with the results of research conducted by Nursanti in 2017, which does not exceed the ≤ 5% limit.

Prediction Results

Prediction results can be used after the simulated data is validated by comparing with real data, Air humidity wind speed and temperature have been declared valid. The percentage value of the validation error of air humidity, wind speed and temperature is within the limits of the average value allowed which is ≤ 5% [17].

Air Humidity Prediction Results

The results of the prediction of air humidity in Pekanbaru City are obtained from entering the percentage of air humidity into the stock flow diagram which can be seen in Figure 6. The highest air humidity prediction results occur in December, namely in 2020 85.46 gram/m^3, while 2021 85.48 gram/m^3 and 2022 is 85.51 gram/m3. The lowest air humidity prediction results occurred in August in 2020 81.97 gram/m^3, while in 2021 82 gram/m^3 and in 2022 82.02 gram/m^3. The predicted air humidity results have the same pattern as the BMKG real average data, which shows that the highest air humidity figure occurs in December and the lowest occurs in August.

Temperature Prediction Results

The results of the Pekanbaru City temperature prediction are obtained from entering the percentage of wind speed into the Pekanbaru City temperature stock flow diagram which can be seen in Figure 7. The highest temperature prediction results occur in April, the predicted temperature for 2020 – 2021 in that month is 27.65ºC while in 2022 it is 27.66ºC. The lowest temperature prediction results occur in January, the predicted temperature in 2020 is 26.45ºC while in 2021 and 2022 it is 26.46ºC. in that month it is 26.43ºC.

Wind Speed Prediction Results

The results of the prediction of wind speed in Pekanbaru City are obtained from entering the percentage of wind speed into the stock flow diagram which can be seen in Figure 8. The highest wind speed prediction results occur in July, the predicted wind speed for 2020 – 2022 in that month is 1.41 m/s. The lowest wind speed prediction results occurred in May, in 2020 it was 0.97 m/s while in 2021 and 2022 it was 0.98 m/s.

The BMKG real average data for the last 5 years (2015 – 2019) and the simulation results do not change too much every month, but still have differences every month with the same pattern every year. Air humidity, wind speed and temperature in the BMKG real average data for the last 5 years (2015 – 2019) show that the average rainfall is in a light rainy condition because the BMKG real average rainfall data for the last 5 years (2015 – 2019) ranges from 5 – 20 mm. Rainfall 2020-2021 is predicted to experience light rain on average, this prediction is in line with research conducted [18] which predicts based on seeing the same data patterns in the variables that influence it.

CONCLUSION

The validation results of air humidity, temperature and wind speed do not exceed the limit of ≤ 5% of the average value allowed. The validation results on simulated data with real BMKG data are declared valid because they do not exceed the predetermined limit of ≤ 5%. Rainfall in 2020 – 2021 is predicted to experience light rain on average.

REFERENCES

1. PERMENLH. (2021). Nilai ambang batas partikulat. *Peraturan Menteri Negara Lingkungan Hidup No. 12*.
2. BMKG. (2019). *Informasi jumlah nilai PM10 Kota Pekanbaru*. Badan Meteorologi, Klimatologi dan Geofisika.
3. Anggriyani, S., Manuputty, M., Lewaherilla, A., & Bakarbessy, L. (2024). Prediksi curah hujan di Kota Tual dengan menggunakan metode backpropagation. *PARAMETER: Jurnal Matematika, Statistika dan Terapannya*, **3**(1), 1–11.
4. Istianto, A. F., Hadiana, A. I., & Umbara, F. R. (2023). Prediksi curah hujan menggunakan metode categorical boosting (Catboost). *JATI (Jurnal Mahasiswa Teknik Informatika)*, **7**(4), 2930–2937.
5. El-Sawah, S., Haase, D., Van Delden, H., Pierce, S., ElMahdi, A., Voinov, A., & Jakeman, A. J. (2012). Using system dynamics for environmental modelling: Lessons learnt from six case studies. *6th International Congress on Environmental Modelling and Software 2012: Managing Resources of a Limited Planet: Pathways and Visions under Uncertainty*, 1367–1374.
6. Safril, A. & Ulfiana, A. (2019). Prediksi curah hujan bulanan menggunakan metode statistical downscaling di pulau jawa dengan pemilihan prediktor berdasarkan transpor uap air. *Jurnal Geografi*, **11**(2), 19–33.
7. Setiyaris, S. (2023). *Prediksi curah hujan berdasarkan parameter cuaca berbasis jaringan saraf tiruan di Kabupaten Nganjuk*. Doctoral dissertation, Universitas Islam Negeri Maulana Malik Ibrahim.
8. Sarwoko, D. (2013). *Pemodelan prediksi total hujan pada musim hujan menggunakan jaringan saraf tiruan dan support vector regression*. Sekolah Pasca Sarjana Institut Pertanian Bogor, Bogor.
9. BMKG. (2013). *Analisis Musim Kemarau 2013 Dan Prakiraan Musim Hujan 2013*. Badan Meteorologi Klimatologi dan Geofisika, Kelas II, and Pondok Betung Betung.
10. Oktaviani, C. & Afdal, A. (2013). Prediksi curah hujan bulanan menggunakan jaringan syaraf tiruan dengan beberapa fungsi pelatihan backpropagation (studi kasus: stasiun meteorologi tabing padang, tahun 2001-2012). *Jurnal Fisika Unand*, **2**(4).
11. Handayani, L. & Adri, M. (2015). Pwenerapan JST (backpropagation) untuk prediksi curah hujan (Studi kasus: Kota Pekanbaru). *Seminar Nasional Teknologi Informasi Komunikasi dan Industri*.
12. BMKG. (2019). *Informasi jumlah nilai PM10 Kota Pekanbaru*. Badan Meteorologi, Klimatologi dan Geofisika.
13. BMKG. (2019). *Kualitas udara Kota Pekanbaru*. Badan Meteorologi, Klimatologi dan Geofisika.
14. BMKG. (2019). *Informasi sebaran titik panas sekitar kota Pekanbaru*. Badan Meteorologi, Klimatologi dan Geofisika.
15. Ni’maturrakhmat. (2019). *Penjadwalan produksi venner di PT. XYZ dengan pendekatan sistem dinamis*. Skripsi

Fakultas Teknologi Pertanian. Universitas Jember.

16. Muljono, A. B., Mukti, K. B. K., & Natsir, A. (2022). Kajian teknis dan ekonomi pembangkit listrik tenaga sampah (PLTSa) menggunakan perangkat lunak LandGEM TPA Kebon Kongok Gerung Lombok Barat. *DIELEKTRIKA*, **9**(1), 68–79.
17. Robby, T. N., Ramdhani, M., & Ekaputri, C. (2017). Alat ukur kecepatan angin, arah angin, dan ketinggian. *eProceedings of Engineering*, **4**(2).
18. Kustiyo, A., Sucahyono, D., & Mujahidin, A. (2015). Penerapan jaringan saraf tiruan untuk pemodelan prakiraan curah hujan bulanan. *IPB Scientific Repository*.

IPC
Indonesian Physics Communication
Department of Physics, Universitas Riau, Pekanbaru, Indonesia
p-ISSN 1412-2960 | e-ISSN 2579-521X
Vol. 21 | No. 3
November 2024
Web: https://kfi.ejournal.unri.ac.id
E-mail: kfi@ejournal.unri.ac.id

Study of the structural, optical, and morphological properties of ZnO nanoparticle biosynthesis using betel leaf extract as a bioreductant

Yanuar Hamzah*, Nursiti Sari Kartika, Lazurdi Umar
Department of Physics, Universitas Riau, Pekanbaru 28293, Indonesia

*Corresponding author: yanuar.hamzah@lecturer.unri.ac.id

ABSTRACT

The biosynthesis of zinc oxide nanoparticles (ZnO) is extensively studied because of its eco-friendly and simple method. Piper ornatum is abundant in Indonesia, and the phytochemical content of Piper ornatum leaves has the potential to be a reductor. The study aims to study the role of Piper ornatum in biosynthesis and the characteristics of the zinc oxide nanoparticles. The sample variations in this study were the volume of Piper ornatum and the precursor solution of zinc nitrate hexahydrate $Zn(NO_3)_2{\cdot}6H_2O$ in proportions of 1:1, 1:5, and 1:10. Characterizations performed include UV-Vis spectroscopy, X-ray diffraction (XRD), scanning electron microscopy, energy dispersive X-ray spectroscope and blue methylene degradation test. UV-Vis spectroscopy of all samples showed peak absorption at the interval of 250 – 330 nm, which indicates that ZnO nanoparticles have already formed. The results of characterization using XRD indicated the degree of crystallinity of the ZnO nanoparticles is not perfect because the crystal field (100) or the highest diffraction peak has a very large full width at half maximum value of 0.8187°. Characterization results using SEM indicate an inhomogeneous morphology and the presence of zinc oxide nanoparticle agglomeration where particle size distribution is at an interval of 170 – 758 nm.

Keywords: Bioreductor; biosynthesis; nanoparticle; *Piper ornatum*; ZnO

Received 29-09-2023 | Revised 22-10-2023 | Accepted 09-11-2024 | Published 30-11-2024

INTRODUCTION

Nanotechnology is a recent modern research field that deals with the synthesis, strategy, and manipulation of particle structures in the size range of 1 – 100 nm. This study introduces one of the methods of nanoparticle synthesis, namely the green synthesis of ZnO NPs using *Becium grandiflorum* leaf aqueous extract. The synthesized ZnO NPs were used to remove MB dye from aqueous solutions [1]. ZnO nanoparticles synthesized using plant extracts and their derivatives are more stable compared to the use of other organisms. This is because the content in plant extracts acts as a reducing agent and stabilizer as well as a capping agent in the biosynthesis of ZnO nanoparticles [2]. Research on the synthesis of $Ag/CoFe_2O_4$ nanoparticles using binahong leaf extract has a degradation percentage value of 44.84% with a contact time of 120 minutes [3]. Another study is on the biosynthesis of zinc oxide nanoparticles with *Suaeda japonica* extract. This study succeeded in reducing methylene blue by 54% [4]. Red betel is a plant that is widely used because of its various uses. Red betel contains several compounds, namely phytochemicals from the alkaloid, flavonoid, and tannin groups which are effective as antihyperglycemic and antioxidants [5]. The tannin compound contained in betel leaves is a phenolic compound which is a polymerization of simple polyphenols. The flavonoid and phenolic content obtained from red betel leaf extract is a surface active molecule that can reduce metals in the formation of nanoparticles [6]. Red betel (*Piper crocatum*) is one of the potential medicinal plants that is empirically known to have properties to cure various types of diseases, in addition to also having high spiritual value. This plant is included in the Piperaceae family with the appearance of leaves that are silvery red and shiny when exposed to light.

©Author(s) | DOI: 10.31258/jkfi.21.3.227-232

In 1990, red betel was used as an ornamental plant by hobbyists, because of its attractive appearance. The surface of the leaves is silvery red and shiny (the red betel plant can be seen in Figure 1). In recent years, it has been widely discussed and used as a medicinal plant. From several experiences, it is known that red betel has medicinal properties for several diseases [2].

Figure 1. Red betel plant.

The use of red betel leaves is currently widely used as herbal medicine. Investigations into the benefits contained in red betel leaves are mentioned because several phytochemicals such as phenolics, essential oils, flavonoids, and terpenes provide positive bioactivity effects. These compounds are equipped with functional groups designed to have properties such as inhibiting oxidation in free fatty acids, facing free radical activity or inhibiting the growth of unwanted cells. Therefore, these bioactive compounds have some potential as antioxidants, antiseptics, antimicrobial activity, and antihyperglycemia. In addition, leaf extracts are also indicated to have anticancer activity against human breast cancer cells [7].

Zinc oxide is an inorganic compound with the molecular formula ZnO. This compound is in the form of a white powder and is almost insoluble in water. ZnO powder is widely used as an additive in various materials and products of ointments, adhesives, plastics, sealants, pigments, food (source of Zn nutrition), batteries, ferrites, and flame retardants [3]. Zinc oxide (ZnO) has a band gap width of 3.37 eV at room temperature (RT) and an exciton energy of 60 meV. ZnO has excellent chemical stability because its hexagonal wurtzite structure at normal temperatures causes large Coulomb forces for its positive and negative electron pairs [8]. This study aims to study the structural, optical and morphological properties of ZnO nanoparticle biosynthesis using red betel leaf extract.

MATERIALS AND METHODS

Preparation of Red Betel Leaf Extract

The plants used are fresh leaves. The leaves that have been taken are washed until clean then rinsed using deionized water then the leaves are cut into pieces to facilitate the drying process. The drying process is carried out under sunlight until the red betel leaves are dry. Once dry, the leaves are ground using a blender and sieved. A total of 10 grams of red betel leaf powder is added with 100 ml of deionized water. After that, it is heated on a hot plate for 30 minutes at a temperature of 90ºC while stirring using a magnetic stirrer. Allow the solution to cool, until it reaches room temperature. Furthermore, the boiled water is filtered using Whatman paper no. 1 until the filtrate is obtained as a red betel leaf polyphenol extract. This filtrate will be used as a bioreductor in the ZnO nanoparticle synthesis process.

Preparation of Precursor Solution

Preparation of ZnO precursor solution with a concentration of 0.1 M was carried out by dissolving 2.97 grams of $Zn(NO_3)_2{\cdot}6H_2O$ crystals. The dissolution process was carried out in an Erlenmeyer flask by adding 100 ml of distilled water. Then, the solution was stirred until it was completely mixed evenly.

Synthesis of ZnO Nanoparticles

The synthesis of nanoparticles was carried out using the biosynthesis method by reacting red betel leaf extract with a previously prepared zinc oxide solution. The red betel leaf extract here acts as a bioreductor. Then drip NaOH solution until it reaches pH 7. The addition of NaOH plays a role in regulating the acidity of the solution. Synthesis of ZnO nanoparticles was carried out by comparing the volume of red betel leaf extract with 0.1 M $Zn(NO_3)_2{\cdot}6H_2O$ solution, namely 1:1, 1:5, and 1:10. The solution was continuously stirred until it was homogeneously mixed using a magnetic stirrer. Then, the solution was heated on a hot plate at 90ºC. The solution was sonicated until it turned brownish black and a precipitate appeared. The precipitate was centrifuged and washed several times with distilled water and absolute ethanol before being dried and heated at 150ºC for 30 minutes to obtain a brownish black powder of ZnO nanoparticles ready to be characterized for structural, optical and morphological properties using XRD, UV-Vis, and SEM.

RESULTS AND DISCUSSION

The synthesis process has been carried out by varying the volume of red betel leaf extract with $Zn(NO_3)_2{\cdot}6H_2O$ precursor with a ratio of 1:1, 1:5 and 1:10 to produce nanoparticles. There is a change in the color of the red betel leaf extract to pitch black at the beginning of the synthesis process as shown in Figure 2.

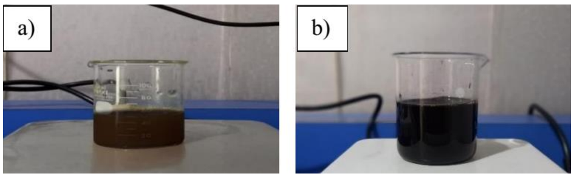

Figure 2. Color change when: (a) before adding NaOH and (b) after adding NaOH.

The color change that occurs during the synthesis process indicates that there is a reaction due to the addition of $Zn(NO_3)_2{\cdot}6H_2O$ and NaOH solutions. The synthesis begins with the formation of $Zn(OH)_2$ which is indicated by the production of a transparent cloudy black solution in the reaction. When Zn^{2+} and OH^- have reached the critical solubility number, a colloid will be produced which is indicated by a change in the color of the solution to pitch black. Zinc cations will then react with hydroxide anions and form a stable $Zn(OH)_4^{2-}$ complex. The presence of H_2O and energy from continuous stirring using a magnetic stirrer, the $Zn(OH)_4^{2-}$ complex can dissociate to form Zn^{2+} and OH- ions which will then form ZnO nanoparticles [2].

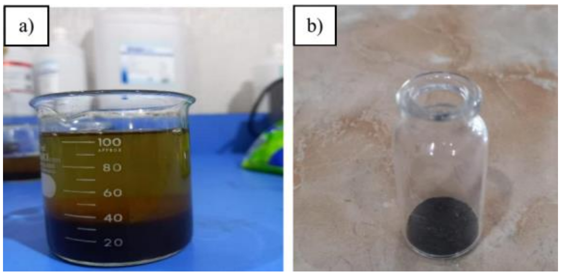

Figure 3. Sample synthesis results: (a) after 1 hour of stirring and (b) powder after drying in the oven.

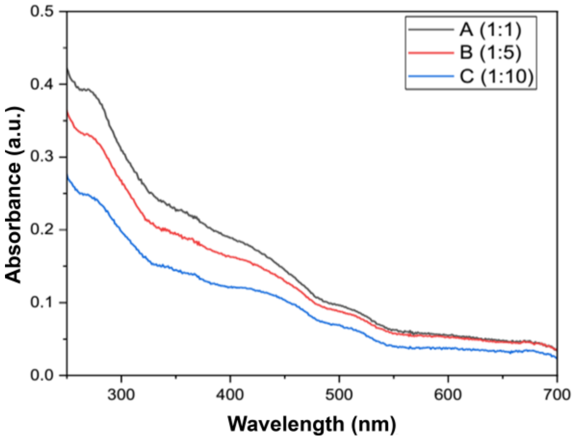

Figure 4. Graph between absorbance and wavelength in sample A (1:1), sample B (1:5) and sample C (1:10).

Continuous stirring using a magnetic stirrer produces a precipitate as shown in Figure 3. The precipitate formed is then dried using an oven for 1 hour at a temperature of 150º to produce powder. In the drying process, this precipitate will cause a dehydration reaction, namely the release of hydrate molecules which are released into the environment in the form of water vapor [9]. The UV-Vis spectrum curve of the ZnO sample with variations in extract and precursor volumes can be seen in Figure 4 showing that this UV-Vis test aims to determine the presence of nanoparticles formed. Analysis of the UV-Vis spectrophotometer test results on samples A (1:1), B (1:5) and C (1:10) with a wavelength range of 250 – 700 nm showed differences in absorbance values. The difference in absorbance and wavelength values indicates the influence of the ratio of the volume of red betel leaf extract to the $Zn(NO_3)_2$ precursor.

Based on the UV-Vis absorbance spectrum curve in Figure 4, the peak absorbance or light absorption of the ZnO sample is in the wavelength range of 250 – 330 nm which indicates that nanoparticles have been formed. These results are in accordance with other studies that recorded the UV-Vis spectrum of ZnO NPs, namely between 250 nm and 300 nm [9]. In another study, the synthesized ZnO NPs showed absorption bands ranging from 308 nm to 330 nm with a maximum peak appearing at 317 nm [10]. Sample A ZnO with a ratio of 1:1 is the sample with the highest absorbance value due to the higher volume of plant extract and sample C with a ratio of 1:10 has the lowest absorbance value. The absorbance values in samples A (1:1), sample B (1:5) and sample C (1:10) were 0.39; 0.33; and 0.24 a.u. Absorbance is directly related to the number of nanoparticles formed. The UV-Vis results show that the absorbance value increases with increasing extract volume. If the absorbance value is higher, the more nanoparticles are formed [11]. Sample A (1:1) was chosen for XRD and SEM characterization because it has the best absorbance intensity. UV-Vis spectrum data is used not only to find out about the absorbance value of the ZnO nanoparticle sample but can also be used to determine the energy gap of the sample. Tauch theory is used to determine the energy gap (E_g) value of sample absorption.

The band gap energy is obtained by transforming the absorbance graph as a function of Wavelength into a graph $(\alpha h v)^2$ as a function of the gap energy using the equation $(\alpha h v)^2 = B(hv - E_g)$, then the gap energy is determined by the extrapolation technique, namely drawing a straight line that intersects the x-axis (energy). The linear transformation graph $(\alpha h v)^2$ with energy (eV) of the ZnO sample with a ratio of 1:1 (sample A) has an energy gap of 3.54 eV (see Figure 5). The energy gap results of this study are not much different from the synthesis of ZnO nanoparticles through the wet chemical method with an energy gap value of 3.63 eV [12]. The X-ray diffraction spectrum of the 1:1 sample can be seen in Figure 6 which shows the peak crystallinity of ZnO nanoparticles that were successfully synthesized using red betel leaf extract. The diffraction pattern peaks are located at 4 2θ angles, namely 33.49º, 59.54º, 63.4º, and 70.15º. The resulting Miller indices are (100), (103), (200), and (201). These diffraction peaks correspond to the hexagonal wurtzite structure based on the Joint Committee in Powder Diffraction Standard (JCPDS) No. 36-1451 [13].

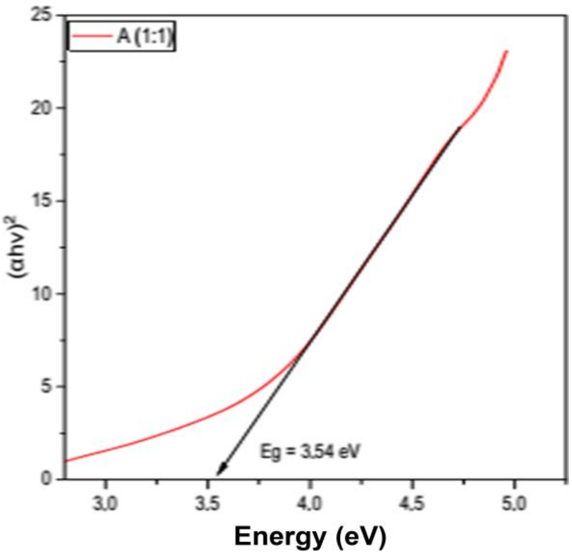

Figure 5. Energy gap graph of ZnO nanoparticles in sample A (1:1).

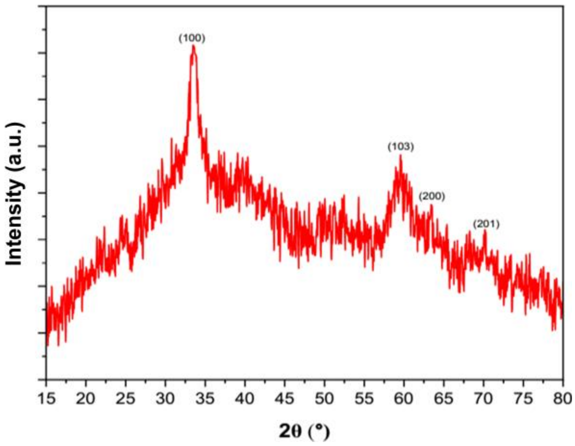

Figure 6. XRD pattern of ZnO nanoparticles in sample A (1:1).

The highest and sharpest diffraction peak based on the XRD pattern as shown in Figure 6 is at position 2θ = 33.49°. Where the diffraction peak is the same as the study on the synthesis of ZnO nanoparticles using trisodium citrate precursors with the Miller index (100) [14].

Scanning electron microscope (SEM) characterization aims to show or demonstrate the surface morphology of ZnO samples synthesized using zinc nitrate hexahydrate precursor solution and red betel leaf extract solution with the best sample ratio in the UV-Vis test, namely a 1:1 sample. SEM results provide information on size and shape based on the surface image of the ZnO sample. Figure 4.6 shows the SEM results with a magnification of 10,000 times and particle size distribution.

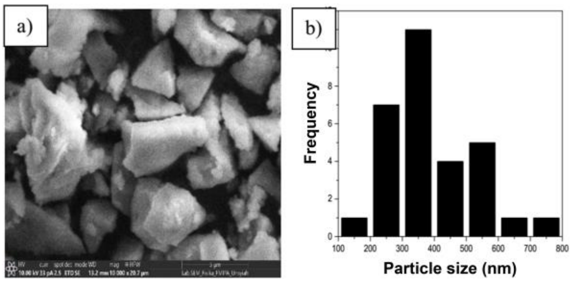

Figure 7. Morphology of ZnO nanoparticle size with (a) 10000x magnification and (b) graph of the results of measuring the diameter of ZnO sample particles.

Based on the SEM results seen in Figure 7 (a) shows the agglomeration (accumulation or collection of nanoparticles) of zinc oxide. Where if a closer look at the agglomerated lumps shows the presence of several nanoparticle aggregates. The surface morphology looks rough and thick, some particles appear elongated and granular like research by [15]. SEM surface morphology analysis can also determine particle size by measuring each particle using ImageJ Software. Figure 7 (b) is a bar chart of measurement results showing the distribution of particle sizes from a scale of 100 – 800 nm. The size of the ZnO nanoparticles obtained varies in the range of 170.4 nm to 758.5 nm with an average nanoparticle size of 402.4 nm. Based on the results, the size of the nanoparticles obtained shows a non-homogeneous particle size distribution. This can be seen from the large standard deviation value obtained, which is 141.63 nm. These results are similar to research where the particle size distribution is between 102 – 733 nm with an average particle size of 607 nm [16].

CONCLUSION

Based on the results of the analysis of the structural, optical and morphological properties of the synthesized ZnO nanoparticles, it can be concluded that red betel leaf extract can act as a reducing agent for zinc nitrate hexahydrate $Zn(NO_3)_2 \cdot 6H_2O$ solution. UV-Vis spectrophotometer absorption analysis showed an absorbance peak in the wavelength range of 250-330 nm with the highest absorbance in samples A (1:1), B (1:5), and C (1:10) respectively 0.39, 0.33, and 0.24 a.u. The XRD pattern shows that the nanoparticles have a Hexagonal wurtzite structure with a crystal size of 10.58 nm. SEM analysis shows that the ZnO nanoparticles have an inhomogeneous morphological shape with a non-uniform distribution. The average size of the ZnO nanoparticles is 402.4 nm.

ACKNOWLEDGMENTS

The author would like to thank LPPM Universitas Riau for funding this research under the 2024 RUUR scheme.

REFERENCES

1. Kahsay, M. H. (2021). Synthesis and characterization of ZnO nanoparticles using aqueous extract of Becium grandiflorum for antimicrobial activity and adsorption of methylene blue. *Applied Water Science*, **11**(2), 45.
2. Rhamdiyah, F. K., & Maharani, D. K. (2022). Biosynthesis of ZnO nanoparticles from aqueous extract of Moringa oleifera L.: Its application as antibacterial and

photocatalyst. *Indonesian Journal of Chemical Science*, **11**(2), 91–102.

3. Tjiang, D., Aritonang, H. F., & Koleangan, H. S. (2019). Sintesis nanopartikel Ag/$CoFe_2O_4$ menggunakan ekstrak daun binahong (*Anredera cordifolia* (Ten) Steenis) dan aplikasinya sebagai fotokatalis untuk mendegradasi zat warna methylene blue. *Chemistry Progress*, **12**(2).
4. Shim, Y. J., Soshnikova, V., Anandapadmanaban, G., Mathiyalagan, R., Perez, Z. E. J., Markus, J., Kim, Y. J., Castro-Aceituno, V., & Yang, D. C. (2019). Zinc oxide nanoparticles synthesized by Suaeda japonica Makino and their photocatalytic degradation of methylene blue. *Optik*, 182, 1015–1020.
5. Batubara, I., Rahminiwati, M., Darusman, L. K., & Mitsunaga, T. (2011). Tyrosinase activity of *Piper betle* and *Piper crocatum* essential oil. *Proceeding of The International Conference on Basic Science*, 50–53.
6. Rosalin, R. & Yasser, M. (2017). Pemanfaatan daun ketapang (*Terminalia catappa*) sebagai bioreduktor sintesis nanopartikel TiO_2 dan analisis sifat antimikroba. *Seminar Nasional Hasil Penelitian & Pengabdian Kepada Masyarakat (SNP2M)*, **2**.
7. Anugrahwati, M., Purwaningsih, T., Manggalarini, J. A., Alnavis, N. B., Wulandari, D. N., & Pranowo, H. D. (2016). Extraction of ethanolic extract of red betel leaves and its cytotoxicity test on HeLa cells. *Procedia Engineering*, 148, 1402–1407.
8. Xin, M. (2022). Crystal structure and optical properties of ZnO: Ce nano film. *Molecules*, **27**(16), 5308.
9. Madhumitha, G., Fowsiya, J., Gupta, N., Kumar, A., & Singh, M. (2019). Green synthesis, characterization and antifungal and photocatalytic activity of Pithecellobium dulce peel–mediated ZnO nanoparticles. *Journal of Physics and Chemistry of Solids*, **127**, 43–51.
10. Arifin, F. S. (2022). Biosintesis dan karakterisasi nanopartikel seng oksida (ZnO-NPs) menggunakan ekstrak daun kenitu (*Chrysophyllum cainito L.*). *Jurnal Teknik Kimia USU*, **11**(2), 56–63.
11. Amin, A. & Ananda, S. R. (2020). Sintesis dan karakterisasi nanopartikel Zn menggunakan kitosan sebagai reduktor. *Fullerene Journal of Chemistry*, **5**(2), 102–108.
12. Debanath, M. K. & Karmakar, S. J. M. L. (2013). Study of blueshift of optical band gap in zinc oxide (ZnO) nanoparticles prepared by low-temperature wet chemical method. *Materials Letters*, **111**, 116–119.
13. Thi Tran, Q. M., Thi Nguyen, H. A., Doan, V. D., Tran, Q. H., & Nguyen, V. C. (2021). Biosynthesis of zinc oxide nanoparticles using aqueous piper betle leaf extract and its application in surgical sutures. *Journal of Nanomaterials*, **2021**(1), 8833864.
14. Goudarzi, A., Zabihi, E., Shahrampour, D., & Heydari Sorshejani, M. (2022). Eco-friendly synthesis of large band gap ZnO nanoparticles by trisodium citrate: investigation of annealing effect on structural and optical properties. *Journal of Materials Science: Materials in Electronics*, **33**(29), 22798–22809.
15. Suresh, J., Pradheesh, G., Alexramani, V., Sundrarajan, M., & Hong, S. I. (2018). Green synthesis and characterization of zinc oxide nanoparticle using insulin plant (Costus pictus D. Don) and investigation of its antimicrobial as well as anticancer activities. *Advances in Natural Sciences: Nanoscience and Nanotechnology*, **9**(1), 015008.
16. Sari, R. N., Nurhasni, Y. M., & Yaqin, M. A. (2017). Sintesis nanopartikel ZnO ekstrak Sargassum sp. dan karakteristik produknya. *Jurnal Pengolahan Hasil Perikanan Indonesia*, **20**(2), 238–254.

IPC
Indonesian Physics Communication
Department of Physics, Universitas Riau, Pekanbaru, Indonesia
p-ISSN 1412-2960 | e-ISSN 2579-521X
Vol. 21 | No. 3
November 2024
Web: https://kfi.ejournal.unri.ac.id
E-mail: kfi@ejournal.unri.ac.id

Analysis and modelling of the characteristics of telecommunication antennas utilising metamaterials with a circular structure

Defrianto[1],*, Saktioto[1], Sofia Anita[2], Siti Zahroh[1], Yan Soerbakti[1], Tengku Emrinaldi[1]
[1]Department of Physics, Universitas Riau, Pekanbaru 28293, Indonesia
[2]Department of Chemistry, Universitas Riau, Pekanbaru 28293, Indonesia

*Corresponding author: defrianto@lecturer.unri.ac.id

ABSTRACT

The development of telecommunication antenna technology is increasingly being considered with the need for high and practical antenna performance. The antenna technology can be realized by using the split ring resonator (SRR) metamaterial structure. SRR metamaterial is a periodic material that has minimal manufacturing dimensions and is able to work at high frequencies. The ability of this metamaterial has the potential to be implemented in microstrip antenna structures as telecommunication applications. This study aims to design, simulate and analyze the characteristics of SRR-Circle metamaterials against the frequency function and application performance as a telecommunication antenna. The process is carried out using the Computer Simulation Technology (CST) Studio Suite Software which is operated at a working frequency of 0.009 – 9 GHz. The metamaterial structure is combined from 1 – 4 SRRs in the shape of a Circle with a fixed radius of 3.5 mm. The results of this study indicate the characteristics of metamaterials with negative values in relative permittivity (ε_r), relative permeability (μ_r) and refractive index (n) with the highest values in the metamaterial structure of the combination of 4 SRR-Circles, each with values of -144.33 Farad/m, -9.29 H/m and -9.07. In its application as a telecommunications antenna, metamaterials have succeeded in improving antenna performance. The highest antenna performance was obtained in the combination structure of 4 SRR-Circles with a return loss value of -34.37 dB, and a bandwidth of 1.00 GHz at a VSWR of 6.77 – 7.77 GHz. The results of this antenna performance have the potential to be applied to telecommunications antenna technology such as satellites, radars and 5G networks.

Keywords: Antennas, metamaterials, resonance, split ring resonator, telecommunications

Received 04-07-2024 | Revised 26-7-2024 | Accepted 03-08-2024 | Published 30-11-2024

INTRODUCTION

The development of information technology and the application of antennas has caused the need for information to continue to increase and has been widely used for applications in the field of telecommunications, one of which is satellites. Satellites are communication devices placed in outer space [1]. Metamaterials are artificial structures that have the characteristics of negative refractive index values and high resonance sensitivity. As a sophisticated technological breakthrough, the use of metamaterials has a very large impact with high and broad potential because the material and structure can be renewed [2]. The metamaterial material used is copper because of its good conductivity and electromagnetic response properties, allowing better control [3].

The use of microstrip antennas on metamaterials is the choice that is applied because it has high efficiency, low cost, simplicity of manufacture and easy integration into circuits. Microstrip antennas are metal conductive antennas mounted on a base plate used as microwaves in various modern telecommunications systems. The main components of a microstrip antenna consist of a ground connection plane, a substrate and a radiation patch. However, this antenna also has several disadvantages, such as low gain and narrow bandwidth [4]. The quality of an antenna can be determined by several simulation parameters from the S-parameter (scattering) such as return loss, VSWR (voltage standing wave ratio), gain and directivity. The metamaterial surface used can improve the characteristics of antenna parameters for communication applications, remote sensing and medical imaging [5].

Telecommunication is a technology and science of communication that involves the transmission of information over long distances using electromagnetic signals [6]. The use of antennas in communication technology can transmit communication signals without being blocked by obstacles. The technology used is satellite. Satellite technology is one of the wireless telecommunications technologies besides cellular communication systems. Satellite technology is expected to be able to reach a wide area even though there are hills, mountains or forests where the area is difficult to reach with cable telecommunications or cellular technology [1].

In this article, it is done by designing and simulating telecommunication antennas based on the characteristics of the circle structure using computer simulation technology (CST) Studio Suite. As a comparison, several simulation parameters from the S-parameter (Scattering) antenna with gain and bandwidth that will be used to obtain new breakthroughs in improving antenna performance and are expected to have potential use in satellite applications.

MATERIALS AND METHODS

Structure Design

The design of the SRR metamaterial structure was carried out using the CST Studio Suite 2019 software. The SRR unit consists of two concentric rings with the radii of the outer ring R_1, R_2 and the inner ring R_3, R_4. Where the size of the inner ring R_1 and the outer ring R_2 are designed with different sizes [2]. The material used in the SRR patch structure and microstrip antenna is copper as a metal inclusion or patch in the antenna application. Expected antenna parameters.

Table 1. Expected antenna parameters.

Parameters	Antenna characteristic
Working frequency	6 – 30 GHz [1]
Return loss	< -10 dB [7]
Bandwidth	≥ 1 GHz [8]
VSWR	≤ 2 [7]
Gain	≤ 3 dBi [1]

Figure 1. Combination structure 1 – 4 SRR-Circle with a fixed radius of 3.5 mm.

The number of cells is designed from one cell then varied into four circular metamaterial cells as in Figure 1 is a metamaterial structure with a combination of 1 – 4 SRR- Circles with a fixed radius of 3.5 mm to be analyzed. The selection of the design in this cell variation is intended to obtain a comparison in the relative permittivity constant (ε_r) relative permeability (μ_r) and refractive index (n) of the structure as in the following equation:

$$\mu_r = \frac{2}{jk_0 t_m} \frac{1 - V_2}{1 + V_2} \tag{1}$$

$$\varepsilon_r = \mu_r + j\frac{2S_{11}}{k_0 t_m} \tag{2}$$

$$n = \pm\sqrt{\varepsilon_r \mu_r} \tag{3}$$

The values of relative permittivity, relative permeability and refractive index of the structure can be determined by applying the NRW method to the S-parameters and phase values obtained during the simulation in CST Studio Suite [9].

The addition of circular metamaterial cells experiences a shift in the resonance frequency which causes a change in the E and B field induction to be lower for each structure. The constants ε_r and μ_r increase based on Maxwell's equations explained in the Literature review section. The relationship between **D** and **E** and **B** and **H** that occurs in linear, non-dispersive, and isotropic materials can be written as [10].

$$\boldsymbol{D} = \varepsilon \boldsymbol{E} = \varepsilon_r \varepsilon_0 \boldsymbol{E} \tag{4}$$

$$\boldsymbol{B} = \mu \boldsymbol{H} = \mu_r \mu_0 \boldsymbol{H} \tag{5}$$

Antenna Dimensions and Design

The dimensions of the SRR ring structure are T_s (substrate thickness), T_p (patch thickness), C_1 (gap and separation distance between rings) and C_2 (patch width) with variations in the number of combination structures 1 – 4. The dimensions of the structure used in this study can be seen in Table 2.

Table 2. SRR structure size.

Symbol	Size (mm)	Description
T_s	1.6	Substrate thickness
T_p	0.035	Patch thickness
C_1	0.43	Ring gap width
C_2	0.6	Patch width

The dimensions of the SRR structure can be seen in Table 1 The SRR structure to be designed is shown in Figure 3.

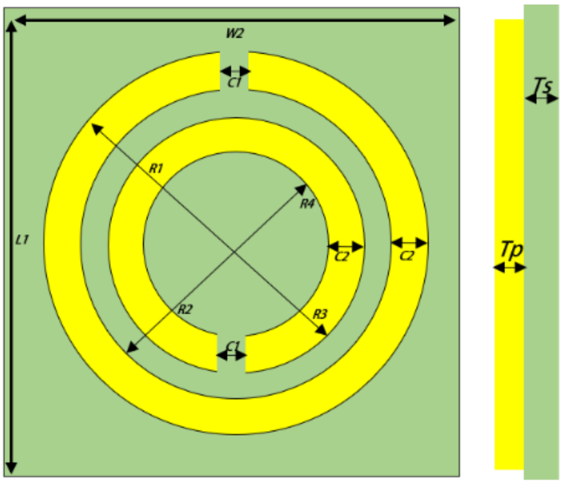

(a) (b)

Figure 3. SRR structure: (a) front and (b) side.

The structure type is applied to the design of a microstrip antenna from a combination of SRR structures. First, the formed SRR structure is analyzed to identify the properties of the metamaterial. Then, the placement of the feeding port and ground is used in the antenna.

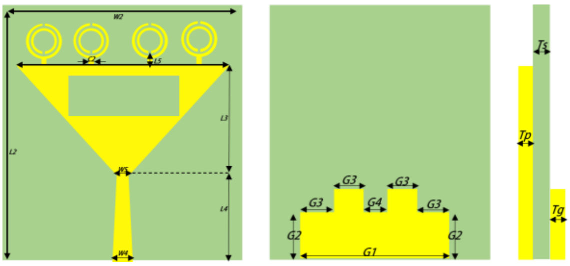

(a) (b) (c)

Figure 4. (a) Front SRR antenna structure after adding the feeding port, (b) rear ground structure, and (c) side.

Table 3. Design parameters of the SRR combination microstrip antenna.

Symbol	Dimension (mm)	Symbol	Dimension (mm)
C_2	0.5	W_4	2.14
L_2	33.34	W_5	1.8
L_3	14.46	G_1	24
L_4	11.20	G_2	7.4
L_5	0.54	G_3	5.43
W_2	29.60	G_4	3.94
W_3	27.84	T_g	0.035

RESULTS AND DISCUSSION

Testing of the metamaterial structure of the combination of 4 SRR-Circles in the form of relative permittivity values (ε_r), relative permeability (μ_r), and refractive index (n). While in the metamaterial structure antenna combination of 4 SRR-Circles focused on the resonance frequency values on return loss, VSWR, bandwidth, and gain obtained from the simulation results by applying the Nicolson-Ross-Weir (NRW) Equation. The working frequency used is 0.009 – 9 GHz.

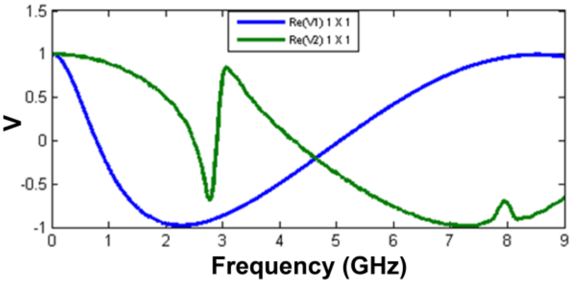

Figure 5. Graph of the real part V1 and V2 of the FR4 substrate (ε = 4.3).

Analysis of Figure 5 explains that Graphs V1 and V2 are the results of the sum of the S11 and S21 values. Graph V1 experiences resonance at a frequency of 2.27 GHz, while Graph V2 experiences two resonances located at frequencies of 2.81 GHz and 7.22 GHz. The resonance frequency is a characteristic of metamaterials based on the spectrum and transmission according to a certain phase magnitude depending on the shape of the metamaterial structure, Graphs V1 and V2 also experience a deflection of the polarization direction by the application of electric fields and magnetic fields given so that dispersion anomaly events (scattering interference) occur when the increase in relative permittivity (ε_r) and relative permeability (μ_r) decrease towards negative values. In addition, the resonance frequencies located on Graphs V1 and V2 also show the location of the resonance frequency on the permittivity and permeability as in Figure 6.

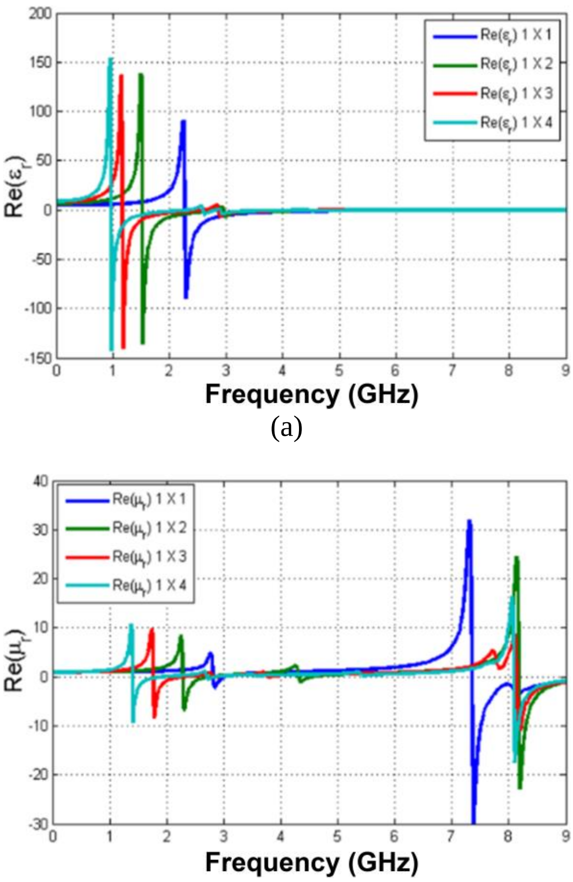

(a)

(b)

Figure 6. Graphs (a) ε_r, and (b) μ_r of metamaterial combination 1 – 4 SRR-Circle.

The effect of the combination of metamaterial cells 1 – 4 SRR-Circle on the metamaterial parameters in Figure 6 explains that the combination of 4 SRR-Circle metamaterial structure cells produces ε_r, μ_r, and n with negative values and the resonance frequency is greater than the metamaterial combination 1 – 3 SRR-Circle. This happens because the addition of the structure affects the properties of the material which is getting stronger (constructive) and the dielectric medium in the material causes the ability to polarize electrons by the resulting E and B field moments to become smaller. So that the influence on relative changes in permittivity and permeability of the material becomes greater.

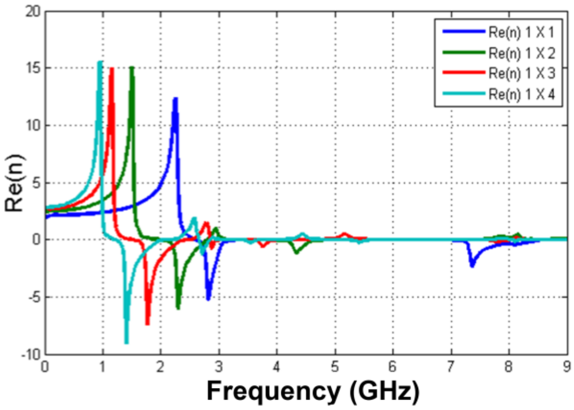

Figure 7. Refractive index graph metamaterial 1 – 4 SRR-Circle.

Figure 7 explains the occurrence of frequency shifts down towards low frequencies with increasing combinations of SRR- Circle metamaterial structures. The refractive index value in metamaterial 1 – 4 SRR- Circle produces a positive resonance frequency originating from the permittivity resonance frequency and vice versa at a negative frequency originating from the permeability resonance frequency so that the maximum refractive index value (n) is -9.07 at a frequency of 1.40 GHz as seen from metamaterial 4 SRR-Circle. The shift in resonance frequency cannot be separated from the contribution of the addition of circle metamaterial cells which causes changes in the E and B field induction to be lower for each structure. So that the constants ε_r and μ_r increase based on Maxwell's equations (4) and (5) explained in the Literature review section.

Identification of the characteristics of metamaterial parameters will be applied to the combination metamaterial structure 1 – 4 SRR-Circle in the form of an antenna as a telecommunications application. The standard quality of the antenna to be used as a detector in a telecommunications network that is good for wide coverage. Return loss and VSWR are one of the parameters that influence each other. The minimum RL value for the antenna application to work is -10 dB or 10% of the power transferred. The VSWR parameter is determined by the RL value obtained. VSWR has a value between 1 and 2 or $1 \leq \text{VSWR} \leq 2$. If RL has a value of -10 dB then VSWR will be equal to 2 and has a value of ≥ 1 when the RL value is lower -10 dB.

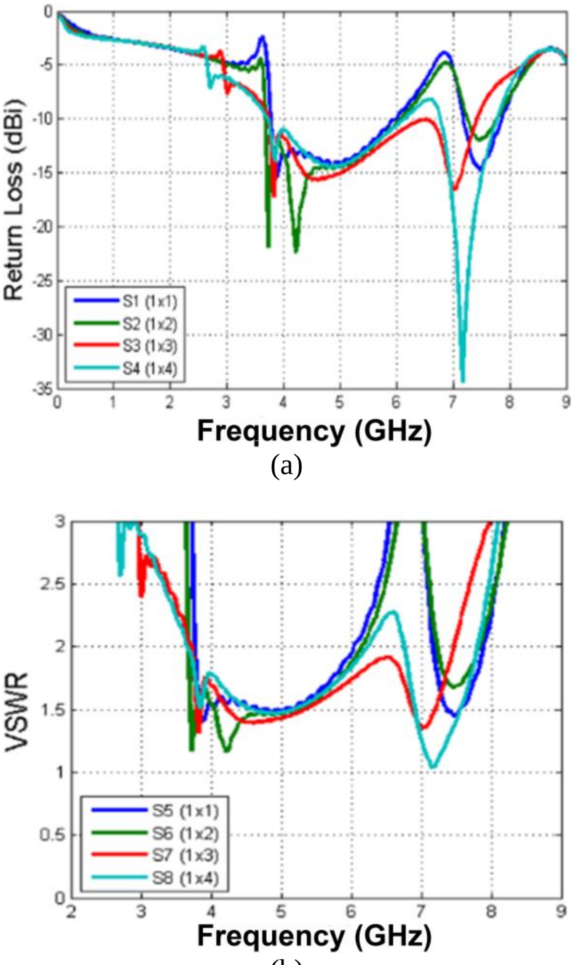

(a)

(b)

Figure 8. Graph (a) return loss and (b) VSWR of the antenna combination 1 - 4 SRR- Circle.

The graphs shown in Figure 8 (a) and (b) are changes in RL and VSWR of metamaterial antennas with variations in the combination of 1 – 4 SRR- Circle with a fixed radius of 3.5 mm. The difference in the combination of SRR-Circle causes the RL antenna parameters to change. As in the combination antenna 1 – 4 SRR- Circle which has a different resonant frequency and RL value.

Based on the simulation results, the RL value will be lower when the SRR- Circle metamaterial structure increases on the antenna. A lower RL indicates that the power received by the antenna is greater and makes the antenna work more optimally. RL increases from the addition of 1 SRR- Circle to 4 SRR- Circle with a value of -14.75 dB to -34.37 dB. This causes the VSWR frequency range and BW width to increase. It is proven from previous studies that the use of metamaterials in antennas can improve antenna parameters and also reduce the size of the antenna dimensions to be smaller and cheaper.

CONCLUSION

The design and simulation of metamaterial structures with cell variations of 1-4 Split Ring Resonator Circle (SRR-Circle) have been carried out with a geometry of less than 1/4 of the minimum wavelength. In the cell variation of 4 metamaterials with a 1 X 4 array arrangement, the relative permittivity (ε_r), relative permeability (μ_r) and refractive index (n) values are large, each with values of -144.33, -9.29, and -9.07 compared to the values in the 1-3 SRR-Circle structure. The application of metamaterials as antennas from the results of the analysis of the characteristics of metamaterials of cell variations obtained results that the return loss value was higher when the cell arrangement on the antenna increased. Return loss on the 4 SRR-Circle antenna structure has a large resonance frequency of 7.16 GHz with a return loss value of -34.37 dB compared to the 1-3 SRR-Circle structure which each have return loss values of -14.78 dB, -11.97 dB and -16.58 dB. In the 4 SRR-

Circle antenna structure with a 1 X 4 array arrangement in accordance with the specifications of the telecommunications antenna application, the antenna results on the circle structure antenna with a high frequency of 7.16 GHz, a return loss of -34.37 dB, and a bandwidth of 1.00 GHz at a VSWR of 6.77 - 7.77 GHz which can be operated on radar telecommunications antennas (satellites), 5G networks and IoT devices.

ACKNOWLEDGMENTS

The research was funded by LPPM Universitas Riau, in DIPA research grant with contract No. 14820/UN19.5.1.3/AL.04/2024.

REFERENCES

1. Rizqa, F., Arseno, D., & Yunita, T. (2020). Analisis Dan Desain Antena Mikrostrip Untuk Komunikasi Satelit Pada Frekuensi Ka-Band. *Aviation Electronics, Information Technology, Telecommunications, Electricals, Controls*, **2**(1), 1–12.
2. Saktioto, T., Syahputra, R. F., Punthawanunt, S., Ali, J., & Yupapin, P. (2017). GHz frequency filtering source using hexagonal metamaterial splitting ring resonators. *Microwave and Optical Technology Letters*, **59**(6), 1337–1340
3. Surjadi, J. U., Gao, L., Du, H., Li, X., Xiong, X., Fang, N. X., & Lu, Y. (2019). Mechanical metamaterials and their engineering applications. *Advanced Engineering Materials*, **21**(3), 1800864.
4. Huque, M. T. I. U., Hosain, M. K., Islam, M. S., & Chowdhury, M. A. A. (2011). Design and performance analysis of microstrip array antennas with optimum parameters for X-band applications. *International journal of advanced computer science and applications*, **2**(4).
5. Hossain, M. B., Faruque, M. R. I., Islam, S. S., & Islam, M. T. (2021). Modified double dumbbell-shaped split-ring resonator-based negative permittivity metamaterial for satellite communications with high effective medium ratio. *Scientific reports*, **11**(1), 19331.
6. Putri, S. M. (2017). Analisis Antena Mikrostrip Fraktal Sierpinski Gasket MIMO. *Jurnal Elektro dan Telkomunikasi*, **4**(2), 55–61.
7. Herudin, H. (2016). Perancangan Antena Mikrostrip Frekuensi 2, 6 GHz untuk Aplikasi LTE (Long Term Evolution). *Setrum: Sistem Kendali-Tenaga-elektronika-telekomunikasi-komputer*, **1**(1), 41–45.
8. Hasanuddin, Z. B. (2014). Design of Ka-band Satellite Links in Indonesia. *International Journal of Electronics and Communication Engineering*, **8**(8), 1299–1303.
9. Al-Bawri, S. S., Islam, M. T., Shabbir, T., Muhammad, G., Islam, M. S., & Wong, H. Y. (2020). Hexagonal shaped near zero index (NZI) metamaterial based MIMO antenna for millimeter-wave application. *IEEE Access*, **8**, 181003–181013.
10. Vendik, I. B. & Vendik, O. G. (2013). Metamaterials and their application in microwaves: A review. *Technical Physics*, **58**, 1–24.

Indonesian Physics Communication
Department of Physics, Universitas Riau, Pekanbaru, Indonesia
p-ISSN 1412-2960 | e-ISSN 2579-521X
Vol. 21 | No. 3
November 2024
Web: https://kfi.ejournal.unri.ac.id
E-mail: kfi@ejournal.unri.ac.id

Enhancing rural teacher competence in Meranti Islands Regency high school basic physics practical curriculum

Saktioto[1,*], Defrianto[1], Ari Sulistyo Rini[1], Dedi Irawan[2], Agrina[3], Sofia Anita[4], Yan Soerbakti[1], Mohammed Fisal Rabin[1]
[1]Department of Physics, Universitas Riau, Pekanbaru 28293, Indonesia
[2]Department of Physics Education, Universitas Riau, Pekanbaru 28293, Indonesia
[3]Department of Community Nursing, Universitas Riau, Pekanbaru 28293, Indonesia
[4]Department of Chemistry, Universitas Riau, Pekanbaru 28293, Indonesia

*Corresponding author: saktioto@lecturer.unri.ac.id

ABSTRACT

Teacher competency standards serve as benchmarks that can be utilised to assess the attributes deemed essential for professional competence in educators. Educators play a crucial and strategic role in the pursuit of national development objectives, particularly within the realm of education. However, the objective of education appears to be a reduction in competency standards at the conclusion of each academic year for specific subjects, particularly in the realm of science and Basic Physics. Consequently, this initiative seeks to inspire educators and students in secondary education to enhance their understanding of the educational process by engaging in the study of science, specifically Basic Physics, utilising appropriate tools and resources. The suggested mode of engagement involves the processes of instruction and education within secondary educational institutions across the Meranti Islands Regency, encompassing SMA, MAN, MTs, and SMP levels. This activity further offers insights into experiments and demonstration tools for educators in the realm of science and Basic Physics, facilitating a comprehension of concepts that range from simple to intricate natural phenomena through accessible demonstration media designed for practical application. In this manner, educators are anticipated to exhibit motivation and enthusiasm throughout the learning process, accompanied by a thorough and nuanced comprehension of the subject matter. To enhance teacher competency standards significantly, ensuring they become more qualified and professional.

Keywords: Physics education; research facility; physical sciences instruction; experimental

Received 09-06-2023 | Revised 02-07-2023 | Accepted 10-07-2024 | Published 30-11-2024

INTRODUCTION

Education plays a crucial and foundational role in shaping an individual's character, as outlined in Law No. 20 of 2003, which asserts that education fosters inherent potential manifested as spiritual and religious strength, self-discipline, character, intellect, ethical values, and the competencies necessary for conscious and deliberate engagement in society [1]. The aims of this educational endeavour are likely to encounter significant disruptions, rendering optimal achievement challenging, particularly in the aftermath of COVID-19 and at the onset of a new academic year following an extended break. The educational environment loses its appeal for students when it is characterised by monotony, a phenomenon particularly evident in the schools of the Meranti Islands Regency. This presents a significant challenge for educators and other stakeholders in enhancing curriculum proficiency and developing instructional materials that effectively facilitate the attainment of learning objectives, ensuring that students grasp the content thoroughly [2].

Meranti Islands Regency constitutes one of the administrative divisions within Riau Province, Indonesia, with Selat Panjang serving as its capital [3]. The district boasts a population of 206,116 individuals as of 2020, encompassing an area of 3,707.84 square kilometres [4]. The Meranti Islands Regency is situated at geographical coordinates ranging from approximately 0°42'30" to 1°28'0" N, and 102°12'0" to 103°10'0" E, positioned along the eastern coastline of Sumatra Island [5]. The Regional Government of the Meranti Islands Regency, particularly the Head of the Education Office, has endeavoured to enhance and uphold the quality of teacher competency annually by persistently assessing teacher evaluations at the conclusion of the academic year.

Science lessons, particularly in Basic Physics, necessitate educators to possess a wide array of competencies. It is insufficient to merely engage in the transmission of theoretical knowledge or rely solely on visual representations. A comprehensive grasp of science and Basic Physics demands an appreciation of extensive natural phenomena, logical reasoning, sensory experiences, and the assurance of observable natural facts [6]. Nonetheless, the implementation of the learning process may encounter challenges owing to the scarcity of resources for demonstrating scientific and fundamental physics practical work. Consequently, the majority of instruction is relegated to structured assignments for students, encompassing both theoretical frameworks and preliminary exposure to practical knowledge, primarily facilitated through accessible online platforms [7]. Consequently, students exhibit diminished motivation and enthusiasm during the learning process, leading to a less comprehensive understanding of the material [8]. The aforementioned explanation leads to the conclusion that one of the contributing factors is the insufficient competence of educators concerning the learning tools that may serve as effective media for instruction. Consequently, the endeavours and resolutions to these challenges present a chance for contemplation, broadening the perspectives on harnessing environmental potential. Furthermore, the use of straightforward equipment and materials as demonstrative tools by educators during the instruction of science and fundamental physics in the classroom is advocated.

MATERIALS AND METHODS

Community Service Location

The community service was carried out directly in Selat Panjang Timur, Tebing Tinggi District, Meranti Islands Regency, Riau Province, Postal Code 28753 as seen in Figure 1. Community service activities were carried out in several nearby Middle Schools throughout the Meranti Islands Regency which were carried out in one location in the Multipurpose Building Room of SMA N 1 Tebing Tinggi, Meranti Islands (see Figure 2).

Figure 1. Community service location in Selat Panjang, Meranti Islands Regency.

Figure 2. View of the interior of the Multipurpose Building.

There are several nearby Middle Schools at the SMA, MTs, MAN, and SMP levels in Selat Panjang that were invited to participate in the Fostered Village Program, such as:

- SMA Negeri 1 Tebing Tinggi, Jl. Pembangunan 2, Selat Panjang Tim., Kec. Tebing Tinggi, Meranti Islands Regency, Riau.
- SMA Negeri 2 Tebing Tinggi, Jalan Tutwuri, Selat Panjang Tim., Kec. Tebing

Tinggi, Meranti Islands Regency, Riau 28753.

- State Senior High School 3 Tebing Tinggi, Banglas, Tebing Tinggi, Meranti Islands Regency, Riau 28753.
- State Senior High School 1, Meranti Islands, located on Jl.
- State Junior High School 1, Meranti Islands, located on Jl.
- Teuku Umar, Selat Panjang Bar., Tebing Tinggi District, Meranti Islands Regency, Riau.
- State Junior High School 2 Tebing Tinggi, South Selat Panjang, Tebing Tinggi, Meranti Islands Regency, Riau.
- State Junior High School 3 Tebing Tinggi, Jl. Siak No.5, Selat Panjang Bar., Tebing Tinggi District, Meranti Islands Regency, Riau.
- SMP Negeri 4 Tebing Tinggi, Banglas Bar., Tebing Tinggi District, Meranti Islands Regency, Riau 28753.

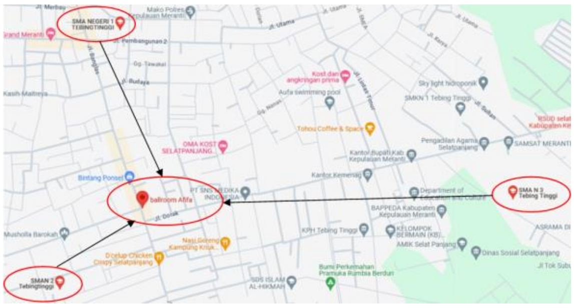

Figure 3. Distance of each Senior High School to the service location.

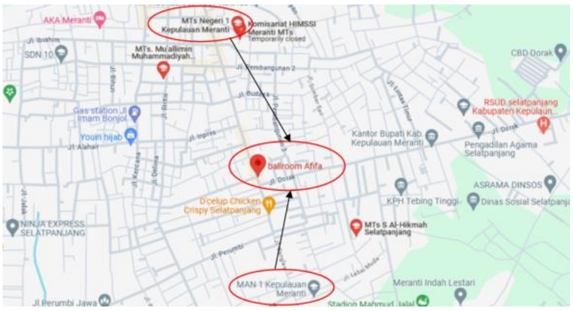

Figure 4. Distance of MTs and MAN Senior High Schools to the service location.

Service Design

The proposed form of activity is in the form of teaching and learning through experimental guidance and demonstration tools for science or science teachers. Basic experimental learning about understanding concepts from simple to complex natural phenomena by displaying equipment and materials for practical work as well as demonstration tools directly. Furthermore, it will be tested on students and introduced to parents. This practical experiment tool can be displayed both in mechanical and non-mechanical (electromagnetic) forms physically in the form of simulations and real practices that can be accepted by the senses, hearing, and sight.

This activity is also carried out using synchronous and asynchronous methods. The development of innovation and creativity in the learning process of practical work with this demonstration includes understanding:

- Systematic approach: understanding natural events that have a causal relationship, a sequence of events that produce a work or product that can then be concluded.
- Historical approach: activities in the process and timeline and changes in events that show the effects and gains that produce an understanding.
- Summary approach: clearly and precisely related event premises from a series of natural events, connected, analogized and compared to produce a conclusion of an event.
- Comparative approach: providing analogies of events and comparisons of both the process and results of a natural phenomenon that can be developed and concluded.

Activity and evaluation methods include in this empowerment:

- Providing material: Basic concepts of science / Basic Physics.
- Demonstration of equipment and materials for practical work.
- Process and testing of experimental tools and materials.
- Repetition and simulation understanding approach: Measurement and calculation.
- Oral and written evaluation: Simulation exercises and independent demonstrations.

The activities are detailed in the following modules:

- Uniform straight motion.
- Spring constant and Hooke's law.
- Standing waves and sound.
- Magnetism and electromagnetic induction.
- Ohm's law and electrical circuits.
- Fluid viscosity and Archimedes' Law.
- Potential and Coulomb Field.
- Capacitor plate electric field and potential.
- Wheatstone bridge.

RESULTS AND DISCUSSION

Overview of the Target Community

In general, teaching staff in secondary schools in the Meranti Islands are relatively young, around 25-30 years old, with little teaching experience. The ratio of male teaching staff is very small compared to female teaching staff, around 1:4 of the total attendance. However, the enthusiasm for learning for teaching staff can be seen from the success of improving teaching skills from online practical simulations. With this program and the potential of teaching staff, it is hoped that physics or science teachers will be able to develop teaching methods using simple practical tools to attract students' interest in learning and increase their knowledge of learning and teaching in class [9].

Figure 5. Implementation of community service activities in the meeting room.

Potential for Community Development (Empowerment)

Teachers in secondary schools in the Meranti Islands Regency who are relatively young have the potential to increase their knowledge with enthusiasm for learning. Therefore, innovative learning service activities need to be carried out with interesting methods with simple practicals. In addition, in today's modern technological world, learning can be done via the internet or online with several interesting methods and videos of course [10].

Educators or teachers are required to have an up-to-date spirit or know the development of existing science, especially physics and science at the secondary school level. However, this requires motivation and guidance for teachers to realize innovative and interesting learning with community service activities carried out online by lecturers from the University of Riau.

Community Empowerment Solutions

Increasing the knowledge of educators or teachers needs to be done by delivering motivation and innovative learning of physics and science using simple practical methods. This activity is very important with a visual approach and interesting things that have never been practiced. This activity was carried out online at the end of the COVID-19 pandemic to minimize the rise of new variants [11].

The community service program for teachers was carried out in various secondary schools in the Meranti Islands Regency in a hybrid manner. The development of student insight is also carried out by providing practical videos or simple research on physics and science phenomena. In addition, the assessment of the achievement indicators of community service is carried out with short and quick tests for teachers. The indicators in question are increasing the knowledge and skills of students in learning physics in the classroom [12].

Figure 6. Enthusiasm of community service participants.

Level of Achievement of Program Targets

Community service activities in developing creativity in physics learning using simple online practical tools have been successfully implemented. The Meranti Islands community has a high level of enthusiasm for working together to make the community service activities that have been carried out online a success. The level of achievement can be seen from the indicators obtained from short and quick tests for teachers. However, before starting the learning activities, students were given a test first to measure how far their insight and knowledge they had. The results of the first test obtained were still less than satisfactory from all teacher participants. Thus, innovative learning and motivation by lecturers were carried out for teachers [13].

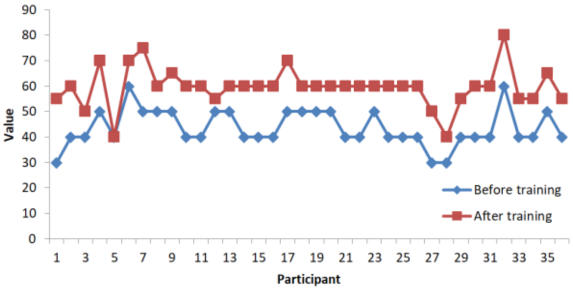

Figure 7. Statistical data on increasing teacher knowledge and skills.

This learning activity is carried out offline by practicing several phenomena of physics and science using simple tools. Then for each experiment, teachers are given the opportunity to ask questions and try them, then given some interesting materials from the lecturers. After the learning activity is carried out, a short and quick test is carried out to determine changes in achievement indicators in increasing knowledge and skills. The results of the second test obtained were very satisfactory with an increase in indicators of 20% (see Figure 7). These results prove that learning physics and science can be more easily understood with the help of a visual approach from practicums using simple tools [14].

CONCLUSION

An innovative learning model to encourage teachers' self-confidence in conducting experiments through simple practical media, believing that science and physics experiments can be carried out with simple equipment and tools, and successfully revealing some misconceptions about science and physics materials that have not been fully revealed, among others, have been successfully resolved and provided significant results.

ACKNOWLEDGMENTS

The research was funded by LPPM Universitas Riau in DIPA research grant with contract No. 15726/UN19.5.1.3/AL.04/2024.

REFERENCES

1. Ichsan, F. N. (2021). Implementasi perencanaan pendidikan dalam meningkatkan karakter bangsa melalui penguatan pelaksanaan kurikulum. *Al-Riwayah: Jurnal Kependidikan*, **13**(2), 281–300.
2. Okvireslian, S. (2021). Pemanfaatan aplikasi Whatsapp sebagai media pembelajaran dalam jaringan kepada peserta didik paket B Uptd Spnf Skb Kota Cimahi. *Comm-Edu (Community Education Journal)*, **4**(3), 131–138.
3. Syahrul, S., Dewita, D., & Restu, R. (2018). Implementasi pewarna alami untuk diversifikasi mie sagu ikan pada pelaku usaha mikro mie sagu di Kabupaten Kepulauan Meranti, Riau. *Riau Journal of Empowerment*, **1**(1), 31–36.
4. Ratnasari, C., Yuliantoro, Y., & Fikri, A. (2021). Eksistensi Kelenteng Hoo Ann Kiong sebagai objek wisata budaya di Kabupaten Meranti. *INNOVATIVE: Journal Of Social Science Research*, **1**(2), 393–398.
5. Pinandita, M. A., Yuliani, G., Subarnas, A., Widhiyatna, D., & Mutiara, S. (2020). Karakterisasi dan estimasi sumber daya

gambut sebagai material adsorben logam berat dalam larutan di Blok Teluk Meranti, Kabupaten Pelalawan, Provinsi Riau. *Buletin Sumber Daya Geologi*, **15**(2), 101–115.

6. Fatmawati, E. (2020). Kerjasama orang tua dan guru dalam meningkatkan motivasi belajar peserta didik. *IBTIDA'*, **1**(2), 135–150.
7. Habibah, B. M., Mulyani, S., Nia, N. I., & Nugroho, P. (2020). Konsep layanan responsif bagi siswa yang mengalami kesulitan belajar secara daring dimasa pandemi covid-19. *Konseling Edukasi: Journal of Guidance and Counseling*, **4**(2), 305–322.
8. Annur, M. F., & Hermansyah, H. (2020). Analisis kesulitan mahasiswa pendidikan matematika dalam pembelajaran daring pada masa pandemi covid-19. *Paedagoria: Jurnal Kajian, Penelitian Dan Pengembangan Kependidikan*, **11**(2), 195–201.
9. Hayati, M. (2023). Penerapan Pendekatan Pembelajaran Berbasis Multiple Intelligences Dalam Pembelajaran Pendidikan Agama Islam. *Jurnal Penelitian Multidisiplin*, **2**(6), 1–18.
10. Chandramidi, M. (2022). Pengembangan model pembelajaran problem based learning berbasis aplikasi tracker untuk meningkatkan pemahaman konsep fisika. *Journal of Learning and Technology*, **1**(2), 51–62.
11. Kurniasari, W., Murtono, M., & Setiawan, D. (2021). Meningkatkan minat belajar siswa menggunakan model blended learning berbasis pada google classroom. *Jurnal Educatio Fkip Unma*, **7**(1), 141–148.
12. Defrianto, D., Saktioto, S., Setiadi, R. N., Farma, R., Soerbakti, Y., & Rabin, M. F. (2023). A simple understanding of physics from an Islamic perspective at the As-Shofa Islamic School Pekanbaru. *Journal of Innovation and Creativity Resources*, **2**(1), 13–18.
13. Defrianto, D., Saktioto, S., Setiadi, R. N., Farma, R., & Soerbakti, Y. (2023). Realization of post-COVID-19 hybrid physics learning at Al-Ulum Islamic School in Pekanbaru. *Journal of Innovation and Creativity Resources*, **1**(2), 59–62.
14. Anita, S., Saktioto, S., Syamsudhuha, S., Defrianto, D., Soerbakti, Y., & Rabin, M. F. (2022). Management of high school laboratory for experimental optimization of physics education. *Journal of Innovation and Creativity Resources*, **1**(1), 7–12.

JOURNAL EDITOR'S DECISION LETTER

INDONESIAN PHYSICS COMMUNICATION

Number: 003/Retraction/IPC/III/2025
Date: April 22, 2025

About Article Retraction

After considering the request for article retraction submitted by the author, we, as the editor of the Indonesian Physics Communication Journal, have conducted an evaluation and investigation regarding the reasons for the retraction submitted. Article data information below:

Authors **:** Elvina Putri, Iwantono Iwantono, Zulkarnain Zulkarnain, Jan Setiawan

Article Title **:** Analysis of the effect of calcination and substitution on the phase properties of strontium-hydroxyapatite

DOI Number **:** 10.31258/jkfi.21.3.245-256

Journal **:** Indonesian Phyics Communication

Based on the evaluation results, we decided to approve the retraction of the article with the following considerations:

1. **Reason for Withdrawal**: There was an ethical violation in the implementation of research activities as disclosed by the author.
2. Responsibility: The retraction of this article is only valid within the scope of the official database and archives of the Indonesian Physics Communication Journal. We are not responsible for the distribution of articles in third-party databases or other open sources.
3. **Retraction Fee**: In accordance with applicable regulations, the author will be charged a retraction fee which must be paid before the official retraction process is carried out.

Hereby, we declare that the article will be removed from publication and will no longer be available in the Indonesian Physics Communication Journal database.

We appreciate the authors' commitment to maintaining scientific integrity and hope that this decision can be a lesson for all parties in maintaining publication ethics.

Thus we have made this decision letter so that it can be used as it should.

Best regards,

Editor
Indonesian Physics Communication
Jurusan Fisika FMIPA Universitas Riau
Email: kfi@ejournal.unri.ac.id

Indonesian Physics Communication
Department of Physics, Universitas Riau, Pekanbaru, Indonesia
p-ISSN 1412-2960 | e-ISSN 2579-521X
Vol. 21 | No. 3
November 2024
Web: https://kfi.ejournal.unri.ac.id
E-mail: kfi@ejournal.unri.ac.id

FTIR and Raman studies of manganese phosphate glasses

Agus Setyo Budi*, Hadi Nasbey, Iwan Sugihartono
Department of Physics, Universitas Negeri Jakarta, East Jakarta 13220, Indonesia

*Corresponding author: agussb1963@gmail.com

ABSTRACT

Raman and infrared (IR) spectra of $xMn_2O_3(1-x)P_2O_5$ glasses (x = 5 mol% – 25 mol%) are reported. The spectral shift is related to changes in the coordination of the neodymium ion. The changes observed are consistent with an elongation of P–O$^-$ terminal and P–O–P bridging bonds in the PO_4 tetrahedra.

Keywords: Infrared; PO_4 tetrahedra; Raman

Received 05-09-2023 | Revised 02-10-2023 | Accepted 15-10-2024 | Published 30-11-2024

INTRODUCTION

Glasses are widely used mainly because they are transparent in the visible spectral range. We are now entering an era when it has become at least as significant to process and transmit information rapidly [1]. Phosphate glasses have very interesting molecular structures and some unique physical properties such as high thermal expansion coefficients, low transition and softening temperatures and low preparation temperatures. Metaphosphate glasses containing rare earth ions have potentially important applications in optical communications and laser technologies [2, 3]. Glasses of the $R(PO_3)_3$ formula (where R represents one of the lanthanide ions) have been reported to exhibit the largest magnetic contributions to the low temperature specific heats known in oxide glasses [4]. Sm and Eu phosphate glasses are unusual in having a negative hydrostatic pressure dependence of bulk modulus and a negative coeeficient of thermal expansion [5]. The promising physical properties of the rare earth phosphate glasses have initiated many studies of their structure including EXAFS and Neutron diffraction [6], and Mossbaur spectroscopy [7]. Raman and IR spectroscopy have been used for investigation of the molecular structure of phosphate glasses [8]. However for phosphate glasses having band gaps in visible or near infrared, the intrinsic optical transitions of the glass overlap some of the intra 4f-shell transitions of the rare-earth dopants. The relevant optical transitions of host glass can be summarize in terms of the optical spectrum [9].

In this paper we report our results and interpretation on IR and Raman spectra of Mn_2O_3-P_2O_5 glasses. Previous investigations on d.c. electrical conduction of neodymium phosphate glasses showed that the electronic conduction is due to hopping of an electron from lower valence state (Nd^{2+}) to higher valence state (Mn^{3+}) of manganese ions [10].

EXPERIMENTAL

Preparation of Sample

Neodymium phosphate glasses of general formula $x(Mn_2O_3)1-x(P_2O_5)$ were prepared by melting mixtures of high-purity dry manganese oxide with phosphorus pentoxide P_2O_5 in a closed platinum crucible of 80 cm^3 capacity. To react the constituents, the mixture of manganese oxide and phosphorus pentoxide in the crucible was heated in an electrical furnace at a temperature was progressively increased, reaching a maximum of approximately 1500ºC. To ensure proper mixing and homogeneity, the molten liquid was shaken frequently and vigorously. After being checked, the melt was cast by pouring as fast as possible into a hot steel split mould to quench to form a glass. The glass was immediately transferred to an annealing furnace at 500ºC where it was kept for 3 h to relieve any residual stress which could cause embrittlement. At the end of this annealing process, the furnace was switched off and the glass left to cool down to the room temperature gradually by controlled thermal treatment at cooling rate of 0.5ºC/min. The sample were selectively cut, ground, and polished. After preparation, samples were stored in plastic containers in a dessicator.

Measurements of IR Spectra

A Perkin Elmer 1600 Fourier-transform infrared (FTIR) have been used to investigate to all sample prepared using the KBr pellet technique. Typically around 2 mg of the finely ground sample is mixed with 200 mg of KBr powder and the mixture then pressed for 4 minutes, in evacuable die under 10 tons of pressure to give a transparent disk with a surface area of 1 cm^3. The FTIR spectra were recorded in the spectral range of 4000 – 400 cm^{-1} resolution and 64 scans to ensure a good signal to noise ratio.

Raman Spectroscopy

Powder samples were used for measurement of Raman spectroscopy (2000R NIR FT-Raman). An Nd:YAG laser (an yttrium aluminum garnet crystal doped with triply-ionized neodymium) at the wavelength 810 nm was used for sample excitation. Power of the laser at the sample was typically ~300 mW. Spectra of the samples were taken in the frequency region between 100 cm^{-1} and 3500 cm^{-1} at a spectral bandpass of 1 cm^{-1}.

RESULTS AND DISCUSSION

Infrared absorption

The IR spectra of $x(Mn_2O_3)1\text{-}x(P_2O_5)$ are shown in Figure 1 and Table 1. The spectra of glasses show five major peak vibration bands at around 1251, 1072, 915, 776.5, and 481 cm^{-1}. Significant changes occur in both intensities and band shapes as a function of composition. These bands can be assigned to $\nu_{as}PO_2$, $\nu_{a}PO_2$, $\nu_{as}POP$, $\nu_{a}POP$, and δPO_2 modes of $(PO_3)_n$ chain groups, respectively [11].

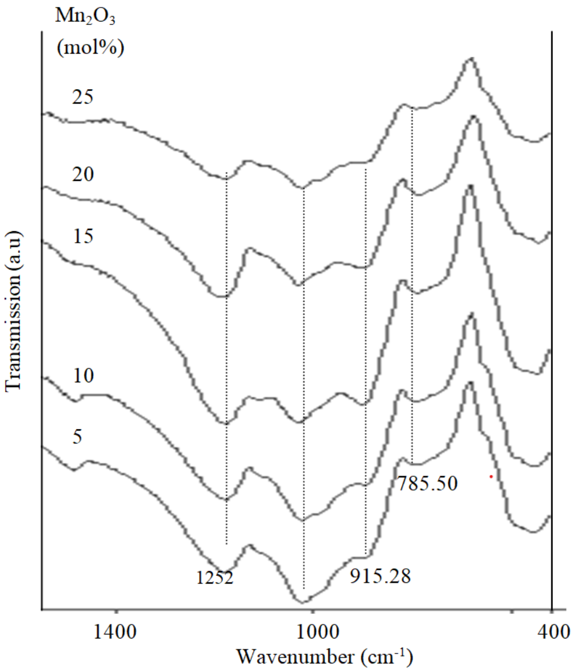

Figure 1. IR spectra of $xMn_2O_3(1\text{-}x)P_2O_5$ glasses, with $0.05 \leq x \leq 0.25$.

The results are very similar to those of the metaphosphate glasses studied by Corbridege [12], Exarhos et al. [13], Karabulut [14], and Hudgens [15]. The band frequency shifts continuously from 1251 cm^{-1} at $(Mn_2O_3)_{0.05}(P_2O_5)_{0.95}$ to 1262.46 cm^{-1} at $(Mn_2O_3)_{0.2}(P_2O_5)_{0.8}$ sample. However there are no significant structural changes to the network and there is no evidence for presence of significant concentrations of terminal groups ($\nu_{as}PO_3$ at 1255.51 cm^{-1}). These observations are consistent with the analyzed compositions which yield O/P ratio of $\approx$2.69 [16] and so PO_3 groups as indicated by the presence of the IR band at 1255.51 cm^{-1}. In addition to the relatively low frequency position of the band at 481 cm^{-1}, are in part due to cross linked three dimensional phosphate structure. This observation is an agreement with results obtained [17]. The band at 776.5 cm^{-1} is assigned to P–O–P ring frequency in the part of three dimensional network relatively free of chain. Generally the structure of the v_sPOP band is considered as the most characteristic one in the spectra of metaphosphate since it appears in a frequency range free from other vibrational frequencies [18]. In addition, the v_sPOP bands are very sensitive to changes since the frequency is strongly dependent on POP bond angle.

Table 1. Infrared spectra of glasses in the region 1500 – 400 cm^{-1}.

Glass	Position of prominent absorption maxima (cm^{-1})				
$5Mn_2O_3 + 95P_2O_5$	1251_s	1072_s	915_{ms}	776.5_m	481_m
$10Mn_2O_3 + 90P_2O_5$	1254.29_s	1062.23_s	898.3_{ms}	780.5_m	490.37_m
$15MN_2O_3 + 85P_2O_5$	1254.26_s	1062.22_s	898.3_s	779.45_m	487.33_m
$20MN_2O_3 + 80P_2O_5$	1262.46_s	1068.49_{ms}	912.85_{ms}	774.66_m	484.57_m
$25MN_2O_3 + 75P_2O_5$	1255.51_{ms}	1060.49_{ms}	912.54_{sh}	-	492.58_m

Note: s, strong; ms, medium strong; m, medium; sh, shoulder

Raman Spectra

The Raman spectra of all glasses were obtained. For binary manganese phosphate glasses, the spectra exhibit major variations as a function of manganese concentration, x, over the x = 5 mol% to x = 25 mol%. These are evident in the 1170 – 1250 cm^{-1}, 970 – 1100 cm^{-1}, and 730 – 780 cm^{-1}, as well as lower frequency regions of the Raman spectra in Figure 2 and Table 2.

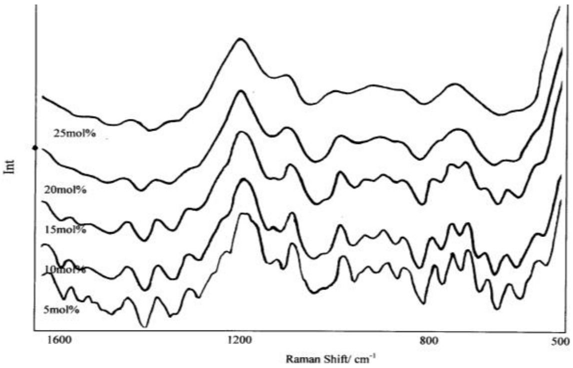

Figure 2. Raman spectra of $xMn_2O_3–(1-x)P_2O_5$ glasses, with $5 \leq x \leq 25$.

The change in frequency and relative intensity of the band maximum at 1360 cm^{-1} to shoulder at 1177.87 cm^{-1} with a change in x = 25 mol% is quite dramatic. Band contour analysis shows that this feature is not due to one band shifting but to the change in relative intensity of two bands at 1085.95 cm^{-1} and 1177.87 cm^{-1}, whose convoluted band maximum shifts. These bands are due to the asymmetric PO_2 stretch of PO_2 units in the chain but with different bonding configurations relative to the rare earth ions [19]. As x increases a shoulder at 1360 cm^{-1}, due to stretch of uncoordinated P=O units disappears, and the strongest band due to the PO_2 symmetric stretch broadens and shift from 977.02 cm^{-1} to lower frequency.

The Raman band at 731.91 – 710.65 cm^{-1} is assigned to predominately P–O–P stretching mode involving imperturbed chain and residual ring units in the P_2O_5 rich glasses. It decreases in intensity and is replaced by the band 710.65 cm^{-1} when x exceeds 10 mol%.

Several bands have been observed in the region of the spectrum containing out of chain PO_2 vibration. Two main bands at around 1270 cm^{-1} and 1420 cm^{-1} in this region are present in the spectra of metaphosphate glasses and assigned to the asymmetric stretch of PO_2 and P=O, respectively [20].

Table 2. The Raman peak positions for $xMn_2O_3–(1-x)P_2O_5$ glasses.

Sample	Absorption peak (cm^{-1})				
S_1	706.38	746.38	985.10	1142.55	1189.36
S_2	708.21	748.26	988.34	1144.23	1192.42
S_3	710.52	754.63	989.21	1149.41	1194.62
S_4	716.36	-	992.46	1152.36	1198.21
S_5	721.27	-	1021.27	1163.13	202.36

For all the glasses, the broad bands are observed in the wavenumber region between 400 – 600 cm^{-1}. Their assignment is not unambiguous because these bands are due to complicated internal vibration such as the skeletal deformation vibration of phosphate chains and PO_3.

CONCLUSION

Stable phosphate glasses containing up to 25 mol% Mn_2O_3 can be obtained by ordinary melt quenching. IR spectroscopy reveals that the glass networks are dominated by bridging P-tetrahedra that constitute the metaphosphate chains, with some chain-terminating sites in glasses with O/P ratio 2.69. The Raman bands reveal that the manganese ion interacts more covalently with phosphate anions in glasses leading to a redistribution of PO_2 (POP) bond angels and lengths. Minor variations in the concentration of Mn_2O_3 around the metaphosphate composition lead to different structures and oxygen environment for the rare-earth ion in glass.

REFERENCES

1. Petrovskii, G. T. (1990). On the optical properties of glasses. *J. Non-Cryst. Solids*.
2. Karabulut, M., et al. (2001). Structure and properties of lanthanum–aluminum–phosphate glasses. *J. Non-Cryst. Solids*.
3. Bishop, S. G., et al. (2000). Excitation of rare earth emission. *J. Non-Cryst. Solids*.
4. Wood, D. L. & Tauc, J. S. (1972). Weak absorption tails in amorphous semiconductors. *Phys. Rev. B*, **5**(8), 3144.
5. Mott, N. F. & Davis, E. A. (2012). *Electronic processes in non-crystalline materials*. OUP Oxford.
6. Prakash, G. V., et al. (2001). Linear optical properties of niobium-based tellurite glasses. *Solid State Commun.*, **119**(1), 39.
7. Davis, E. A. & Mott, N. (1970). Conduction in non-crystalline systems V. Conductivity. *Phil. Mag.*, **22**(179).
8. Urbach, F. (1953). The long-wavelength edge of photographic sensitivity and of the electronic absorption of solids. *Phys. Rev.*.
9. Ratnakaram, Y. C. & Reddy, A. V. (2000). Electronic spectra and optical band gap studies. *J. Non-Cryst. Solids*, **277**(2-3).
10. Arzeian, J. M. & Hogarth, C. A. (1991). Some structural, electrical and optical properties. *J. Mater. Sci.*, **26**, 5353–5366.
11. Bridge, B., et al. (1983). On the elastic constants and structure of the pure inorganic oxide. *Phys. Status Solidi A*, **77**.
12. Corbridge, D. E. C., et al. (1966). *Topics in phosphorus chemistry*. Interscience.
13. Exarhos, G. J., et al. (1974). Interionic vibrations and glass transitions in ionic oxide metaphosphate. *J. Chem. Phys.*, **60**.
14. Karabulut, M., et al. (2001). Structure and properties of lanthanum–aluminum–phosphate glasses. *J. Non-Cryst. Solids*.
15. Hudgens, J. J. & Martin, S. W. (1993). Glass transition and infrared spectra of low-alkali, anhydrous lithium phosphate glasses. *J. Am. Ceram. Soc.*, **76**(7), 1691.
16. Budi, A. S., et al. (2002). Study of fractal bond connectivity of neodymium phosphate glasses. *Jurnal Teknologi*, 11.
17. Ilieva, D., et al. (2001). FT–IR and Raman spectra of Gd phosphate crystals and glasses. *J. Non-Cryst. Solids*, **293**, 562.
18. Znášik, P. & Jamnický, M. (1992). Preparation, infrared spectra and structure of glasses in the system $CuCl-Cu_2O-(P_2O_5+MoO_3)$. *J. Non-Cryst. Solids*, **146**.
19. Wong, J. & Angell, C. A. (1971). Application of spectroscopy in the study of glassy solids, Part II. *Appl. Spectrosc. Rev*.
20. Muller, K. P. (1969). Struktur und Eigeinschaften von Glasern und glasbildenden Schmelzen. *Glastechn. Ber*.

IPC
Indonesian Physics Communication
Department of Physics, Universitas Riau, Pekanbaru, Indonesia
p-ISSN 1412-2960 | e-ISSN 2579-521X
Vol. 21 | No. 3
November 2024
Web: https://kfi.ejournal.unri.ac.id
E-mail: kfi@ejournal.unri.ac.id

Synthesis and characterization of activated carbon based on young coconut fiber as a supercapacitor electrode

Dio Davana Firdaus Nasution, Awitdrus*
Department of Physics, Universitas Riau, Pekanbaru 28293, Indonesia

*Corresponding author: awitdrus@lecture.unri.ac.id

ABSTRACT

Supercapacitor is energy storage devices consisting of electrodes, electrolyte, current collectors, and separator. In this research, carbon electrodes are made from young coconut fiber biomass (SKM) waste using $ZnCl_2$ 0.5 M as activation agent and variations in physical activation temperatures. Carbon electrodes preparation begins with a pre-carbonized process of 200ºC temperatures for 1 hour and 30 minutes, chemical activation using $ZnCl_2$ 0.5 M as activation agent, then the carbonization process uses N_2 gas as well as physics activation using CO_2 in temperature variation of 700ºC, 750ºC, and 800ºC. Analysis of the nature of electrodes cell capacitor based fiber young coconut fibers sample shows that the activation physics 750ºC sample is best, agreeble with the density of carbon electrodes declined by 40.43% after the carbonization-activation process. Carbon electrodes represent semicrystalline based on the characterization of the X-ray diffraction, marked with a ramp peak at 2θ at about 24º and 45º. The SKM-750 has a highest of L_c/L_a ratio an average number of microcrystalline inner layers (N_p), are 0.9 and 3.55. SKM-750 has the highest of specific capacitance value, namely 245.45 F/g.

Keywords: Activated carbon; electrode; physical activation; supercapacitor; young coconut fiber

Received 15-09-2023 | Revised 12-10-2023 | Accepted 02-11-2024 | Published 30-11-2024

INTRODUCTION

The energy crisis is one of the biggest problems in modern life, because energy supplies are running low. The solution that can be done to overcome this energy crisis is to use electrical energy to prepare for future energy. The use of very large energy in everyday life indicates the need for electrical energy storage media that is also very strong and durable.

This storage device has the attention of every country. One of them is a supercapacitor. Supercapacitors are widely used in industrial power and memory backup systems and energy management [1]. Supercapacitor components consist of electrode materials, electrolytes, current collectors, and separators. All components contribute to the performance of supercapacitor storage, but electrode and electrolyte materials play an important role [2]. One important component of a supercapacitor is the electrode. This electrode can affect the capacitance value that will be produced by the supercapacitor. The electrode is in the form of activated carbon which can be produced from biomass (organic material) which goes through a chemical and physical activation process.

Biomass that has the potential to be used as a carbon electrode in a supercapacitor is young coconut fiber. Coconut is a tropical plant that has long been known to the public. Coconut is a commodity strategy that has a social, cultural and economic role in the lives of Indonesian people. Young coconut fiber is the largest component of a coconut, the outermost part of the coconut fruit that wraps the coconut shell. The thickness of the coconut fiber ranges from 5 – 6 cm consisting of the outer layer 8 (exocarpium) and the inner layer (endocarpium). Young coconut fiber consists of fiber and also cork which functions to connect one fiber to another. Each coconut has 0.4 kg of fiber consisting of 30% fiber [3].

Young coconut fiber contains tannin compounds or tannic acid around 4.28%, while young coconut cork contains tannin compounds around 5.62%. Tannin has antibacterial activity against *Eserichia coli* and *Staphylococcus* *aureus* [4]. Young coconut fiber also contains 29.4% lignin, 26.6% cellulose, and 27.7% hemicellulose [5].

RESEARCH METHODS

This research method explains the procedure for making carbon electrodes for supercapacitor cells based on young coconut fiber. Young coconut fiber is separated from its cork. then dried in the sun until constant mass. The pre-carbonization process uses an oven at a temperature of 200 ℃ for 1 hour 30 minutes and the sample is ground using ball milling for 20 hours. The sample is sieved using a sieve with a size of 53 μm to standardize the particle size of the carbon powder. The chemical activation process uses 0.5 M $ZnCl_2$ activating agent. The manufacture of pellets from carbon powder uses a hydraulic press with a pressure of 7.5 tons and is held for 2 minutes. The carbonization process is carried out by heating the pellets in a furnace at a temperature of 600℃ using Nitrogen gas (N_2). The physical activation process uses Carbon dioxide gas (CO_2) with temperature variations of 700℃, 750℃, and 800℃. The carbon electrode is soaked using distilled water until the pH is neutral. The manufacture of supercapacitor cells is made using several components, namely carbon electrodes, current collectors, Teflon, separators (softies surgical masks 2nd layer), and electrolytes (H_2SO_4). Each sample will be subjected to density calculations and x-ray diffraction analysis, as well as electrochemical properties testing using the cyclic voltammetry method.

RESULTS AND DISCUSSION

Density Analysis

Figure 1 is a graph of the density reduction of carbon electrodes before and after the pyrolysis process. This decrease in density is caused by the carbonization and physical activation processes which have a role in removing elements other than carbon. The decrease in density obtained occurs because of the reaction of H_2O with carbon so that there will be a break in the carbon chain which forms new pores and carbon electrodes [6]. The resulting pores will determine the surface area of the carbon caused by carbon particles breaking into smaller parts than before [7]. After pyrolysis, the density value of the monolith in each sample experienced a decrease of 0.563, 0.511, and 0.585 g/cm^3 respectively with a density percentage of 32.8%, 40.43%, and 31.46%. SKM-700 has the lowest density compared to SKM-750 and SKM-800. Judging from the results of the density reduction, it can be concluded that the SKM-750 sample is the sample with the best heating, because the increase in density causes the porosity to decrease so that the specific capacitance value will also decrease [8].

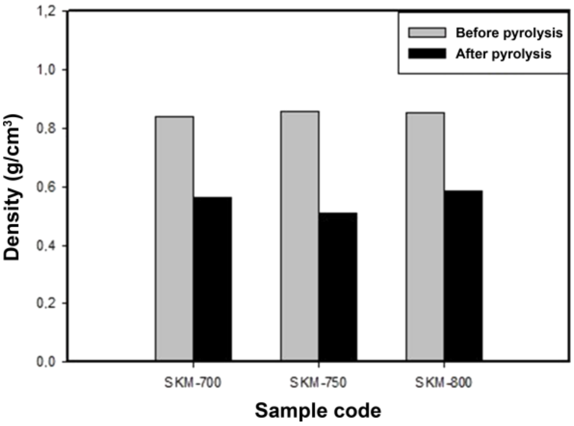

Figure 1. Carbon electrode density reduction.

X-ray Diffraction Data Analysis

The results of the X-ray diffraction pattern characterization show two peaks located on the hkl plane (002) and (100), where the 2θ angle on the scattering plane (002) and (100) on SKM-750 is 24.16º and 45.5º, while for SKM-800 it is 24.36º and 45.18º. The two gentle peaks mark the scattering angles that correspond to the amorphous structure of biomass-based carbon materials [9]. The sample with the largest high microcrystalline layer (L_c) is found in the SKM-750 sample with a physical activation temperature of 750ºC. The width of the microcrystalline layer (L_a) is inversely proportional to the height of the microcrystalline layer (L_c). The SKM-750 sample has the highest Lc value of 13.06 nm. Where a high L_c value indicates a large carbon surface [10]. It is concluded that the density and L_c value of the sample will affect the surface area [11]. The L_c/L_a ratio in each SKM-750 and SKM-800 sample is 0.9 and 0.8. This L_c/L_a ratio is related to the specific capacitance value that will be produced, because a high L_c/L_a ratio indicates a larger micropore volume, number of mesopores, and surface area so that the specific capacitance value will increase [12]. Table 1 shows that the SKM-750 sample has an N_p value of 3.55. This indicates that the microstructure of the sample has developed pores [13].

Table 1. Interplane distance and microcrystalline dimensions of carbon electrode.

Sample code	2θ		Interplane distance		Microcrystalline dimensions		L_c/L_a	N_P
	002	100	d_{002} (Å)	d_{100} (Å)	L_c (nm)	L_a (nm)		
SKM-750	24.16	45.5	3.68	1.99	13.06	14.46	0.9	3.55
SKM-800	24.36	45.18	3.65	2	11.61	14.46	0.8	3.18

Cyclic Voltammetry Analysis

Cyclic voltammetry test curves of SKM-700, SKM-750, and SKM-800 samples with a scan rate of 1 mV/s are shown in Figure 2. The CV curve on SKM-800 has the smallest area and the CV curve on SKM-750 has the largest area, this can affect the magnitude of the specific capacitance value in the supercapacitor cell. The wider the CV curve, the greater the charge-discharge current value, so the specific capacitance is high. The resulting CV curve also approaches the length size, where this shape is the ideal property of electrochemical double-layer supercapacitors (EDLC) [6].

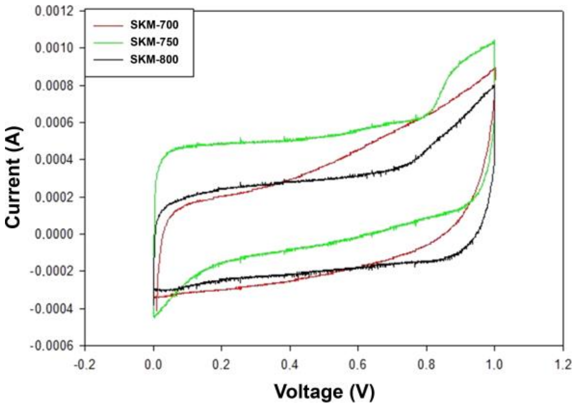

Figure 2. Cyclic voltammetry curve.

The specific capacitance value for each sample of SKM-700, SKM-750, and SKM-800 is 122.22, 145.45, and 95.93 F/g. This specific capacitance value is influenced by the physical activation temperature, where the higher the physical activation temperature, the faster the gasification reaction of volatile compounds, so that the carbon chain will be released and cause the pores formed to increase. However, if the physical activation temperature is too high as in the SKM-800 sample, it will affect the specific capacitance results. This happens because the temperature is too high will cause the carbon electrode structure to collapse, the inner wall channel becomes thinner and the adjacent pores will be interconnected. The high specific capacitance value in SKM-750 is due to having the lowest density value after the pyrolysis process of other samples. The low density value of the carbon electrode can increase the porosity which indicates the number of pores in the carbon electrode. The low physical activation temperature causes few pores to form in the carbon electrode. While the physical activation temperature that is too high damages the pore structure of the carbon electrode [14].

CONCLUSION

The results and discussion show that the temperature of 750°C is the optimum physical activation temperature for young coconut fiber samples. The temperature of 750°C is able to produce carbon electrodes with the highest density shrinkage percentage of 40.43%. The physical activation temperature of 750°C has high L_c, L_c/L_a, and N_p values so that it can increase the surface area of the carbon electrode. Analysis using cyclic voltammetry shows that the temperature of 750°C is able to produce a C_{sp} of 145.45 F/g.

REFERENCES

1. Miller, J. R. & Burke, A. (2008). Electrochemical capacitors: challenges and opportunities for real-world applications. *The Electrochemical Society Interface*, **17**(1), 53.
2. Samantara, A. K., Ratha, S., Samantara, A. K., & Ratha, S. (2018). Components of supercapacitor. *Materials Development for Active/Passive Components of a Supercapacitor: Background, Present Status and Future Perspective*, 11–39.
3. Awang, Y., Shaharom, A. S., Mohamad, R. B., & Selamat, A. (2009). Chemical and physical characteristics of cocopeat-based media mixtures and their effects on the growth and development of Celosia cristata. *American journal of agricultural and biological sciences*, **4**(1), 63–71.
4. Viju, N., Satheesh, S., & Vincent, S. G. P. (2013). Antibiofilm activity of coconut (Cocos nucifera Linn.) husk fibre extract. *Saudi Journal of Biological Sciences*, **20**(1), 85–91.
5. Paskawati, Y. A., & Retnoningtyas, E. S. (2017). Pemanfaatan sabut kelapa sebagai bahan baku pembuatan kertas komposit alternatif. *Widya Teknik*, **9**(1), 12–21.
6. Hanifa, Z., & Awitdrus, A. (2022). Pembuatan Elektroda Karbon dari Biomassa Sabut Kelapa Muda dengan Aktivator KOH Sebagai Aplikasi Sel Superkapasitor. *Indonesian Physics Communication*, **19**(1), 45–50.
7. Sudibandriyo, M. & Lydia, L. (2011). Karakteristik luas permukaan karbon aktif dari ampas tebu dengan aktivasi kimia. *Jurnal Teknik Kimia Indonesia*, **10**(3), 149–156.
8. Hartati, S. D., Taer, E., Sugianto, S., & Taslim, R. (2016). Pengaruh variasi suhu aktivasi fisika terhadap sifat fisis dan elektrokimia elektroda karbon superkapasitor dari limbah kulit pisang. *Spektra: Jurnal Fisika dan Aplikasinya*, **1**(2), 165–170.
9. Awitdrus, A., Hanifa, Z., Agustino, A., Taer, E., & Farma, R. (2022). Perbandingan larutan elektrolit H_2SO_4 dan KOH pada kinerja elektrokimia bahan elektroda berbasis karbon aktif sabut kelapa muda. *Indonesian Journal of Industrial Research*, **12**(1), 15–20.
10. Farma, R., Lestari, A. N. I., & Apriyani, I. (2021, October). Supercapacitor cell electrodes derived from nipah fruticans fruit coir biomass for energy storage applications using acidic and basic electrolytes. *Journal of Physics: Conference Series*, **2049**(1), 012043.
11. Miller, J. R. & Simon, P. (2008). Electrochemical capacitors for energy management. *Science*, **321**(5889), 651–652.
12. Farma, R., Deraman, M., Awitdrus, A., Talib, I. A., Taer, E., Basri, N. H., Manjunatha, J. G., Ishak, M. M., Dollah, B. N. M., & Hashmi, S. A. (2013). Preparation of highly porous binderless activated carbon electrodes from fibres of oil palm empty fruit bunches for application in supercapacitors. *Bioresource Technology*, **132**, 254–261.
13. Farma, R., Winalda, B., & Apriyani, I. (2023). The self-adhesive properties of carbon activated-like shape coin derived from Palmae plant waste and used as high-performance supercapacitor electrodes. *Journal of Electrochemical Energy Conversion and Storage*, **20**(2), 020902.
14. Simanjuntak, M. T., & Awitdrus, A. Fabrikasi elektroda karbon dari sabut kelapa muda dengan aktivasi fisika sebagai aplikasi superkapasitor. *Indonesian Physics Communication*, **19**(2), 65–68.

IPC
Indonesian Physics Communication
Department of Physics, Universitas Riau, Pekanbaru, Indonesia
p-ISSN 1412-2960 | e-ISSN 2579-521X
Vol. 21 | No. 3
November 2024
Web: https://kfi.ejournal.unri.ac.id
E-mail: kfi@ejournal.unri.ac.id

Interpretation of aquifer layers in peatland areas using the Wenner configuration geoelectric method in Rimba Panjang Village, Tambang District, Kampar Regency

Restu Firmansyah, Juandi Muhammad*
Department of Physics, Universitas Riau, Pekanbaru 28293, Indonesia

*Corresponding author: juandi@lecture.unri.ac.id

ABSTRACT

Geoelectric is a geophysical method used to determine the geological conditions of the earth's subsurface based on the variations of rock resistivity value. Interpretation of the aquifer layer is carried out on 2 paths with a length of 300 meters each. The lithology of the study area consists of layers of clay, peat, clay, sand, coarse sandstone, dry gravel, mudstone, limestone, tufan sand to siltstone. According to the data processing results, it shows that the aquifer in Rimba Panjang Village is at a depth ranging from (12.8 – 24.9) meters below ground level with medium groundwater potential. Interpretation using Res2Dinv Software as well as geological maps of the surrounding area informed the subsurface conditions and the presence of groundwater aquifers of the study area. It was found that the resistivity interval of trajectory 1 are (164.341) Ωm, (709 – 1477) Ωm, to (1477 – 3075) Ωm while of trajectory 2 are (864 – 1642) Ωm, (1642 – 3118) Ωm, to (3118 – 5921) Ωm. It can be concluded that the deeper the soil layer, the higher the moisture content. Because the deeper the soil layer, the lower the maturity of the peat, so that the soil is able to hold more water.

Keywords: Aquifer; geoelectrical method; peat; Res2Dinv; Wenner configuration

Received 18-09-2023 | Revised 17-10-2023 | Accepted 04-11-2024 | Published 30-11-2024

INTRODUCTION

Water is a component that moves actively continuously through the surface and also through the lower part of the earth's surface [1-3]. Water has a very important role in human life, all living things certainly need the availability of water, the availability of water on the face of the earth is very limited, both in terms of quality and quantity [4-6].

Groundwater is one of the components of the flow of water on earth which is called the hydrological cycle where water is often used in the survival of all living things after going through the process of evaporation (precipitation) from the sea, lakes, or rivers, then condensation occurs in the atmosphere, and then becomes rain that falls to the earth's surface. The rainwater that falls on the earth's surface moves through the earth's surface (run off) and some enters below the earth's surface (infiltration) [7].

The soil structure of a place depends on geological and climatic conditions. This event affects the condition of the soil layer structure in various regions. The type of rock layer passed by groundwater is obtained by finding the resistivity value of a material formation below the ground surface. The conditions of inundated, flooded and non-inundated areas have different depths depending on the thickness of the layer and the presence of aquifers [8].

Aquifers are permeable underground layers that contain water, rocks, fractures, and materials that are not united. Geoelectric measurements aim to further explore the concept of physics in the earth's layers including the method of subsurface resistivity, to determine the distribution of resistivity in the aquifers that make up the subsurface layer and to interpret the measurement data obtained. The method used in this study is the geoelectric method with Wenner's rules. Physical

| DOI: 10.31258/jkfi.21.3.265-270

parameters that can provide an overview of water quality are resistivity, conductivity, and salinity [9].

The presence of groundwater is known by identifying the composition of rocks from the earth's subsurface structure referring to differences in resistivity values using geoelectric exploration [10].

Previous research has been conducted by Nuryanti 2020 on the determination of low aquifers using the Wenner rule geoelectric method and hydrogeochemistry in Rimba Panjang Village, the results of the study based on data analysis stated that the aquifer is at a depth of less than 8 meters below the ground surface with a resistivity interval ranging from (89.2-1023.9) Ωm. The groundwater layer obtained from the processing of data from trajectories 1 and 2 shows the distribution of groundwater [11].

The use of the Wenner method is expected to be a step in horizontal land mapping and its nature is spread so that it can provide a cross-section of the distribution of groundwater and aquifers in the peat area of Rimba Panjang Village, namely the Gean de Green II housing.

LITERATURE REVIEW

Water sources, namely surface water and groundwater, must be managed sustainably to avoid further water scarcity [12].

Sustainable groundwater exploitation must be based on an understanding of the geology and hydrological conditions of the aquifer, because the productivity of aquifers in various regions is highly dependent on the subsurface soil layer [13]. Groundwater is found in permeable geological structures called aquifers, which are water-holding structures that allow large amounts of water to pass through. Groundwater is also found in aquicludes (semi-permeable bases) structures that contain water but cannot move it quickly enough to replenish large supplies of wells or springs of sand and gravel, alluvium, and glacial deposits.

Sandy estuarine deposits are excellent sources of water [14, 15]. Rock resistivity is the ability of a material or rock to block the flow of electric current in a medium. The resistivity value of rocks is inversely proportional to conductivity.

The relationship between soil resistivity and soil conductivity can be written in the form of an equation:

$$\rho = \frac{1}{\sigma} \tag{1}$$

Table 1. Rock resistivity values [16].

Material	Resistivity (Ωm)
Air	-
Phyrite	0.01 – 100
Quartz	500 – 80000
Calcite	$1 \times 10^{12} – 1 \times 10^{13}$
Rock salt	$30 – 1 \times 10^{13}$
Granite	200 – 10000
Andesite	$1.7 \times 10^{2} – 45 \times 10^{4}$
Basalt	200 – 10000
Limestone	500 – 10000
Sandstone	200 – 8000
Shales	20 – 2000
Sand	1 – 1000
Clay	1 – 100
Ground water	0.5 – 300
Magnetite	0.01 – 1000
Dry gravel	600 – 10000
Alluvium	10 – 800
Gravel	10 – 600

RESEARCH METHODS

The geoelectric method has been reported to have a high level of sensitivity for groundwater exploration [17]. In addition, the efficiency of the geoelectric resistivity method is able to map the subsurface layer providing more precise important information to characterize the aquifer layer, describe the depth of the bedrock, and determine resistivity values [18]. By estimating the resistivity price, rock porosity, and soil hydraulic conductivity, groundwater can be estimated qualitatively.

The Wenner configuration can provide a resistivity distribution map in the form of a two-dimensional subsurface image. The distance between the current electrode is three times the distance of the potential electrode, the potential distance to the sounding point is a/2, so the distance between the current electrode and the sounding point is 3a/2. The target depth that can be achieved is a/2 [16].

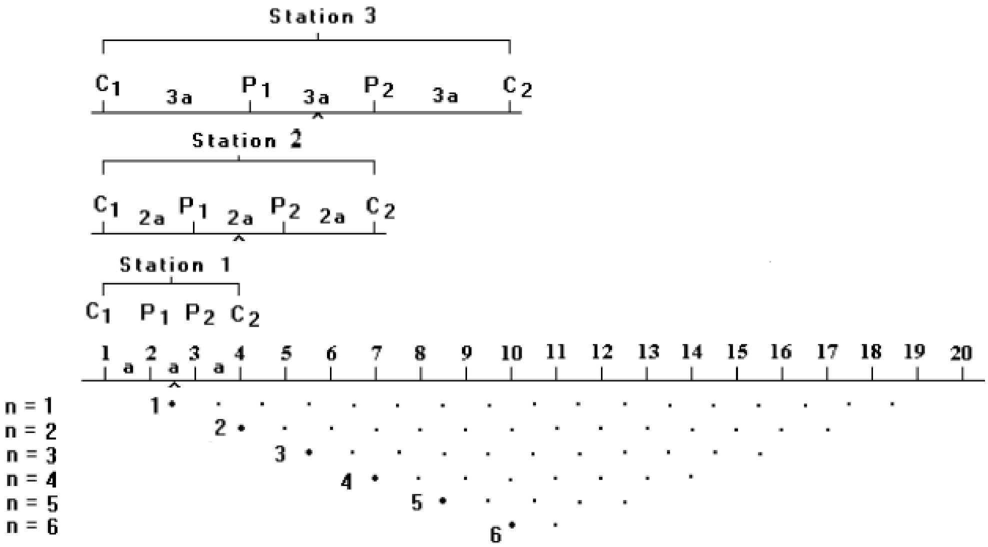

Figure 1. How to measure the Wenner configuration

RESULTS AND DISCUSSION

Data analysis and interpretation results based on field measurements using 2 tracks, each 300 meters long. Data collection in the field using the Wenner configuration geoelectric method at Gean de Green II Housing, Rimba Panjang Village, Tambang District, Kampar Regency. Field measurement data on track 1 were converted into apparent resistivity and 2D cross-section inversion results using Res2Dinv Software.

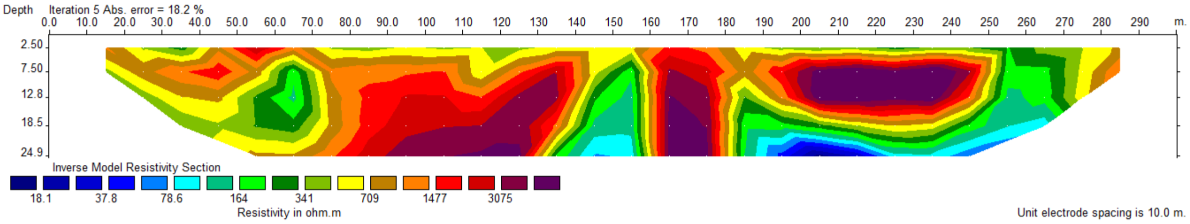

Figure 2. 2D cross-section inversion results for track 1.

Figure 2 above displays various layers with certain resistivity values according to the material in them. The results of calculations and data processing on track 1 with Res2Dinv Software using the Wenner method obtained an RMS-error value of 18.2% with a resistivity interval of (18.1 – 3075) Ωm and the depth of the layer displayed reached 24.9 meters. The results of the calculation and data processing on track 2 with Res2Dinv Software obtained an RMS-error value of 21.0% with a readable depth of 24.9 meters.

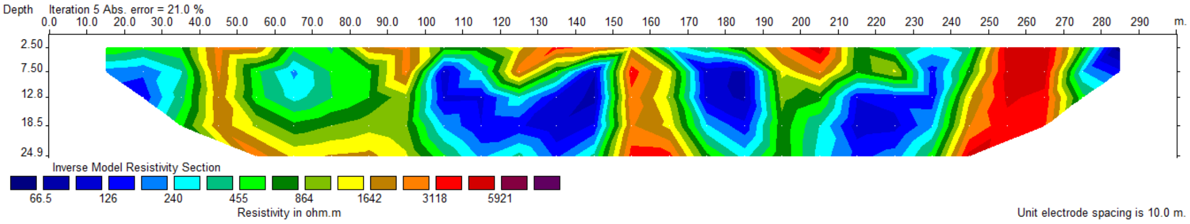

Figure 3. Results of 2D cross-section inversion of track 2.

The results of the 2D cross-section inversion of track 2 are shown in Figure 3 above with a resistivity interval ranging from (66.5 – 5921) Ωm. From the data processing carried out, it shows that the aquifer is located at a depth of 2.50 – 24.9 meters. Interpretation of track 1 on L1 with a depth of 2.5 – 12.8 meters is interpreted as shallow peat containing clay composition with a resistivity value ranging from (18.1 – 78.6) Ωm. L2 is light green in color and is suspected to be calcareous mudstone, with a resistivity value of (78.6 – 164) Ωm at a depth of 12.8 – 18.5 meters. L3 is dark green with a resistivity value of (164 – 341) Ωm is suspected to be a formation of coarse ash sandstone with a little clay at a depth of 24.9 meters. L4 is interpreted as the presence of claystone and sand at a depth of 7.50 – 18.5 meters with a resistivity value of (341 – 709) Ωm. L5 is brown to red in color, there is a composition of limestone, silt, and dry gravel at a depth of 15 meters with a resistivity value of (709 – 1477) Ωm. L6 is red to purple in color is suspected to be dry gravel material, and a little siltstone with a resistivity value of (1477 – 3075) Ωm at a depth of 24.9 meters.

Table 2. Results of L1 data processing.

Depth (m)	Resistivity (Ωm)	Material composition	Type of layer
2.5	66.5 – 240	Clay and tuffaceous sand	Aquitard
7.5	240 – 864	Claystone	Aquiclude
12.8	864 – 1642	Dra gravel	Aquifer
18.5	1642 – 3118	Dry gravel and sandstone	Aquifer
24.9	3118 – 5921	Dry gravel, limestone, and sandstone	Aquifer

The results of the path interpretation indicate that the potential aquifer is in a shallow area close to the surface at varying depths (see Tables 2 and 3). L1 with a depth of 2.5 meters is a medium peat layer containing fresh groundwater marked by dark blue to light blue with a resistivity value of (66.5 – 240) Ωm. L2 is green to turquoise with a resistivity value of (240 – 864) Ωm interpreted as a layer containing claystone at a depth of 7.50 meters.

Table 3. Results of L2 data processing.

Depth (m)	Resistivity (Ωm)	Material composition	Type of layer
2.5	66.5 – 240	Clay and tuffaceous sand	Aquitard
7.5	240 – 864	Claystone	Aquiclude
12.8	864 – 1642	Dra gravel	Aquifer
18.5	1642 – 3118	Dry gravel and sandstone	Aquifer
24.9	3118 – 5921	Dry gravel, limestone, and sandstone	Aquifer

L3 is a layer of clay, silt, and a little dry gravel found at a depth of 12.8 meters with a resistivity value of (864 – 1642) Ωm marked by a yellow to brown color. L4 is suspected of containing dry gravel and glauconite sandstone formations with a resistivity of (1642 – 3118) Ωm at a depth of 18.5 meters, marked by a brown to red color. The L5 assumption shows the presence of dry gravel, limestone and sandstone formations. Figures 2 and 3 show various layers with certain resistivity values based on the material or rocks below the peat soil surface as a geoelectric research site.

CONCLUSION

Based on the results of resistivity measurements, it is interpreted that for path 1 the resistivity value of the soil layer ranges from (18.1 – 3075) Ωm with a maximum depth of 24.9 meters, path 2 obtained a resistivity value of the soil layer ranging from (66.5 - 5921) Ωm with a maximum depth of 41.06 meters. Interpretation of lithology below the ground surface of Gean de Green II Housing, namely peat, clay, sandstone, limestone, dry gravel, saturated gravel, sandy clay, and sand.

The existence of aquifers refers to the formation of the geological sheet map and based on the results of data processing and 2D geoelectric cross-sectional images of the Wenner configuration, it is interpreted that on path 1 it was found at a depth of 15 meters, 24.9 meters and > 24.9 meters with a lithology composition of limestone, dry gravel, coarse sandstone, and siltstone. Route 2 found aquifer layers at depths of 12.8 meters, 18.5 meters and 24.9 meters with lithological compositions, namely dry gravel, sandstone and limestone which are very good at transmitting water.

REFERENCES

1. Juandi, M. & Ginting, E. N. (2021, October). The groundwater analysis using geoelectric method Wenner rules in Rejosari Village, Tenayan Raya Pekanbaru. *Journal of Physics: Conference Series*, **2049**(1), 012064.
2. Handwerger, A. L., Booth, A. M., Huang, M. H., & Fielding, E. J. (2021). Inferring the subsurface geometry and strength of slow-moving landslides using 3-D velocity measurements from the NASA/JPL UAVSAR. *Journal of Geophysical Research: Earth Surface*, **126**(3), e2020JF005898.
3. Singha, K., & Navarre-Sitchler, A. (2022). The importance of groundwater in critical zone science. *Groundwater*, **60**(1), 27–34.
4. Juandi, M. & Santoso, S. A. (2021). Analysis of groundwater infiltration using the schlumberger geoelectric method. *Journal of Physics: Conference Series*, **2049**(1), 012070.
5. Young, S. L., Frongillo, E. A., Jamaluddine, Z., Melgar-Quiñonez, H., Pérez-Escamilla, R., Ringler, C., & Rosinger, A. Y. (2021). Perspective: the importance of water security for ensuring food security, good nutrition, and well-being. *Advances in nutrition*, **12**(4), 1058–1073.
6. Sarker, B., Keya, K. N., Mahir, F. I., Nahiun, K. M., Shahida, S., & Khan, R. A. (2021). Surface and ground water pollution: causes and effects of urbanization and industrialization in South Asia. *Scientific Review*, **7**(3), 32–41.
7. Octalizar, M. R. (2021). Penentuan lapisan dan akuifer dengan kualitasnya menggunakan metode geolistrik dan geokimia konfigurasi Wenner di Desa Tarai Bangun Kecamatan Tambang Kabupaten Kampar. *FMIPA Universitas Riau*.
8. Enggarwati, D. A., Susilo, A., & Wardhana, D. D. (2015). Pendugaan akuifer serta pola alirannya dengan metode geolistrik daerah Pondok Pesantren Gontor 11 Solok–Sumatera Barat. *Physics Student Journal*. **2**(1), 549– 553.
9. Juandi, M. (2018). The interpretation of underground water physical parameters of housing in the region of asahan indah palm oil factory area Rokan Hulu District. *Open Journal of Modern Hydrology*, **8**(4), 119–125.
10. Wijaya, A. S. (2015). Aplikasi metode geolistrik resistivitas konfigurasi Wenner untuk menentukan struktur tanah di halaman belakang SCC ITS Surabaya. *Jurnal Fisika Indonesia*, **19**(55), 1–5.
11. Nuryanti, N. (2020). Identifikasi akuifer dangkal dengan menggunakan metode geolistrik konfigurasi Wenner dan hidrogeokimia di Desa Rimba Panjang. *FMIPA Universitas Riau*.
12. Juandi, M. (2017). Sustainability model for unconfined aquifers. *International Journal of Science and Applied Technology*, **1**(1).
13. Juandi, M. & Syahril, S. (2017). Empirical relationship between soil permeability and resistivity, and its application for determining the groundwater gross recharge in Marpoyan Damai, Pekanbaru, Indonesia. *Water Practice and Technology*, **12**(3), 660–666.
14. Vila-Concejo, A., Gallop, S. L., & Largier, J. L. (2020). Sandy beaches in estuaries and bays. *Sandy beach morphodynamics*, 343–362.

15. Driscoll, F. G. (1987). Groundwater and Wells, Johnson Division, second printing, St. *Paul, MN*.
16. Telford, W. M., Geldart, L. P., & Sheriff, R. E. (1990). *Applied geophysics*. Cambridge university press.
17. Lenkey, L., Hámori, Z., & Mihálffy, P. (2005). Investigating the hydrogeology of a water-supply area using direct-current vertical electrical soundings. *Geophysics*, **70**(4), 11–19.
18. Sultan, S. A. & Santos, F. A. M. (2008). Evaluating subsurface structures and stratigraphic units using 2D electrical and magnetic data at the area north Greater Cairo, Egypt. *International Journal of Applied Earth Observation and Geoinformation*, **10**(1), 56–67.

Indonesian Physics Communication
Department of Physics, Universitas Riau, Pekanbaru, Indonesia
p-ISSN 1412-2960 | e-ISSN 2579-521X
Vol. 21 | No. 3
November 2024
Web: https://kfi.ejournal.unri.ac.id
E-mail: kfi@ejournal.unri.ac.id

The effect of water content on increasing grammage in paper made from water hyacinth and cassava peel

Jati Nur Sariah*, Ety Jumiati, Ridwan Yusuf Lubis
Department of Physics, Universitas Islam Negeri Sumatera Utara, Deli Serdang 20371, Indonesia

*Corresponding author: jatinursariah@gmail.com

ABSTRACT

Paper is a thin sheet-shaped material containing cellulose from wood. The high demand for paper makes the raw material for paper production increase, which causes forest exploitation. As for this study to determine the effect of mixed variationsin the mixture made from ater hyacinth and cassava peel with the adition of NaOH solution, the characteristics of the paper produced, and the optimal paper quality. Variations in the percentage of water hyacinth and cassava skin raw materials, namely: sample A 30% : 70%, sample B 50% : 50%, and sampel C 70% : 30%. Using the experimental method is done with the soda process. The characterization tests carried out were grammage and water content. The results of the characteristictest obtained grammage values in sample A = 51.6 g/m^2, sample B = 84.0 g/m^2, sample C = 97.0 g/m^2. Test the water content in sample A = 5.7%, sample B = 5.9%, and sample C = 6.1%. Has met the value of SNI 7274-2008 for printing type A paper.

Keywords: Cassava peel; paper; water hyacinth

Received 31-10-2023 | Revised 14-11-2023 | Accepted 16-11-2024 | Published 30-11-2024

INTRODUCTION

In Indonesia, paper usage increases every year, causing the use of wood as a raw material for paper making to also increase [1]. Almost 90% of the raw material for paper making is still dominated by wood, which causes the possibility of forest exploitation. Excessive exploitation of wood can damage the ecosystem and environment [2].

Global paper consumption is currently 394 million tons and is predicted to increase to 490 million tons by 2020. However, domestic paper usage is very high compared to other countries. So it has the potential for high forest damage. In addition, the available wood will be increasingly scarce, and forest damage will be even worse. By substituting other potential materials besides wood, efforts are being made to reduce its use as a raw material for pulp and paper [3].

Seeing the increasing demand for paper, alternative materials are needed to be used as the main raw material for paper making, so that the use of wood in paper making can be reduced. One of them is water hyacinth and cassava skin, which until now have not been widely used. Water hyacinth is usually processed by the community into raw materials for seedlings, mulch, fertilizer, and paper.

LITERATURE REVIEW

Paper

Paper comes from organic materials containing cellulose [4]. Glucose and β-1-4-glucan bonds form a straight chain polysaccharide polymer known as cellulose. Inside the cellulose there are fibers that have high tensile strength, are insoluble in organic solvents and water [5]. The cellulose content in making paper pulp greatly affects the quality of the paper, if the cellulose content is below 40%, the resulting paper is not good.

Water Hyacinth

Water hyacinth (*Eichhornia crassipes*) is a plant that grows in the air floating, has thick

©Author(s) | DOI: 10.31258/jkfi.21.3.271-274

and bubbly leaves [6]. Both vegetatively and generatively, water hyacinth grows very quickly. Water hyacinth is used by researchers as the main ingredient in making paper, because it has a lot of cellulose content, which is the main requirement for making paper.

Cassava Peel

Cassava peel can also be used in making paper because it has cellulose fibers, which is the main requirement in making paper. Cassava (*Manihot esculenta*) is a plant with a fairly high starch content. can be processed into semi-finished products such as tapioca flour or used as a substitute for staple foods. Apart from the tubers, cassava skin dregs can also be used as raw materials for making paper. Some people only use cassava skin as animal feed. The use of cassava in Indonesia is 19.9 million tons per year. Where cassava skin reaches 0.04 – 0.09 million tons per year [7].

Water hyacinth and cassava skin can be used as pulp in making paper. The method of making pulp in general through the stages, pulp making, defibration, washing, filtering, bleaching (bleaching), and printing. Pulping is the process of reducing the size of raw materials containing fibers such as wood or other materials into a mass of fiber. Because the fibers are tightly bound together, long-fiber pulp paper has high tensile strength. Conversely, long fibers are unable to fill small pores, because the pores will be filled with short-fiber pulp [8]. In paper making, it is necessary to add adhesive to obtain good paper quality such as the desired color, fiber quality and texture, as well as the physical quantity of the paper such as good grammage and tensile strength [9, 10].

RESEARCH METHODS

The technique used in the study is an experimental method, carried out with a soda process using 2.5% NaOH solution. In the heating process using 2.5% NaOH to remove lignin in water hyacinth and cassava skin. The three-dimensional polymer network known as lignin functions to glue cellulose fibers together to make them stiff. H_2O is used as a bleach (bleach), Na_2SO_3 is used as a softener of raw materials, Acetic acid is used as a solvent of raw materials.

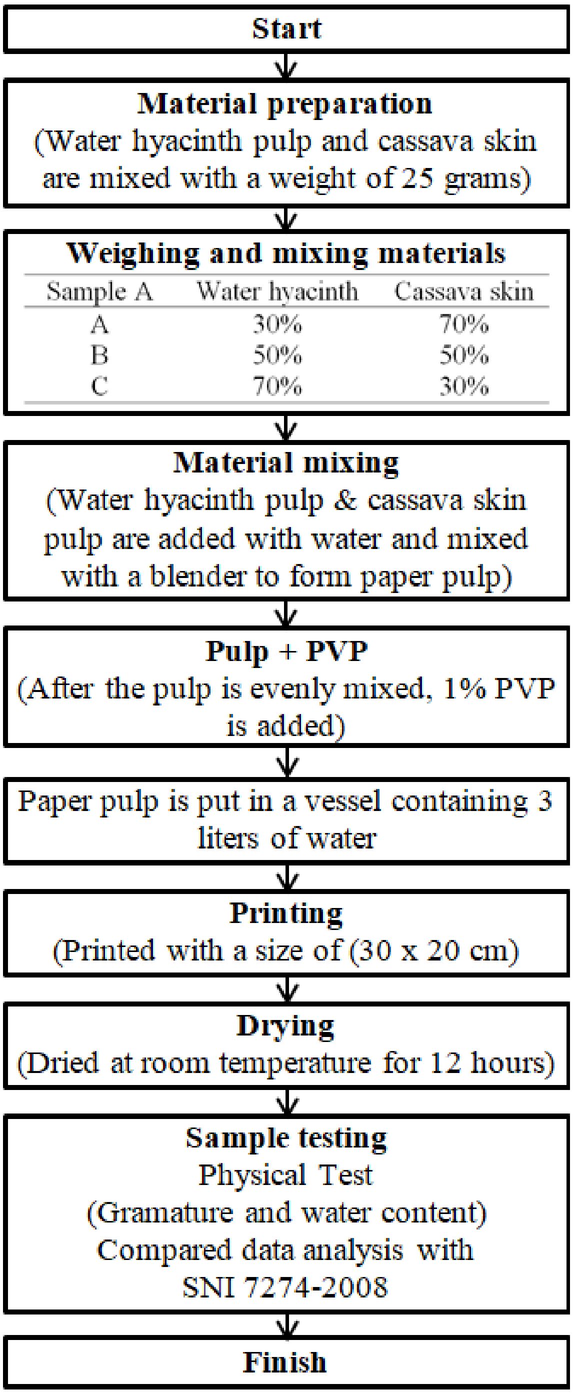

Sample A	Water hyacinth	Cassava skin
A	30%	70%
B	50%	50%
C	70%	30%

Figure 1. Stages of making and testing paper from water hyacinth and cassava skin raw materials.

The tools used in this study were oven, tripod, magnetic hotplate, analytical balance, stand & clamp, magnetic stirrer, blender, 1000 ml beaker, porcelain cup, stirring rod, thermometer, sieve, plastic, vessel, paper mold, ruler, and scissors. The diagram of this research can be seen in Figure 1.

The raw materials in this study were water hyacinth taken in the Medan Tuntungan area of North Sumatra, cassava skin taken in the Medan Tuntungan area of North Sumatra, 2.5% NaOH, 5.25% H_2O_2, 2% Na_2SO_4, 10% acetic acid, pinovinylpyrrolidone, water, distilled water. In addition, the composition of water hyacinth and cassava skin was varied with different mixtures as in Table 1.

Table 1. Variations in the mixture of raw materials for making paper.

Sample	Water hyacinth	Cassava skin
A	30%	70%
B	50%	50%
C	70%	30%

RESULTS AND DISCUSSION

Grammage

Conducted to determine the mass of paper from a certain unit area. Based on Table 2, the highest paper grammage value in sample C is 97.0 g/m^2, in sample B is 84.0 g/m^2, and sample A is 51.6 g/m^2. As the sample can be seen in Table 2, the paper grammage tends to increase in proportion to the composition of water hyacinth and cassava peel materials and has met SNI standards.

Table 2. Paper grammage measurement.

Sample	Grammage (g/m^2)	SNI 7274-2008 (g/m^2)
A	51.6	50 – 100
B	84.0	
C	97.0	

Based on Figure 2, it shows that grammage increases with the comparison of materials, sample A (30% water hyacinth : 70% cassava peel), B (50% water hyacinth : 50% cassava peel), and sample C (70% water hyacinth : 30% cassava peel). the highest value in sample C. this is influenced by the increasing percentage of water hyacinth. Because water hyacinth has a higher water content and has longer fibers compared to cassava peel.

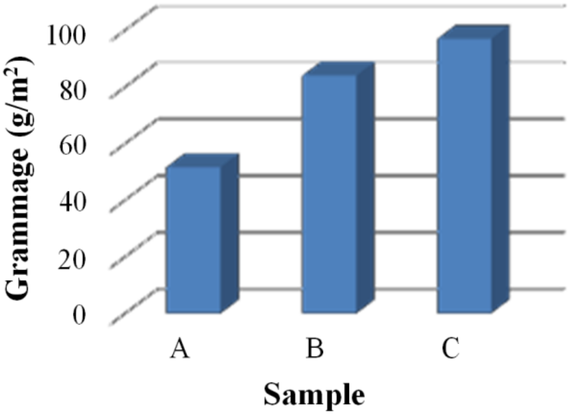

Figure 2. Paper grammage measurement chart.

Water Content

Conducted to determine the water content of a paper. Based on Table 3, the air content value in sample A is 5.7%, in sample B is 5.9%, and in sample C is 6.1% from the three samples above, the lowest air content value is obtained in sample A.

Table 3. Measurement of paper water content.

Sample	Water content (%)	SNI 7274-2008 (%)
A	5.7	< 6
B	5.9	
C	6.1	

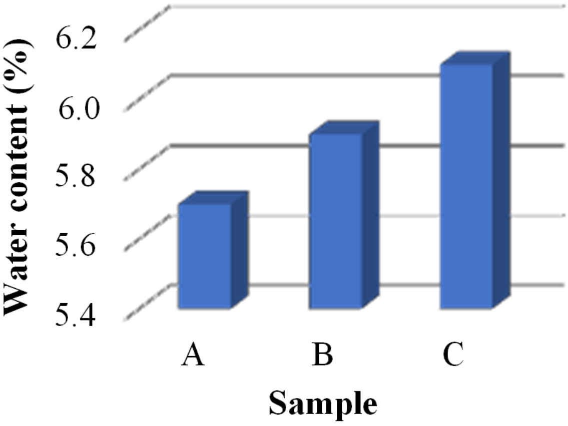

Figure 3. Paper water content measurement.

Based on Figure 3, it shows that the air content increases with the comparison of materials, the sample that shows the most optimal value in sample A, namely the sample that has the lowest air content. This is due to the increasing percentage of water hyacinth, because the water hyacinth content is more than cassava skin.

CONCLUSION

The conclusion drawn from the results of this study is that the grammage value of sample A is 51.6 g/m^2, sample B is 84.0 g/m^2, and sample C is 97.0 g/m^2. The water content test value of sample A is 5.7%, sample B is 5.9%, and sample C is 6.1%. If the grammage value is high, it will affect the water content value which will also increase because water hyacinth has a higher water content than cassava skin. The grammage and water content values have met the quality requirements of type A printing paper (SNI 7274-2008).

REFERENCES

1. Apriani, E. & Malik, J. A. (2019). Pembuatan kertas daur ulang dari limbah serat kelapa muda dan kertas bekas *Prosiding Konferensi Nasional Engineering Perhotelan X*, 242–247.
2. Fenny, F. O. & Farma, W. (2016). Pengaruh rasio berat kulit pisang dengan kertas koran dan batang jagung dengan kertas koran terhadap indeks tarik dan indeks sobek kertas recycle. *Prosiding Semnastek.*
3. Kurniawan, H., Garchia, C. H., & Ayucitra, A. (2017). Pemanfaatan kulit buah matoa sebagai kertas serat campuran melalui proses pretreatment dengan bantuan gelombang mikro dan ultrasonik. *Widya Teknik*, **16**(1), 1–10.
4. Kurniawan, M. A., Ramanda, G. D., Cantikasari, T., & Van Leun, S. G. (2019). Pembuatan kertas dari limbah pohon ketapang dengan metode delignifikasi. *Khazanah: Jurnal Mahasiswa*, **11**(1).
5. Nata, I. F., Niawati, H., & Muizliana, C. (2013). Pemanfaatan serat selulosa eceng gondok (*Eichhornia crassipes*) sebagai bahan baku pembuatan kertas: isolasi dan karakterisasi. *Konversi*, **2**(2), 9-16.
6. Rahmadi, A. I., Madusari, S., & Lestari, I. (2018). Uji sifat fisik dan sifat kimia pulp dari limbah pelepah kelapa sawit (*Elaeis guineensis Jacq.*). *Prosiding Semnastek.*
7. Ristianingsih, Y., Angraeni, N., & Fitriani, A. (2017). Proses pembuatan kertas dari kombinasi limbah ampas tebu dan sekam padi dengan proses soda. *Chempublish Journal*, **2**(2), 21–32.
8. Rosmainar, L. (2017). Analisis Bahan-Bahan Alternatif Pengolahan dalam Pembuatan Kertas. *Jurnal Inkofar (Online)*, **1**(2).
9. Hasibuan, A., Hasani, A. P. P., Nasution, N., & Hasibuan, S. M. (2023). Pemanfaatan tanaman eceng gondok (*Eichornia crassipes*) untuk kerajinan tas. *Cross-border*, **6**(2), 1091–1097.
10. Widyastuti, P. (2019). Pengolahan limbah kulit singkong sebagai bahan bakar bioetanol melaui proses fermentasi. *Jurnal Kompetensi Teknik*, **11**(1), 41–46.

Indonesian Physics Communication
Department of Physics, Universitas Riau, Pekanbaru, Indonesia
p-ISSN 1412-2960 | e-ISSN 2579-521X
Vol. 21 | No. 3
November 2024
Web: https://kfi.ejournal.unri.ac.id
E-mail: kfi@ejournal.unri.ac.id

Physical characteristics of water paint with the addition of bintaro extract additives

Romi Fadli Syahputra*, Surya Wulandari, Delovita Ginting
Department of Physics, Universitas Muhammadiyah Riau, Pekanbaru 28294, Indonesia

*Corresponding author: romifadli@umri.ac.id

ABSTRACT

The addition of additives to paint aims to improve the quality and usability of paint. Natural additives, such as bintaro seed extract, have potential as anti-bacterial and anti-fungal agents. This study aims to investigate the physical properties of commercial paints added with bintaro seed extract. The physical properties tested were changes in density and adhesion. While the chemical content was characterized using HPLC and FTIR. The extraction process includes drying to grinding the bintaro seeds into powder, followed by extraction using a ratio of bintaro powder and 96% (m/v) ethanol 1:3. Bitaro extract obtained was added to commercial watercolors (100 ml) with variations of 5, 10 and 15 ml. The paint is applied to the surface of the multiplex wood evenly by pre-heating it at 40°C. The adhesion analysis was carried out using the help of ImageJ software to determine the ratio of the gray value of the image before and after the adhesion test using the cross-cut technique. It was observed that the increase in bintaro seed extract caused a decrease in paint adhesion.

Keywords: Adhesive; bintaro seed extract; density; paint

Received 01-08-2023 | Revised 19-10-2024 | Accepted 06-11-2024 | Published 30-11-2024

INTRODUCTION

Paint is generally defined as a colloidal dispersion of pigments in solvents [1]. So the properties of paint are highly dependent on the particle size and surface of the pigment. Paint dispersion is the process of wetting and releasing the main pigment particles to spread them into the application media [2].

Bintaro fruit has the Latin name *Cerbera manghas* which has secondary metabolite compounds such as alkaloids, saponins, flavonoids, and tannins [3]. Alkaloid compounds in the form of berberine are found in almost all parts of the bintaro plant which play a role in the mortality of bintaro insects which play a role in insect mortality [4].

The way cerberin works is by disrupting the function of calcium ion channels in the heart of insects and eventually causing death [5]. Bintaro fruit extract has been proven to have the potential as a botanical insecticide. The level of cerberin depends on the level of ripeness of the bintaro fruit. Fruit whose skin color is more than 50% red has a high cerberin content, while unripe fruit contains low cerberine. When the ripeness of the bintaro fruit is even, the antibacterial content is at its maximum [6].

Bintaro fruit consists of 14% shell and 86% seed flesh. Bintaro seeds contain oil between 35% – 50%. The drier the bintaro seeds, the more oil they contain. This oil is a type of non-edible oil. Bintaro plants have many benefits even though Bintaro plants have dangerous cerberin poison [7]. The purpose of this study was to fabricate paint that can prevent termite attacks. Physical testing includes density testing and reactive power testing. High pressure liquid chromatography (HPLC) testing to quantitatively identify the chemical compound content in bintaro seed extract. Fourier transform infrared spectroscopy (FTIR) testing is used to identify functional compound groups contained in a compound [8].

©Author(s) | DOI: 10.31258/jkfi.21.3.275-280

LITERATURE REVIEW

Paint is defined as a liquid used to coat the surface of a material with the aim of beautifying, strengthening, or protecting the material. After being coated on the surface and drying, the paint will form a thin layer that adheres firmly to the surface [1].

Bintaro has various secondary metabolite contents that function as self-defense against pests and insects. Almost all parts of the bintaro plant contain a poison called "cerberin", a poison that can inhibit human calcium ion channels, thereby disrupting the heartbeat and can cause death. In addition, smoke from burning wood can cause poisoning [4].

Bintaro is known as one of the perennial plants that is widely used for greening, city decoration, organic pesticides and also as a raw material for dried flower crafts. All parts of the bintaro plant are poisonous because they contain alkaloid compounds that are repellent and antefeedant. Bintaro contains the poison cerberin which is very deadly. The leaves, fruit, and bark of the bintaro plant contain saponins, the leaves and fruit contain polyphenols which are known to be very toxic to insects and can inhibit pest feeding activities, and the bark contains tannins. Behind its poison, the bintaro tree can be used for human benefit, such as eradicating rats, raw materials for candles, bio-insecticides, wound medicine, deodorants and potentially as biodiesel [16]. The bintaro tree is 4 to 20 meters tall. This plant grows abundantly in the lowlands to the coast and is very suitable for sandy areas. Bintaro leaves are oval-shaped, elongated, symmetrical, and stacked at the ends, shiny dark green in color with varying lengths averaging 27 cm with a spiral leaf arrangement and collected at the end of the rosette.

RESEARCH METHODS

Seed Sample Preparation

The type of bintaro used is *Cerbera manghas*. Bintaro was collected from several parks in Pekanbaru City. The seeds used are from the bintaro fruit. Seed preparation includes several stages as follows: Separating the seeds from their shells, After the seeds are separated, the shells are washed and dried in the sun for ± 7 days. The dried seeds are then ground using a blender. The bintaro seed powder is sieved using a T100 mesh sieve.

The Process of Making Bintaro Seed Extract

The extract is made by macerating the bintaro seeds that have been ground using a blender then weighed as much as 100 grams and mixed with 300 ml of distilled water, left for ± 24 hours and a closed container to remove the substances in the bintaro seed powder [9]. The soaked powder is heated using a temperature of 60°C for ± 1 hour after being filtered using filter paper and then centrifuged for 20 minutes [10].

Extract and Paint Mixing Process

Watercolor mixing is done by first measuring the paint and bintaro seed extract using a measuring cup. Put the paint and bintaro seed extract into one container then stir using a stirring rod until both are mixed. This study uses 2 variables, the independent variable of bintaro seed extract and the dependent variable of paint. Bintaro seed extract as much as 5, 10, and 15 ml were mixed each in 100 ml of paint as summarized in Table 1.

Table 1. Variation of paint and extract mixtures.

Sample	Extract (ml)	Paint (ml)	Description
CEB-0	0	100	Control
CEB-1	5	100	Constant
CEB-2	10	100	Constant
CEB-3	15	100	Mixture

Characterization and Testing

HPLC Test

HPLC testing was carried out in the chemistry laboratory of Riau University by sending a sample of 10 ml. HPLC testing quantitatively identifies the content of alkaloids, saponins, flavonoids, and tannins [11].

FTIR Test

FTIR testing was carried out in the chemistry laboratory of Riau University by sending samples to identify functional compound groups contained in a compound. Testing was carried out with the ASTM E1252 standard 2013.

Density

Density (or density, is the mass (m) per unit volume (V). Things that affect the density measurement of a sample are temperature and pressure. Mathematically, density measurement can be found using Equation (1) [12].

$$\rho = \frac{m}{V} \tag{1}$$

Adhesion Test

Adhesion is measured using a cross cut system. This test is relatively simple by making a number of (6 – 11 lines) cross line boxes to the surface of the paint according to the ASTM D3359 standard. Furthermore, the tape is attached to the prepared paint surface and pulled quickly to the side [13]. Image capture using a smartphone camera with 16MP+5MP autofocus camera specifications and f/1.7 Aperture with a distance between the camera and sample of ~28 cm. The image capture scheme can be seen in Figure 1.

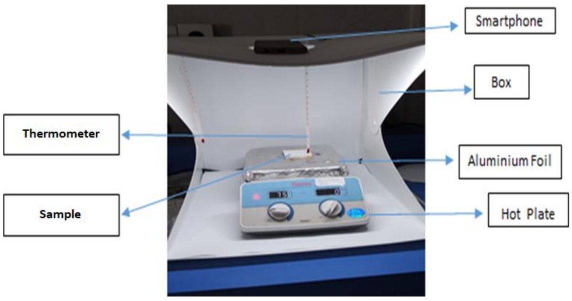

Figure 1. Image capture scheme.

Image analysis is carried out with the help of ImageJ software to obtain adhesion data. The ratio of the gray value of the image before and after the adhesion test using tape is represented as paint adhesion.

RESULTS AND DISCUSSION

Results

The maceration process is a fairly simple extraction process or method without a heating system or known as cold extraction [14]. So in this process the sample and solvent do not undergo a heating process so that they can be used on compounds that are not heat resistant. The disadvantage of this method is that it takes quite a long time. The maceration process on bintaro seeds is carried out by soaking approximately 1 gram of powdered sample in aquades solvent for 24 hours at room temperature [10]. Previously, the dry and cut seeds will be ovened for 6 hours to make it easier during the blending process to produce powder [7]. In the soaking process, plant samples will experience the breakdown of cell walls and membranes due to the difference in pressure between inside and outside the cell. Furthermore, maceration is carried out using heating at a temperature of 60°C because excessive heating can damage the chemicals contained in the powder [10].

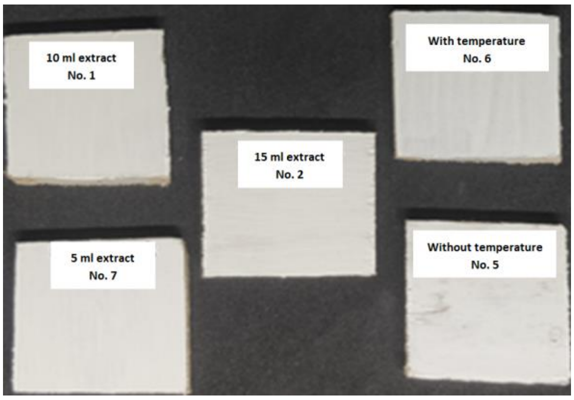

Figure 2. Multiplex sample image.

The filtering process is carried out using ordinary filter paper and Whatman paper to separate the extract from the dregs of bintaro seed powder [15]. Filtration was carried out for 2 days so that the extract was completely separated from the dregs of the bintaro seed extract powder after the extract was obtained, then centrifuged for 20 minutes [10]. The extract obtained was then mixed with commercial paint and then painted on the surface of the plywood sample (see Figure 2).

HPLC Testing

The results of the bintaro seed powder data obtained after analysis using the HPLC tool in the form of chromatograms, retention time and peak area of the compound [11]. The time data is used to determine the type of compound contained in the sample, this occurs because the price or value for each compound between the sample and the standard is the same. If the retention time of the resulting sample is the same as the time produced, then the retention of one of the standard standards contains the compound used as the standard. From 12 data taken from different concentrations and times, data was obtained. The data produced only one substance that is very dominant in the bintaro seed powder is at 3.037, area 46301227 and 283253 ppm. Then from the graph above, a control chart graph is made to see whether the data obtained is only one substance that is very prominent in the bintaro seed powder, which can be seen in Figure 3.

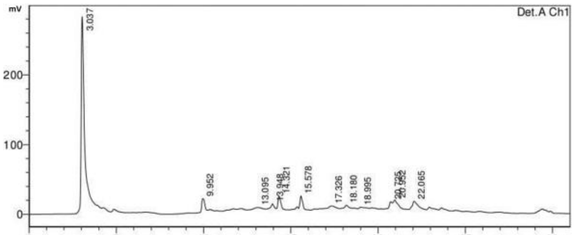

Figure 3. Spectrum p-control chart of bintaro seed powder

FTIR Test

FTIR testing aims to determine the functional groups of compounds contained in bintaro seeds and paint. The test is carried out by grinding bintaro seeds and then adjusting them to the existing spectrum, the paint used is commercial paint available in stores used for trees. The FTIR spectrum is recorded using a spectrophotometer at room temperature, the data obtained is in the form of a spectrum image between wave numbers and transmittance so that the functional groups contained in the bintaro seed powder and paint can be known. The results of the analysis of bioplastic functional groups with FTIR can be seen in Figure 4 and 5.

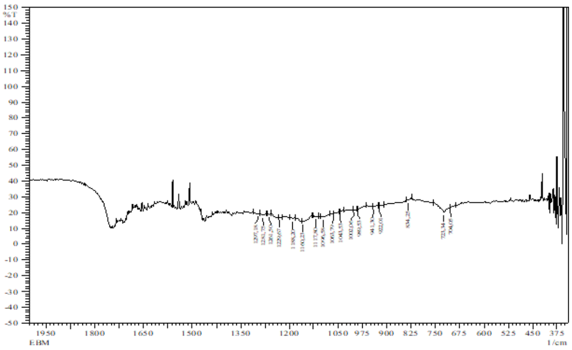

Figure 4. FTIR spectrogram of bintaro seeds.

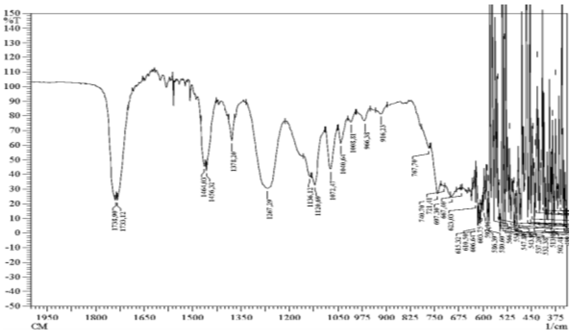

Figure 5. FTIR spectrogram of commercial paint

A wide absorption band with weak intensity at a wavelength of 1950 – 1350 cm^{-1} contains a typical alkaloid peak, where in this absorption area there is also an HN–O stretching group. Wavelength 675 – 450 cm^{-1} contains the C–Br functional group. The commercial paint graph group band has a wavelength of 4600 – 3600 cm^{-1} contains O-H (Alcohol).

Density Testing

The results of the density test for each sample are presented in Table 2. There appears to be a tendency for an increase in density when the amount of extract is increased.

Table 2. Density of liquid extract of bintaro seeds.

Sample	ρ (g/cm^3)
CEB-1	1.04
CEB-2	1.07
CEB-3	1.11

Adhesion

The results of the adhesion test (cross cut) were carried out by scratching the surface layer with a pencil, then tape was attached to the layer that had been drawn in the form of lines forming small boxes of 1 cm, then the attached tape was pulled or removed again until the results were obtained. This adhesion test (cross cut) was carried out on all test specimens as shown in Figure 6, 7, and 8.

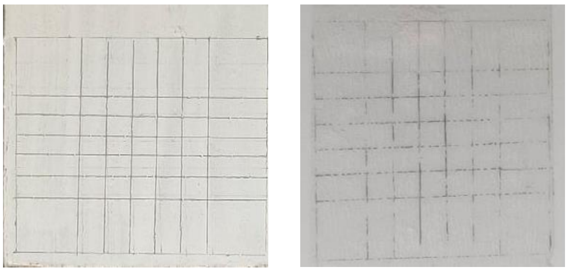
(a) (b)

Figure 6. Surface image of paint before (a) and after (b) adhesion test for sample CEB-1.

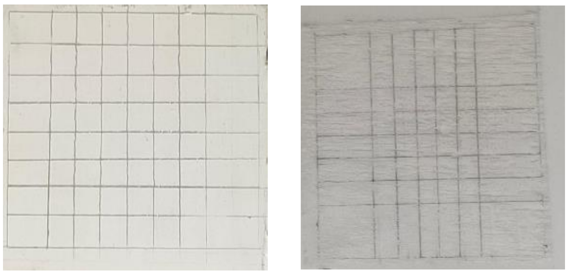
(a) (b)

Figure 7. Surface image of paint before (a) and after (b) adhesion test for sample CEB-2.

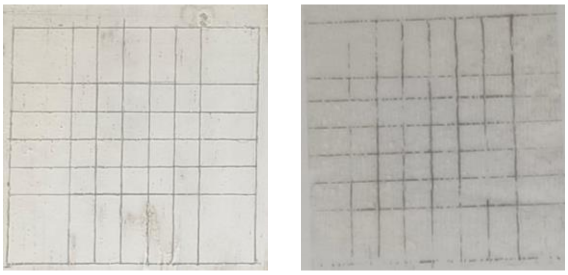
(a) (b)

Figure 8. Surface images of paint before (a) and after (b) adhesion test for CEB-3 sample.

Table 3. Adhesion test results.

Sample	Peeled in (%)	
	Image result	Visual result
CEB-1	5.62	5
CEB-2	15.18	15
CEB-3	29.42	35

The results of the adhesion test (cross cut) above show the level of adhesion of paint to the multiplex wood surface [1]. The results of visual observation and ImageJ analysis showed that shows consistent results. The large percentage of peeled ca on CEB-2 and CEB-3 samples indicates a decrease in paint adhesion due to increased concentration of bintaro seed extract. Therefore, further study is needed to determine the maximum dose of bintaro extract as a paint additive.

CONCLUSION

The content in the bintaro seed extract is proven to have alkaloid content as in the FITR test data. The density of the extract has an average value of 1.067 g/cm^2, 1.108 g/cm^2 from the data obtained means that the density of an extract reaches its maximum density value. The addition of bintaro extract concentration causes a decrease in paint adhesion.

ACKNOWLEDGMENTS

The author would like to thank the Integrated Laboratory of Universitas Muhammadiyah Riau and the Chemical Engineering, Analytical and Nanotechnology Laboratory (Material 1) of Universitas Riau for their willingness to facilitate the implementation of this research.

REFERENCES

1. Cahyadi, D. & Puspita, D. F. (2019). Pengembangan Formulasi Cat Tembok Emulsi Berbahan Acrylic untuk Meningkatkan Daya Saing IKM. *Jurnal Teknologi Bahan dan Barang Teknik*, **4**(1),

1–6.
2. Khan, M. A. & Hadromi, H. (2020). Pengaruh Inhibitor Natrium Kromat Terhadap Laju Korosi Pada Komponen Radiator Sistem Pendingin Mobil. *Automotive Science and Education Journal*, **9**(1), 18–24.
3. Wulandari, K. & Ahyanti, M. (2018). Efektivitas ekstrak biji bintaro (Cerbera manghas) sebagai larvasida hayati pada larva Aedes aegypti Instar III. *Jurnal Kesehatan*, **9**(2), 218–224.
4. Gokok, S. (2017). *Uji Toksisitas bioinsektisida ekstrak metanol buah bintaro (Cerbera odollam L.) terhadap mortalitas ulat grayak (Spodoptera litura) pada pakan daun tomat*. Universitas Sanata Dharma, Indonesia.
5. Jannah, S. R., Ika Trisharyanti, D. K., & Farm, M. (2013). Aktivitas ekstrak etanol daun bintaro (*Cerbera odollam Gaertn.*) *terhadap bakteri Shigella sonnei dan Staphylococcus saprophyticus*. Doctoral dissertation, Universitas Muhammadiyah Surakarta, Indonesia.
6. Rizal, S. & Dewi, H. (2015). Pengaruh jenis pelarut terhadap aktivitas antibakteri ekstrak daging dan biji buah bintaro (*Cerbera manghas L.*). *Jurnal Teknologi Industri & Hasil Pertanian*, **20**(1), 51–64.
7. Amelia, H. (2022). *Pengaruh ekstrak daun bintaro (Cerbera odollam) terhadap pengendalian hama ordo Lepidoptera Pada Tanaman Kubis (Brassica oleracea).* Universitas Islam Negeri Sunan Ampel, Indonesia.
8. Nandiyanto, A. B. D., Oktiani, R., & Ragadhita, R. (2019). How to read and interpret FTIR spectroscope of organic material. *Indonesian Journal of Science and Technology*, **4**(1), 97–118.
9. Suastuti, N. A., Dewi, I. P., & Ariati, N. K. Pemberian ekstrak daun sirsak (*Annona muricata*) untuk memperbaiki kerusakan sel beta pankreas melalui penurunan kadar glukosa darah. *Jurnal Kimia*, **9**(2), 289–295.
10. Lateef, A., Azeez, M. A., Asafa, T. B., Yekeen, T. A., Akinboro, A., Oladipo, I. C., Azeez, L., Ajibade, S. E., Ojo, S. A., Gueguim-Kana, E. B., & Beukes, L. S. (2016). Biogenic synthesis of silver nanoparticles using a pod extract of Cola nitida: Antibacterial and antioxidant activities and application as a paint additive. *Journal of Taibah University for Science*, **10**(4), 551–562.
11. Saputra, S. A. & Arfi, F. (2019). Analisis residu kloramfenikol pada udang windu (*Penaeus monodon*) menggunakan high performance liquid cromatography (HPLC). *Amina*, **1**(3), 126–131.
12. Widiyatun, F., Selvia, N., & Dwitiyanti, N. (2019). Analisis viskositas, massa jenis, dan kekeruhan minyak goreng curah bekas pakai. *STRING (Satuan Tulisan Riset Dan Inovasi Teknologi)*, **4**(1), 25–30.
13. ASTM Standard D3359-09. (2010). Test methods for measuring adhesion by tape test. *ASTM D3359-09*.
14. Badaring, D. R., Sari, S. P. M., Nurhabiba, S., Wulan, W., & Lembang, S. A. R. (2020). Uji ekstrak daun maja (*Aegle marmelos L.*) terhadap pertumbuhan bakteri Escherichia coli dan Staphylococcus aureus. *Indonesian Journal of Fundamental Sciences*, **6**(1), 16.
15. Putri, V. D. & Dyna, F. (2019). Standarisasi Ganyong (Canna edulis ker) sebagai pangan alternatif pasien diabetes mellitus. *Jurnal katalisator*, **4**(2), 111–118.
16. Kartimi, K. (2015). Pemanfaatan buah bintaro sebagai biopestisida dalam penanggulangan hama pada tanaman padi di kawasan pesisir Desa Bandengan Kabupaten Cirebon. *Prosiding Seminar Nasional Pendidikan Biologi 2015*, 101–111.

Indonesian Physics Communication
Department of Physics, Universitas Riau, Pekanbaru, Indonesia
p-ISSN 1412-2960 | e-ISSN 2579-521X
Vol. 21 | No. 3
November 2024
Web: https://kfi.ejournal.unri.ac.id
E-mail: kfi@ejournal.unri.ac.id

Manchester system brachytherapy simulation using EGSnrc Monte Carlo simulation

Shella Salsa Octavia, Tony Sumaryada, Sitti Yani*
Department of Physics, IPB University, Bogor 16680, Indonesia

*Corresponding author: sittiyani@apps.ipb.ac.id

ABSTRACT

One type of cervical cancer treatment is brachytherapy using the Manchester system. In this study, isodose curves were analyzed on tissue phantoms irradiated using several types of radioactive sources with the Manchester system using Monte Carlo simulation, EGSnrc. This study used a homogeneous tissue phantom with dimension 10 × 10 × 10 m^3. The Manchester system uses 2 ovoid and 3 tandem containing radioactive sources placed inside the phantom. The resulting isodose curves were combined and analyzed using MATLAB-based VDOSE GUI. The results showed that the dose distribution for each type of radioactive source at the reference point had different values, namely Cobalt-60 had a dose distribution at reference point A of 15.08% with a dose distribution at reference point B of 0%, Cesium-137 was 13.37% and 0%, Iridium-192 was 13.27% and 0%. The use of radioactive source types can be adjusted to the actual location of cervical cancer.

Keywords: Brachytherapy; EGSnrc; isodose curve; Monte Carlo; Manchester system

Received 18-10-2024 | Revised 09-11-2024 | Accepted 23-11-2024 | Published 30-11-2024

INTRODUCTION

Based on the mode of radiation delivery, radiotherapy is divided into two, namely teletherapy (the source is outside the body) and brachytherapy (the source is inside the body). Brachytherapy refers to a therapeutic technique with the placement of a radioactive source into or very close to the target tissue [1]. The most commonly used radioactive sources for brachytherapy treatment are Iridium-192 [2], Cobalt-60 [3], Cesium-137, and Radium [4]. Each radioactive source has different characteristics [3].

Brachytherapy is commonly used as a therapy for breast, prostate, cervical, and several other types of cancer [5]. Brachytherapy method by inserting a closed radioactive source in the cavity of the cancer cell site or intracavitary brachytherapy is often used in the treatment of cervical cancer [6]. Cervical cancer is an abnormal growth of cervical epithelial tissue in the neck of the uterus [7]. The Manchester system is one of the systems used in the treatment of cervical cancer through the brachytherapy method. The Manchester system is a type of brachytherapy system by implanting radioactive substances into the body through uniform dose distribution. It uses two intravaginal applicators and a rubber tandem tube. This system distributes the dose to several points [8-10]. Dose calculation in the Manchester system can be done through the Monte Carlo (MC) method [11].

Several Monte Carlo codes have been used to calculate dose distributions in several cancers with brachytherapy techniques such as MCNP [12], Geant4 [13], and EGSnrc [11]. EGSnrc is a program to simulate the transport of photon and electron particles using the MC algorithm. In this study, modelling and analysis of the effect of the type of radioactive source on the distribution of radiation dose received by the target and its surroundings through the isodose curve are carried out. This research will use the Manchester system as a method of placing radioactive sources using three radioactive sources, namely Ir-192, Cs-137, and Co-60. The results of the isodose curves of the two types of radioactivity will be compared and analyzed to determine the dose distribution. Therefore, the purpose of this study is to compare and analyze isodose curves on tissue phantoms irradiated using several different types of radioactive sources with the Manchester system through Monte Carlo simulation.

RESEARCH METHODS

Simulation Design

This study uses EGSnrc with the user code DOSXYZnrc as a simulation program. DOSXYZnrc is used to design and simulate absorbed dose with various mediums and phantom sizes [14]. A phantom is a modeling of a human object used in the field of radiology for radiodiagnostics and radiotherapy. DOSXYZnrc has several types of sources as sources used in simulations. The type of DOSXYZnrc source in this study is isource= 6: Uniform isotropically radiating parallelepiped within DOSXYZnrc. The use of this source allows the simulation of a radioactive source placed in a phantom that emits uniform radiation. The volume of the field size can be adjusted as long as it is within the DOSXYZnrc phantom (active volume is limited). The active volume of the radioactive source is bounded in the x direction by xinl, xinu (cm), bounded in the y direction by yinl, yinu (cm), and zinl, zinu, which is the z boundary of the active volume (cm).

The simulation was carried out by placing the radioactive source on a $10 \times 10 \times 10$ m^3 homogeneous phantom which all voxel parts contained tissue material with the information of each voxel shown in Table 1. The radioactive sources used were Iridium-192, Cesium-137, and Cobalt-60. The Manchester system applicator was inserted into the phantom with one intrauterine rubber tandem tube containing 3 radioactive seeds inside and two ovoids (intravaginal applicators) each containing a radioactive seed. In direct clinical use, points A and B are located on the right and left sides. Point A is located 2 cm to the right, left of the tandem and 2 cm above the ovoids. Point B is located 5 cm and 2 cm to the right, left of the tandem and above the ovoids. This point is 3 cm lateral to point A. Point B is used to deliver the dose to the distal parametrium [3].

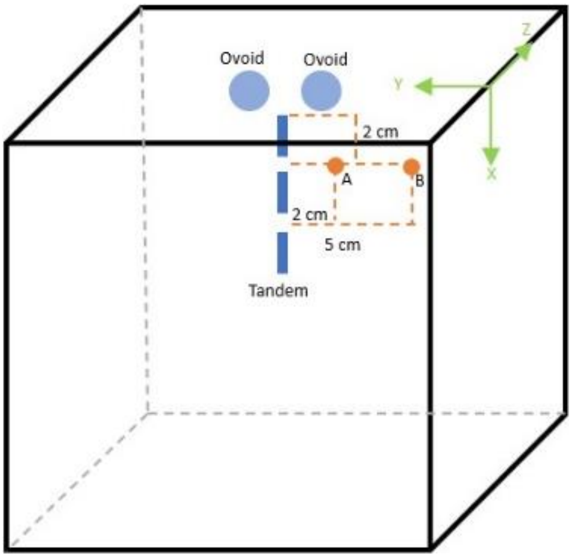

Figure 1. Set-up of the phantom simulation.

Table 1. Virtual phantom information.

Axis	Voxel number	Voxel size (cm)	Voxel Boundaries (cm)
x	100	0.1	-5 to + 5
y	100	0.1	-5 to +5
z	100	0.1	0 to 10

Dose Distribution Analysis

Each simulation produces output files that are used in the data analysis process, namely .3ddose files and .egsphant files. The dose profile is a dose distribution curve in a certain direction in one dimension obtained by analyzing the .3ddose file through the STATDOSE program. Isodose curves can be obtained using dosxyz_show or VDOSE. The .3ddose and .egsphant files of each radioactive source applicator location (2 on ovoid and 3 on tandem) will be merged using the MATLAB-based VDOSE GUI. The merged results will produce isodose curves. The isodose curve will be analyzed at point A and point B of the Manchester system. The results of the dose distribution analysis are compared between the three types of radioactive sources used in this study.

RESULTS AND DISCUSSION

Dose Profile

The three-dimensional dose distribution data generated by the simulation process by DOSXYZnrc is stored in a .3ddose file. The data file can be analyzed using STATDOSE to produce dose profiles for each radioactive type. The dose profile is a picture of the dose distribution curve in two dimensions. Figure 2 below displays a graph of the dose profile received along the phantom Y-axis versus depth using Cobalt-60 radioactivity (Figure 2). The relative dose was obtained from normalizing the .3ddose data to the maximum dose after analysis by the STATDOSE program. The radioactive isodose profile curve images between Cobalt-60, Cesium-137 and Iridium-192 are similar.

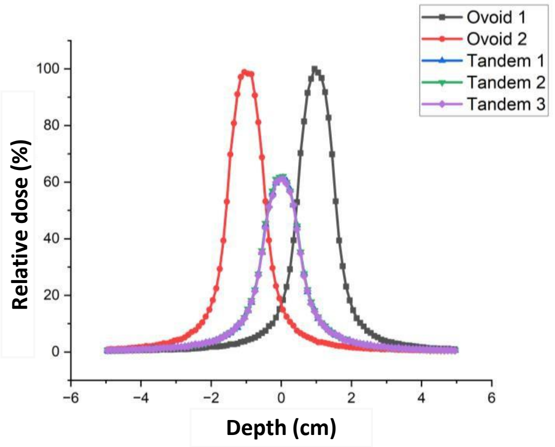

Figure 2. Dose profile using Cobalt-60 radioactive in 2 cm depth.

Cobalt-60 has the highest relative dose where ovoid 1 is 100% at a depth of 0.95 cm, ovoid 2 is 98.30% at a depth of -0.95 cm, tandem 1 is 61.56% at a depth of 0.04 cm, tandem 2 is 61.06% at a depth of 0.04 cm, and tandem 3 has a relative dose of 61.08% at a depth of 0.04 cm. Radioactive Cesium-137 and Iridium-192 had the same relative dose in each applicator. The relative dose in ovoid 1 for both radioactive is 100% at a depth of 1.05 cm, ovoid 2 is 98.97% at a depth of -0.95 cm, tandem 1 is 61.44% at a depth of -0.05, tandem 2 is 60.24% at a depth of 0.04 cm, and tandem 3 is 59.18% at a depth of -0.05. The similarity between iridium-192 and Cesium-137 and the difference between the two against Cobalt-60 may occur due to differences in average energy. Iridium-192 and Cesium-137 have an average energy of 0.4 MeV and 0.66 MeV, respectively, so they have an energy difference of 0.26 MeV. However, Cobalt-60 has an average energy of 1.17 MeV so it has a larger difference of about 0.51 – 0.77 MeV which affects the dose difference.

Isodose Curve

The isodose curve shows the dose distribution over a given area at a given depth. This study uses a radioactive source applicator that will be separated into 5 sections. The sections are ovoid 1 which is the section located at the bottom left position (Figure 3a), ovoid 2 which is the section located at the bottom left position (Figure 3b), tandem 1 which is the source located at the center of the Y voxel direction and the left in the X voxel direction, tandem 2 which is the source located after tandem 1, and tandem 3 which is located after tandem 1 and 2. The colors on the curve represent the amount of dose distribution received. The red color represents the location with the highest level of dose distribution and the blue color represents the location with the lowest dose distribution. The location of the source placement is the same for each radioactive type. All three types have similar isodose curves. Figure 3 below illustrates the radioactive isodose curve for each section of the applicator.

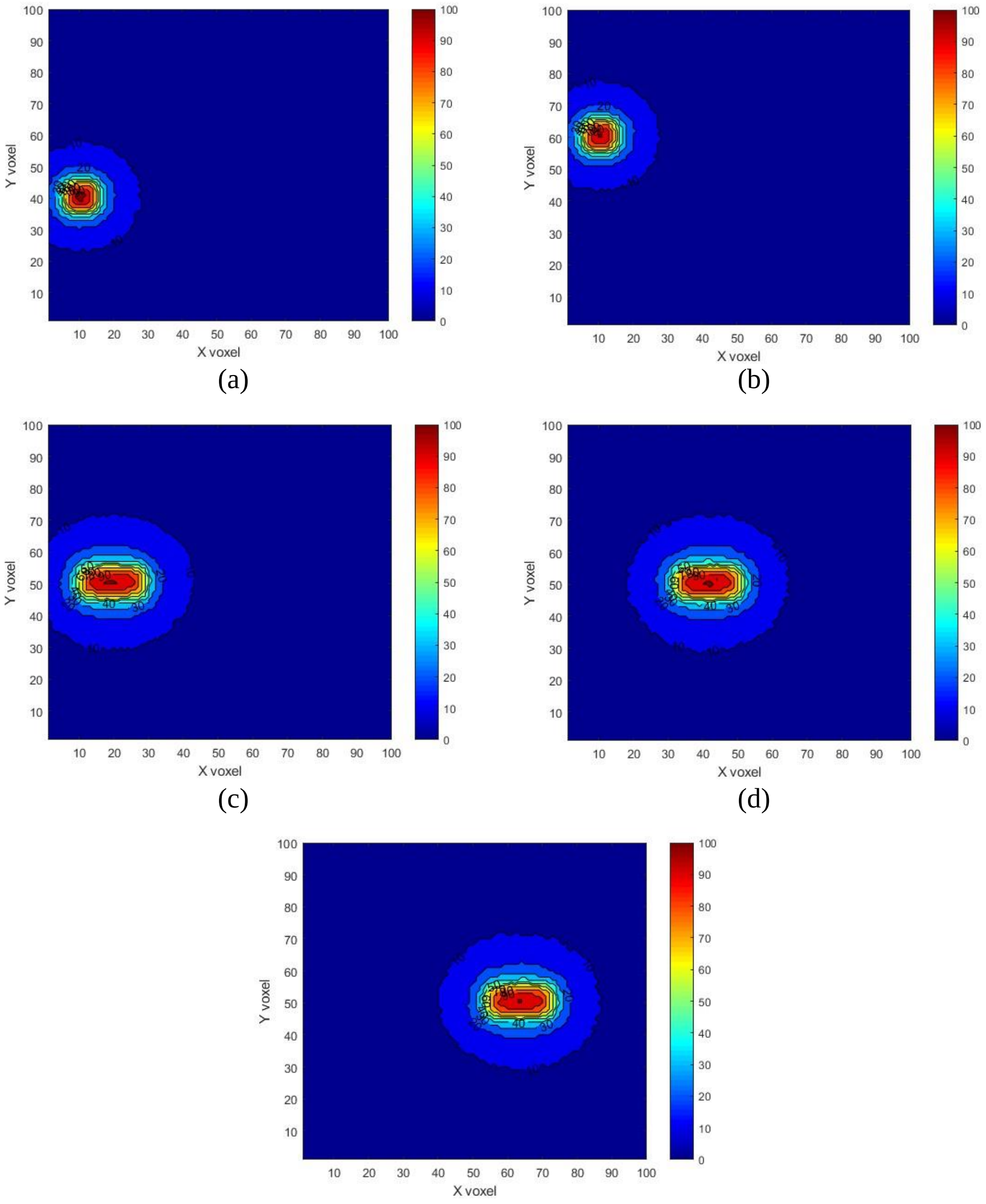

(a) (b) (c) (d) (e)

Figure 3. Cobalt-60 isodose curve of section: (a) Ovoid 1; (b) Ovoid 2; (c) Tandem 1; (d) Tandem 2; and (e) Tandem 3.

Comparison of Isodose Curves at a depth of 4.5 cm

The isodose curve in each voxel layer will be different due to differences in the placement of the radiation source location, density, and energy used. The difference in dose distribution can be seen in the parameter with a color gradation from intense blue to intense red located next to the isodose curve image. In this study, the isodose curve is obtained by cutting the voxel in the Z direction, so the layers to be discussed are layers in the z-axis or depth direction.

Analysis of the isodose curves at a depth of 4.5 cm shows variations in dose distribution for each type of radioactivity used. Cobalt-60 shows the highest dose distribution of 60%, with the dark red area in Figure 4, while Cesium-137 and Iridium-192 have the highest dose distribution of 50%. The colors in the isodose curve indicate the level of dose distribution, with red indicating the highest dose and blue indicating the lowest dose. The dose distribution is also outlined in Y and X voxels for each radioactive type, with the highest dose area located at the ovoid position. Colors such as orange, yellow, green, navy blue, and dark blue indicate decreasing levels of dose distribution, with distribution values ranging from 50% to 0%.

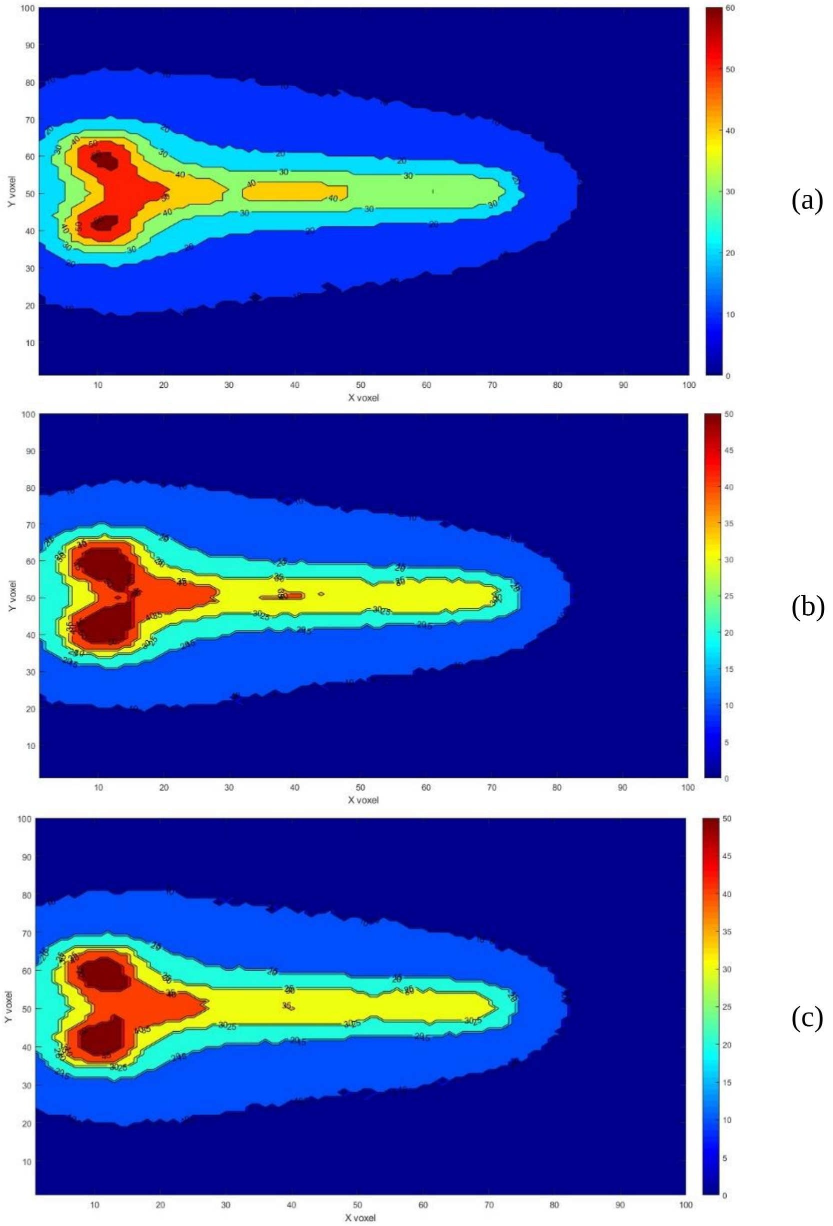

Figure 4. Isodose curves at the 4.5 cm depth for radioactive: (a) Cobalt-60; (b) Cesium-137; and (c) Iridium-192.

Dose Comparison on Manchester System

Cobalt-60 vs Iridium-192

A comparison of the dose distribution (dose difference at the same voxel) between Cobalt-60 and Iridium-192 is shown in Figure 5. The difference is due to the large energy difference between the two radioactive types, which is 0.77 MeV. The difference in dose distribution is seen in the parameter with a color gradation from intense blue to bright yellow. The parameter shows that the level of difference in dose distribution is 0% to 8.5%. The area that has the largest dose distribution difference is in the area around the two ovoids and tandem 1 (Tandem closest to the ovoid), with a yellow color indicating that there is a dose distribution difference of about 8.5% in that area. Each part of the applicator has a dose distribution difference of 0% – 4%. The locations around tandem 2 and tandem 3 have a dose difference between 5% – 6% and around ovoid 1, ovoid 2, and tandem 1 have a dose distribution difference of 6% to 8.5%.

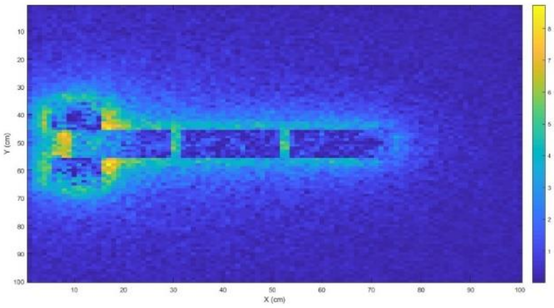

Figure 5. Comparison of Cobalt-60 and Iridium-192 isodose curve.

Cobalt-60 vs Cesium-137

Cobalt-60 and Cesium-137 have large difference in dose distribution due to the difference in average energy between the two radioactive types about 0.51 MeV (Figure 6). The difference in dose distribution can be seen in the parameter with a color gradation from intense blue to bright yellow. The parameter shows that the level of difference in dose distribution is 0% to 7.5%. The area that has the largest dose distribution difference is around the two ovoids and tandem 1 with a yellow dose distribution indicating that there is a dose distribution difference of about 7.5%.

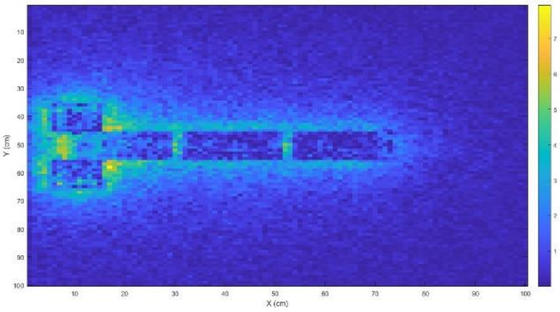

Figure 6. Comparison of Cobalt-60 and Cesium-137 isodose curve.

Iridium-192 vs Cesium-137

The dose distribution comparison between Iridium-192 and Cesium-137 is not as big as the difference with Cobalt-60 (Figure 7). The existence of a comparison that is not too large is caused by the average energy difference between iridium-192 and cesium-137 of only 0.37 MeV. The highest dose difference is 3.5% around both ovoid and tandem 1.

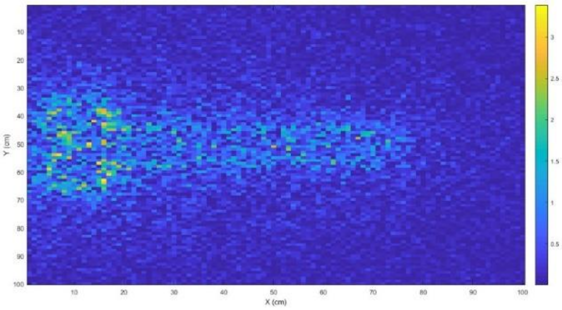

Figure 7. Comparison of Cesium-137 and Iridium-192 isodose curve.

Dose Distribution in Manchester System

Each type of radioactivity using the Manchester system has a different dose distribution which causes the dose at reference points A and B to be different. According to Banahene et al. (2019) point A in the Manchester system is located at 2 cm above the tip of the tandem and also 2 cm lateral from the cervical canal while point B is at a position 3 cm lateral from point A or 5 cm from the centerline of the tandem (Figure 1) [15]. The reference point refers to the rectum and bladder as radiosensitive organs adjacent to the target volume in cervical cancer. In Cobalt-60, the dose distribution exposure received by voxels at reference points A and B was 15.08% and 0%, respectively. Cesium-137 was 13.37% at point A and 0% at point B. Iridium-192 had a dose distribution value at reference point A of 13.27% and reference point B was 0%.

According to Toossi et al. (2012), based on the ICRU (The International Commission of Radiation Units and Measurement) report number 38 recommend the definition of reference points in the implementation procedure. The reference point A dose should be limited to 80% of the defined point A dose [16]. Therefore, the three types of radioactivity used in this study have appropriate reference point values and are not greater than 80%. The use of the type of radioactive source can be adjusted according to the actual location point of cervical cancer.

CONCLUSION

This study used a tissue phantom of 10 × 10 × 10 m^3 with the same radioactive source point location for the three types of radioactivity, Cobalt-60, Cesium-137, and Iridium-192. The isodose curve in brachytherapy using the Manchester system from each radioactive gives different results. The three types of radioactivity have reference point values that are in accordance with the recommendations of the ICRU (The International Commission of Radiation Units and Measurement) report number 38, that the reference point A dose should be limited to 80% of the specified point A dose. Cobalt-60 received a dose distribution exposure at reference point A of 15.08% which is the highest relative dose value compared to the radioactive sources, Cesium-137 and Iridium-192.

REFERENCES

1. Stish, B. J., Davis, B. J., Mynderse, L. A., McLaren, R. H., Deufel, C. L., & Choo, R. (2018). Low dose rate prostate brachytherapy. *Transl Androl Urol*, **7**(3), 341–356.
2. Görkem, A. K. S. U. (2017). Serviks ve endometrium kanserinde brakiterapi. *Turkish Journal of Oncology*, **32**(1), 34–35.
3. Wen, A., Wang, X., Wang, B., Yan, C., Luo, J., Wang, P. & Li, J. (2022). Comparative analysis of 60Co and 192Ir sources in high dose rate brachytherapy for cervical cancer. *Cancers*, **14**, 749.
4. Hellman, K., Hellström, A. C., & Pettersson, B. F. (2014). Uterine cervix cancer treatment at Radiumhemmet: 90 years’ experience. Time trends of age, stage, and histopathology distribution. *Cancer Med.*, **3**(2), 284–292.
5. Strohmaier, S. & Zwierzchowski, G. (2011). Comparison of Co-60 and Ir-192 sources ih HDR brachytherapy. *Journal of Contemporary Brachytherapy*, **3**(4), 199–208.
6. Carvalho, H.A. & Mauro, G.P. (1992). History of radiotherapy in the treatment of uterine cervix cancer: an overview. *Rev Assoc Med Bras.*, **69**(suppl 1), e2023S126.
7. Zhang, S., Xu, H., Zhang, L., & Qiao, Y. (2020). Cervical cancer: Epidemiology, risk factors and screening. *Chin J Cancer Res.*, **32**(6), 720–728.
8. Tod, M. & Meredith, W.J. (1953). Treatment of cancer of the cervix uteri, a revised Manchester method. *Br J Radiol.* **26**, 252–257.
9. Hoskin, P. J. & Rembowska, A. (1998). Dosimetry rules for brachytherapy using high dose rate remote afterloading implants. *Clinical Oncology*. **10**(4), 226–230.
10. Eng, T. Y., Cummins, S., & Baake, D. (2007). Point A or point H in prescribing high-dose-rate (HDR) intracavitary brachytherapy for cervical carcinoma? *International Journal of Radiation Oncology, Biology, Physics*. **69**(3), S396–S397.
11. Kurniati, F., Krisna, F. P., Junios, & Haryanto F. (2021). The dose distribution from Iridium-192 source on cervical cancer brachytherapy by Manchester system using Monte Carlo simulation. *Atom Indonesia*. **47**(3), 205–211
12. Morato, S., Juste, B., Peris, S., Miro, R., Verdu, G., Ballester, F., & Vijande, J. (2018). Brachytherapy organ dose estimation using Monte Carlo simulations of realistic patient models. *Annu Int Conf IEEE Eng Med Biol Soc*, **2018**, 6149–6152.
13. Liu, J., Medhat, M. E., & Elsayed, A. M. M. (2024). Geant 4 Monte Carlo

simulation for I-125 brachytherapy. *Nuclear Engineering and Technology*, **56**(7), 2516–2523.

14. Walters, B., Kawrakow, I., & Rogers, D.W.O. (2021). *DOSXYZnrc User Manual*. Ottawa: National Research Council Canada.
15. Banahene, J. O., Darko, E. O., Abubakar, M., Awuah, B., & Amoako. (2019). Using Manchester system for the treatment of cervix carcinoma for a selected oncology facility in Ghana. *International Journal of Science and Research (IJSR)*, **8**(1), 1395–1401.
16. Toossi, M. T. B., Ghorbani, M., Makhdoumi, Y., Taheri, M., & Shandiz, F.H. (2012). A retrospective analysis of rectal and bladder dose for gynecological brachytherapy treatments with GZP6 HDR afterloading system. *Reports of Practical Oncology & Radiotherapy*, **17**(6), 352–357.